Thermodynamic characterization of azepane based compounds

Experimental insights and structure-property relationship

Maria Luís de Almeida Ferreira do Vale Nogueira
Master in Chemistry
Department of Chemistry and Biochemistry
Faculty of Sciences of the University of Porto
2024/2025

Thermodynamic characterization of azepane based compounds

Experimental insights and structure-property relationship

Maria Luís de Almeida Ferreira do Vale Nogueira

Master in Chemistry - Specialization in Functional Materials and Surfaces for Sustainability

Department of Chemistry and Biochemistry

2024/2025

Supervisor

Vera Lúcia de Sousa Freitas, PhD specialized in the scientific field, CIQUP, Faculty of Sciences of University of Porto

Co-Supervisor

Maria das Dores Ribeiro da Silva, Associate Invited Professor, Faculty of Sciences of University of Porto

Abstract

Hydrogen storage remains a central challenge for sustainable energy, motivating the search for molecular carriers that combine efficient hydrogen uptake with facile release.

This dissertation presents a combined thermophysical and thermochemical study of the azepan derivatives: iminostilbene (IMB), iminodibenzyl (IDB) and 5-acetyliminodibenzyl (AcIDB). Thermophysical properties were established via DSC/TG–DSC (phase transitions) and sublimation enthalpies determined by Knudsen effusion mass loss (KEML), Knudsen effusion mass spectrometry (KEMS) and non-isothermal thermogravimetry (NITG); KEMS also verified a predominantly monomeric vapour under the measurement conditions. Thermochemical analysis was anchored by G3(MP2)//B3LYP calculations, providing gas-phase standard enthalpies of reaction and position-resolved hydrogenation enthalpies. The integrated experimental–computational framework assesses the suitability of these scaffolds as organic hydrogen carriers (OHCs) by jointly considering hydrogenation energetics alongside liquid-phase operability (melting behaviour, supercooling and volatility).

Part of the experimental programme was carried out during a two-month Erasmus+ research stay at Sapienza University of Rome, supervised by Prof. Stefano Vecchio Ciprioti (Department of Basic and Applied Sciences for Engineering) and Prof. Andrea Ciccioli (Department of Chemistry), enabling cross-laboratory validation of methods and results.

Keywords: Iminodibenzyl, Iminostilbene, 5-Acetyliminodibenzyl, hydrogen storage and transport, thermodynamic properties

Resumo

O armazenamento de hidrogénio continua a ser um desafio central no ramo da energia sustentável, o que motiva o estudo e o desenvolvimento de novos transportadores de hidrogénio que assegurem uma absorção e libertação de hidrogénio eficiente.

Esta dissertação apresenta a combinação do estudo termodinâmico de derivados do azepano: iminostilbeno (IMB), iminodibenzil (IDB) e 5-acetiliminodibenzil (AcIDB). As propriedades termofísicas foram determinadas por DSC/TG–DSC (transições de fase) e as entalpias de sublimação foram determinadas por efusão de Knudsen por perda de massa (KEML), espectrometria de massa por efusão de Knudsen (KEMS) e termogravimetria não isotérmica (NITG); e foi possível observar, pelo método KEMS, um vapor predominantemente monomérico às condições experimentais. A análise termoquímica foi complementada com cálculos G3(MP2)//B3LYP, que forneceram as entalpias padrão de reação em fase gasosa e entalpias de hidrogenação resolvidas por posição. A estrutura experimental-computacional integrada permite a avaliação dessas estruturas como transportadores orgânicos de hidrogénio (OHCs), considerando simultaneamnte a energia de hidrogenação e o estabilidade na fase líquida (comportamento de fusão, super-arrefecimento e volatilidade).

Parte do programa experimental foi realizado na Universidade Sapienza de Roma, ao abrigo do programa Erasmus+, com a duração de dois meses e foi supervisionada pelo Prof. Stefano Vecchio Ciprioti (Departamento de Ciências Básicas e Aplicadas para a Engenharia) e pelo Prof. Andrea Ciccioli (Departamento de Química), permitindo a validação interlaboratorial de métodos e resultados.

Palavras-chave: Iminodibenzil, Iminostilbeno, 5-Acetiliminodibenzil, armazenamento e transporte de hidrogénio, propriedades termodinâmicas

Acknowledgements

Esta dissertação e o trabalho apresentado, só foi possível com o apoio e contribuições das pessoas e instituições às quais quero expressar o meu apreço.

À que embarcou comigo nesta aventura, a Doutora Vera Freitas. Agradeço por ter estado sempre do meu lado (seja na cidade *Invicta* seja na cidade *Eterna*), mesmo com todos os desafios que foram surgindo ao longo do ano. Nunca desistiu de mim e motivou-me a ser mais e melhor. Consigo aprendi muito sobre química e mais! Sou grata por todos os conselhos, pela orientação e pela preocupação que sempre teve comigo. Um grande exemplo como cientista e também como pessoa. Foi um prazer trabalhar consigo!

À Professora Maria das Dores M. C. Ribeiro da Silva, por me ter dado a oportunidade e também a confiança para integrar neste grupo de trabalho. Uma referência marcante desde que fui sua aluna na licenciatura. Motivou-me muito e mostrou-me o significado de resiliência. Agradeço pela orientação e por todos os conhecimentos transmitidos.

To Professor Stefano Vecchio Ciprioti for welcoming me so kindly in you're your laboratory and for accepting this challenge! I cherish the time that I've spent in Rome and I'm grateful that I had the opportunity to learn from someone with so much knowledge. I would also like to thank Professor Andrea Ciccioli, Doctor Bruno Brunneti and Doctor Lorenza Romagnoli for receiving me in their laboratories at La Sapienza University of Rome and helping me to work on this dissertation. Também ao Ferraz por ter sido um grande apoio ao longo dos meus anos de estudante e também parceiro de laboratório em Roma.

Ao Departamento de Química e Bioquímica da Faculdade de Ciências pela Universidade do Porto, ao Centro de Investigação em Química da Universidade do Porto, e à Universidade "La Sapienza" de Roma pelo apoio e pelas condições disponibilizadas para a execução deste trabalho.

Ao programa Erasmus+ pela concessão da bolsa de mobilidade de longa duração que tornou a minha estadia em Roma possível.

A todos os passaram por mim ao longo destes longos 5 anos (e não só), um mega obrigado. Foram anos muito felizes e atribulados mas sempre bem acompanhada. Aos "dissimulados" que sobreviveram comigo, obrigada por me terem carregado. A todas as amizades que fiz na AEFCUP, fizeram parte de um lindo capítulo. Aos que

rapidamente tornaram-se amigos da vida, com menção especial aos desumildes, aos campeões, aos mais novos e velhos que se tornaram muito especiais. Não esquecer dos “Quem?”. Terei sempre um grande carinho por todos.

Um obrigada ginórmico às que me acompanharam sempre, Sofia, Guida, Meireles, Raquel e Teresa. Nem sempre fui fácil e estiveram sempre lá por mim mesmo a ouvir as teorias mais loucas de sempre e também acompanharam sidequests igualmente loucos.

Por fim, aos meus pais, à minha irmã (e à Pepa): Nem sempre fui fácil de aturar, mas é de família! Agradeço por terem estado sempre lá e por me terem proporcionado tudo o que estava ao vosso alcance e não só.

Obrigada.

Table of contents

List of figures

List of tables

List of abbreviations

AclDB	5-Acetyliminodibenzyl
CHCs	Chemical hydrogen carriers
COHCs	Cyclic organic hydrogen carriers
DFT	Density functional theory
DSC	Differential scanning calorimetry
DOE	Design of experiments
HAE	Heavy atom effect
HTMs	Hole transport materials
IDB	Iminodibenzyl
IMB	Iminostilbene
I-TG	Isothermal thermogravimetric analysis
KEML	Knudsen effusion mass-loss
KEMS	Knudsen effusion mass spectrometry
LOHCs	Liquid organic hydrogen carriers
NI-TG	Non-isothermal thermogravimetric analysis
OFETs	Organic field-effect transisitors
OHCs	Organic hydrogen carriers
OLEDs	Organic light-emitting diodes
OPVs	Organic photovoltaics
OSCs	Organic semiconducting materials
QCM	Quartz crystal microgravimetry
QCMB	Quartz crystal microbalance
RISC	Reverse intersystem crossing
SOHCs	Solid organic hydrogen carriers
TADF	Thermally activated delayed fluorescence
TGA	Thermogravimetric analysis

List of symbols

$\Delta_{\mathrm{cr}}^{\mathrm{l}}\boldsymbol{H}_{\mathrm{m}}$	Molar enthalpy of fusion
$\Delta_{\mathrm{cr}}^{\boldsymbol{g}}\boldsymbol{H}_{\mathrm{m}}$	Molar enthalpy of sublimation
$\Delta_{\mathrm{l}}^{\boldsymbol{g}}\boldsymbol{H}_{\mathrm{m}}$	Molar enthalpy of vaporization
$\Delta\boldsymbol{H}_{\boldsymbol{d}}$	Dehydrogenation enthalpy
C	Heat capacity
Cr	Crystalline
E	Energy
G	Gibbs free energy
H	Enthalpy
m	Mass
p	Pressure
$\boldsymbol{p^o}$	Vapor pressure
q	Heat
S	Entropy
T	Temperature
t	Time
U	Internal energy
w	Work
Δ	Change
$\boldsymbol{\mu}$	Chemical potential
$\boldsymbol{\sigma}$	Effective molecular collision diameter
$\boldsymbol{\phi}$	Heat flow

1. Introduction

Global energy demand is still met predominantly by fossil fuels, the main source of greenhouse-gas emissions with significant environmental and health impacts. To reduce these emissions and progress toward carbon neutrality by 2050 [1] the scientific community is accelerating research into alternative energy systems and the supporting infrastructure required to deploy them at scale. A critical enabler of this transition is energy storage, which buffers the intermittency of renewables and stabilizes power supply. Current storage options include electrochemical (batteries) [2], chemical (hydrogen systems) [3], gravitational/potential (pumped hydropower) [4], kinetic (flywheels) [5], magnetic (superconductors) [6], and thermal/thermochemical (e.g., molten salts) [7]. In practice, heterogeneity in renewable resources, population density, industrial demand, and load profiles complicates techno-economic choices and regional deployment strategies.

Among chemical options, hydrogen has gained substantial attention as a clean energy carrier that emits only water at the point of use. Its total environmental footprint, however, depends on the production route: fossil-based pathways still generate CO_2 unless paired with effective carbon capture. Conventional storage and distribution - compressed gas, cryogenic liquid, and condensed-phase storage - face challenges of safety, low volumetric density, boil-off, transport, cost, and the need for new infrastructure [8]. Overcoming these barriers is essential to unlock the potential of hydrogen across power generation, transportation, steelmaking, and petrochemicals. While non-recyclable inputs remain in parts of the value chain, a key bottleneck persists in storage and transport. In this context, organic hydrogen carriers (OHCs) and related condensed-phase approaches have attracted interest for operation at comparatively mild temperatures and pressures with conventional liquid-handling logistics.

Early demonstrations have already appeared at pilot scale - for example, the first marine transport of an organic carrier was reported in 2022 on [9]. Looking forward, hydrogen is expected to serve both as feedstock and heat source across multiple industries, provided storage solutions meet efficiency, safety, and cost targets.

Various materials have been explored for this purpose, including (OHCs), which provide a promising alternative for conventional hydrogen storage by enabling safe and efficient hydrogen uptake, transport, and release.

(OHCs) enable safe, high-density, and potentially reversible chemical storage of hydrogen by hydrogenation/dehydrogenation cycles, facilitating uptake, transport, and release. Their practicality, however, depends on thermophysical and thermodynamic properties: thermal stability, hydrogen binding enthalpy, and the reversibility and kinetics of the coupled reactions. Within the wide chemical design space, tricyclic heteroaromatic frameworks have emerged as promising because of their structural tunability, high thermal stability, favourable redox behaviour, and rich π-conjugation. Nitrogen-containing heterocycles in particular have been explored in organic electronics [10], catalysis [11], and energy storage systems [12], and they exhibit properties relevant to hydrogen handling and charge transport [13].

Beyond their role as hydrogen carriers, *N*-heterocycle–based compounds exhibit remarkable optical and electronic properties, making them highly versatile for both energy storage and optoelectronic applications. Their π-conjugated frameworks promote electron delocalization and tunable electronic structures, which are critical for hydrogen-storage mechanisms (binding/release), charge transport, and radiative emission [14, 15]. Owing to these attributes, carbazole and azepine derivatives have been extensively explored in organic light-emitting diodes (OLEDs), thermally activated delayed fluorescence (TADF) emitters, and organic photovoltaics (OPVs) [16].

Driven by their structures and electronic properties, cyclic organic compounds have attracted growing attention. Several molecular-engineering strategies are commonly employed to tailor performance, including ring fusion, introduction of electron-donating substituents, and heteroatom incorporation (N, O, S) into the aromatic core [17].

In the context of hydrogen storage, *N*-functionalized compounds, such as phenylcarbazoles and their halogenated derivatives, as well as azepine derivatives, have shown potential for reversible hydrogenation/dehydrogenation [18]. Their ability to store and release hydrogen efficiently under controlled conditions makes them attractive next-generation OHCs, where molecular stability, reversibility, and high hydrogen capacity are essential [19]. Halogenation [20], particularly bromination, in carbazole-based molecules can modulate electronic properties [21], lower melting points, and influence phase transitions, thereby enhancing their performance as hydrogen-storage materials.

For hydrogen carriers, a lower melting point improves processability (easier liquefaction and pumping), can facilitate thermal management, and enables more efficient hydrogenation/dehydrogenation cycles - benefits that are especially valuable in liquid OHCs, where phase behaviour and temperature-dependent kinetics strongly affect performance [13]. Lower melting points also aid handling, transportation, and, in some

systems, reversibility of hydrogen-release/uptake [22], making brominated derivatives promising candidates for future hydrogen-storage technologies.

This dual functionality - as efficient hydrogen carriers and as optoelectronic materials - positions *N*-functionalized compounds as innovative building blocks for next-generation energy technologies. Their high thermal/chemical stability and ability to undergo reversible redox processes make them promising for sustainable hydrogen storage, energy-efficient lighting, and advanced photovoltaics.

A comprehensive understanding of the thermodynamic properties of these promising OHCs is essential for their further development. Key parameters – as enthalpy and entropy of hydrogenation/dehydrogenation, hydrogen binding energy, and phase-transition temperatures/enthalpies - govern efficiency, reversibility, and practical feasibility. Thermodynamic characterization is particularly important to define operating windows, anticipate kinetic/energetic barriers affecting hydrogen release and uptake, and quantify how halogenation impacts molecular stability and hydrogen-bonding strengths. By tailoring the thermodynamic landscape of *N*-heterocycle–based compounds, researchers can design hydrogen carriers with optimized operating conditions, improved reversibility, and long-term stability, contributing to the advancement of hydrogen storage and sustainable energy technologies.

1.1 Hydrogen Storage Systems

Hydrogen is the most abundant element in the universe and, on Earth, occurs mainly in compounds such as water and hydrocarbons. It is considered a clean fuel at the point of use, since its combustion produces primarily water with negligible pollutant emissions. Hydrogen has a high gravimetric energy density 120 MJ/kg [23] and can be produced by several methods, including renewable electrolysis [24].

The versatility of hydrogen makes it an attractive energy vector. In transportation, fuel cells convert chemical energy to electricity via electrochemical reactions, offering up to ~30% higher tank-to-wheel efficiency than conventional engines [25]. In industry, hydrogen can provide low-carbon high-temperature heat [26]. In buildings, combined with cooling, heating and power systems (CCHP) based on fuel cells offer stable, cleaner alternatives to boilers. In the power sector, hydrogen can complement wind and solar - today’s dominant renewables - by mitigating intermittency and stabilizing supply [27].

Hydrogen can be stored as compressed gas, cryogenic liquid, solid-state, or chemically bound in carriers. The storage choice strongly impacts energy density, safety, costs, and logistics.

1.1.1 Compressed Gaseous Hydrogen Storage

Compressed gaseous hydrogen storage relies on high-pressure vessels, which are categorized based on their pressure capacity: Type I (<20 MPa), Type II (20-30 MPa), Type III (30-45 MPa), and Type IV (>45 MPa) [28]. This method offers rapid refuelling rates and good compatibility with the existing hydrogen infrastructure, making it one of the most widely adopted storage solutions, however it requires high pressures, around 35-70 MPa [29], to store appreciable amounts of hydrogen, while still exhibiting relatively low volumetric energy densities around 40 kg/m^3 at 70 MPa [30]. In addition, safety concerns arise due to the hazards associated with high-pressure containment.

To overcome these challenges, larger and more robust storage vessels are often required, which increases both capital and operational costs. Furthermore, compression to such high pressures consumes a considerable amount of electricity, adding significantly to the overall energy demand.

Mitigating these limitations requires technological advancements. The development of lightweight, high-performance composite materials can reduce vessel mass and manufacturing costs, while improving mechanical strength. Enhancing compressor efficiency can lower the energy burden of gas pressurization, and the integration of advanced monitoring and safety systems can improve reliability and operational security. Taken together, these improvements could make compressed gaseous hydrogen storage a more viable and cost-effective option for large-scale energy applications.

1.1.2 Cryogenic Liquid Hydrogen Storage

Cryogenic liquefaction enables hydrogen to be stored in its liquid state, requiring extremely low temperatures and advanced insulation materials to maintain stability. Compared with compressed gaseous hydrogen storage, liquid hydrogen storage provides significantly higher energy densities. For instance, Song et al. [31] reported a density of 64 kg/m^3 at 10 MPa and −235.15ºC. Moreover, the high latent heat of vaporization of liquid hydrogen offers advantages for thermal management and safety, as it helps mitigate the risk of rapid pressure build-up in the event of leaks [28].

Despite these advantages, cryogenic storage faces major challenges. The liquefaction process is highly energy-intensive, consuming approximately 30–40% of the stored hydrogen’s energy content [32]. The design of cryogenic tanks is also technically

complex and costly, while continuous evaporation losses (~3% per day) further compromise storage efficiency [28].

To address these drawbacks, research is directed toward several areas: reducing energy consumption during liquefaction by adopting advanced cooling technologies; improving insulation performance with novel high-efficiency materials to minimize boil-off losses; and developing safer, more cost-effective tank designs. Optimizing operational conditions also plays a key role in enhancing reliability, lowering infrastructure costs, and improving hydrogen handling efficiency.

Although liquid hydrogen storage achieves higher densities than compressed storage and can offer greater safety under controlled conditions, its economic and energetic limitations remain significant. Future developments must therefore focus on reducing infrastructure costs, improving liquefaction efficiency, and enhancing long-term stability if cryogenic hydrogen storage is to become a practical large-scale solution for hydrogen energy systems.

1.1.3 Hydrogen Carriers

Hydrogen carriers enable the safe, efficient, and often reversible storage of hydrogen, playing a crucial role in large-scale energy storage and transport. Unlike compressed or cryogenic storage, these systems rely on chemical binding, where hydrogen is stored within molecular structures and subsequently released under controlled conditions.

Hydrogen carriers can be broadly categorized into two classes:

- Solid-state hydrogen storage
- Organic Hydrogen Carriers (OHCs), which may be solid (SOHCs) or liquid (LOHCs)

Solid-state Hydrogen Storage

Hydrogen storage in solid-state systems can occur through physisorption or chemisorption, two mechanisms that differ fundamentally in reversibility and energy requirements.

- Physisorption relies on weak van der Waals interactions, making it fully reversible and strongly dependent on surface area, porosity, and temperature/pressure conditions. Materials such as carbon-based structures, MOFs, and zeolites exemplify this class, where storage efficiency increases with higher surface affinity [33-35].

- Chemisorption, by contrast, involves the formation of chemical bonds between hydrogen and the solid matrix. This process typically exhibits stronger interactions, higher heats of adsorption, and lower reversibility, often requiring chemical or thermal activation to release hydrogen. Metal hydrides are classical examples of this category and are often classified as Chemical Hydrogen Carriers (CHCs) [36].

CHCs such as ammonia, formic acid, and borohydride offer high hydrogen storage capacities and potential integration with fuel cells but face challenges in regeneration energy costs and byproduct management [37].

- **Organic Hydrogen Carriers (OHCs)**

A more versatile approach is provided by (OHCs), which chemically bind hydrogen in organic molecules and allow controlled release through reversible hydrogenation–dehydrogenation cycles. OHCs can be divided into:

- **Solid Organic Hydrogen Carriers (SOHCs):** high stability and reduced volatility but limited by high release temperatures and catalytic requirements.
- **Liquid Organic Hydrogen Carriers (LOHCs):** liquid under ambient conditions, compatible with existing fuel infrastructure, and attractive for large-scale transport and storage. Notable examples include the toluene/methylcyclohexane pair, dibenzyl toluene, and *N*-heterocyclic compounds such as carbazoles.

LOHCs are particularly attractive because they remain liquid under ambient conditions, show thermophysical properties (viscosity, density, heat capacity) comparable to diesel [38], and can therefore use existing fuel infrastructure with minimal adaptation. They also enable long-term hydrogen storage without self-discharge, making them suitable for seasonal storage and long-distance transport.

The performance of LOHCs, however, is strongly governed by thermodynamic parameters. According to Müller et al. [39], the enthalpy of dehydrogenation should ideally range between 40–60 $kJ \cdot mol^{-1}$ H_2, ensuring a balance between stability and energy input. Moreover, hydrogenation and dehydrogenation reactions should display negative Gibbs free energies under operational conditions, while temperature and pressure directly influence reaction efficiency.

The challenge, therefore, lies in identifying suitable organic derivatives that can reversibly store and release hydrogen at relatively mild conditions while maintaining high

efficiency. Notable examples studied include toluene/methylcyclohexane, dibenzyl toluene, and heteroaromatic systems such as carbazoles and azepines [36, 40, 41].

Within this framework, *N*-heterocyclic compounds—particularly carbazoles and azepines—stand out as promising OHC candidates. Their π-conjugated structures provide tunable electronic properties and high stability, supporting efficient hydrogenation/dehydrogenation cycles while also enabling optoelectronic applications [42-45]. A detailed thermodynamic characterization of these compounds is therefore crucial to assess their suitability as next-generation hydrogen carriers and to guide molecular modifications toward improved performance [46, 47]

- **Cyclic Organic Compounds and Structural Modification**

With the growing interest in cyclic organic compounds for energy storage, significant efforts have been directed toward the development and modification of new molecular structures to improve their efficiency as hydrogen carriers. In 1975, Sultan and Shaw [48] introduced the concept of cyclic organic hydrogen carriers (COHCs) as potential materials for hydrogen storage. Hydrogen storage in these systems is accomplished through catalytic dehydrogenation and subsequent aromatic hydrogenation processes

Cycloalkanes, in particular, have demonstrated promising gravimetric and volumetric hydrogen storage capacities of approximately of 6~8wt% and 60~62 $g \cdot L^{-1}$ [17] respectively. They offer several advantages, including remaining liquid under ambient conditions, compatibility with existing storage and transport infrastructure, abundance, low cost, high reproducibility, and the production of hydrogen with high purity. These characteristics make cycloalkanes attractive candidates for hydrogen storage [49, 50].

However, their main drawback is the relatively low hydrogen storage efficiency, which is directly associated with their high dehydrogenation enthalpies (ΔH_d= 60-70 $kJ \cdot mol^{-1}$ H_2).

The evaluation of thermodynamic properties is essential for determining the reversibility of the hydrogenation/dehydrogenation cycles. From the enthalpy (ΔH) and entropy (ΔS) of reaction, the Gibbs free energy (ΔG) can be obtained as:

$$\Delta G = \Delta H - T\Delta S \qquad (1.1)$$

Hydrogenation reactions are exothermic and thus thermodynamically favourable ($\Delta G < 0$. Conversely, dehydrogenation is endothermic and, at low temperatures (relevant for industrial applications seeking efficiency with reduced energy input), becomes thermodynamically unfavourable ($\Delta G > 0$). A strategy to overcome these limitations is to

structurally modify the carrier molecules in order to optimize their thermodynamic properties. Ideally, ΔG should approach zero, meaning that reversible hydrogenation and dehydrogenation reactions can proceed under analogous and practical conditions.

Four main structural modification approaches have been reported and reviewed:

- **Fusion of organic rings**: Pez et al. [51] demonstrated that increasing the number of fused aromatic rings reduces the endothermicity of dehydrogenation.
- **Introduction of electron-donating substituents**: In addition to the effect of extended conjugation, the incorporation of electron-donating groups into the central ring has also been shown to decrease ΔH_d.
- **Incorporation of heteroatoms into aromatic rings**: Theoretical studies revealed that introducing nitrogen atoms lowers the dehydrogenation enthalpy compared to the corresponding cycloalkane. Density Functional Theory (DFT) calculations indicated that both on-ring and off-ring substitutions reduce ΔH_d. The effect is more pronounced when the nitrogen atom is placed at the meta position, and stronger in five-membered compared to six-membered rings. Beyond nitrogen, oxygen- and sulfur-containing heterocycles have also been investigated.
- **Substitution of protic hydrogen with metals**: He et al. [52] classified this potential group of hydrogen storage materials as metal–organic hydrides, divided into two categories: (1) alkali-metal aliphatic hydrides, and (2) alkali-metal aromatic/cyclic hydrides. In these systems, alkali and alkaline earth metals replace the active hydrogen atom bonded in O–H groups of organic rings. DFT calculations demonstrated that such metalation strategies can tune thermodynamic properties effectively.

1.2 Optoelectronics

Over the years, optoelectronic technologies have been quickly integrated into modern applications, becoming essential tools in daily life. However, their development is far from complete, with ongoing advances in materials and device performance continuing to drive innovation. This progress has enabled the emergence of a new generation of solar-active materials, recognized for their excellent light-harvesting properties and compatibility with solution-based processing methods, thereby supporting the development of flexible and cost-effective photovoltaic systems.

Closely linked to the study of renewable energy storage systems is the field of organic semiconducting materials (OSCs). These materials have attracted significant attention due to their central role in sustainable organic electronic devices, including organic photovoltaics (OPVs), organic field-effect transistors (OFETs), and organic light-emitting diodes (OLEDs) [53-55]. The implementation of photovoltaic devices plays a crucial role in reducing reliance on fossil fuels and accelerating the transition to clean energy sources.

Photovoltaic technology offers several advantages, such as low maintenance requirements, simplified device architectures, and high scalability, making it suitable for applications ranging from microwatt- to megawatt-scale power generation. A key benefit is its ability to convert solar radiation directly into electrical energy with minimal thermal losses, providing an efficient and environmentally friendly alternative to conventional energy systems [56].

- **Organic Photovoltaics (OPVs) and Hole Transporting Materials (HTMs)**

Organic photovoltaics (OPVs) represent a promising approach to solar energy conversion, employing thin organic semiconductors to transform solar radiation into electrical power. Within these devices, hole-transporting materials (HTMs) are essential for facilitating charge mobility, improving device efficiency, and ensuring long-term stability [56].

Compared to *N*-phenylamines, carbazoles possess an additional C–C bond, which induces a hypochromic shift in their UV–Vis absorption bands [57]. This structural modification results in a higher bandgap energy, and, combined with the short π-conjugation of carbazoles, contributes to their elevated triplet energy levels. These characteristics are crucial for optimizing both the efficiency and stability of OPVs and OLEDs, as they enhance charge-transport properties and reduce recombination losses in photovoltaic devices [58].

Azepine derivatives, owing to their non-planar geometry and strong electron-donating ability, have also attracted attention in the field of organic optoelectronics [59] . Their structural flexibility enables efficient charge injection and transport, while their inherent thermal stability makes them suitable for high-vacuum thermal deposition processes used in OLED fabrication. As π-excessive systems, azepines can enhance hole-transporting capability and contribute to improved device durability. Recent studies have demonstrated that dibenzoazepine-based derivatives can function as both hole-transporting and emissive layers in OLEDs, showing promising electroluminescent efficiency and stability. These features position azepine frameworks as versatile building

blocks for the design of next-generation organic semiconductors, complementing the well-established role of carbazoles in OPVs and OLEDs.

1.3 Scope of Dissertation

The initial dissertation project, entitled *"*Thermodynamic study of the effect of bromine as a substituent in *N*-phenylcarbazole and its derivatives*"*, aimed to investigate the energetic–structural influence of halogen substitution in *N*-phenylcarbazoles. The objective was to assess their thermochemical and thermophysical properties through experimental calorimetric and effusion techniques, complemented by computational studies, in order to understand the role of bromination on their stability and performance as potential organic hydrogen carriers and optoelectronic materials. The selected target compounds are shown in Figure 1.1.

However, due to the difficulty of purifying the carbazole derivatives in sufficient quantity and purity within the timeframe of the dissertation, it was not possible to carry out the planned experimental program. To overcome this limitation while preserving the scientific rationale of the project, the study was redirected toward nitrogen-containing heterocycles of comparable relevance. In particular, dibenzoazepine derivatives (iminostilbene, iminodibenzyl, and 5-acetyliminodibenzyl) were selected, as they share structural and electronic features with carbazoles (whose structural formulas are shown in Figure 1.2), offering potential both as organic hydrogen carriers and as functional materials for optoelectronic applications.

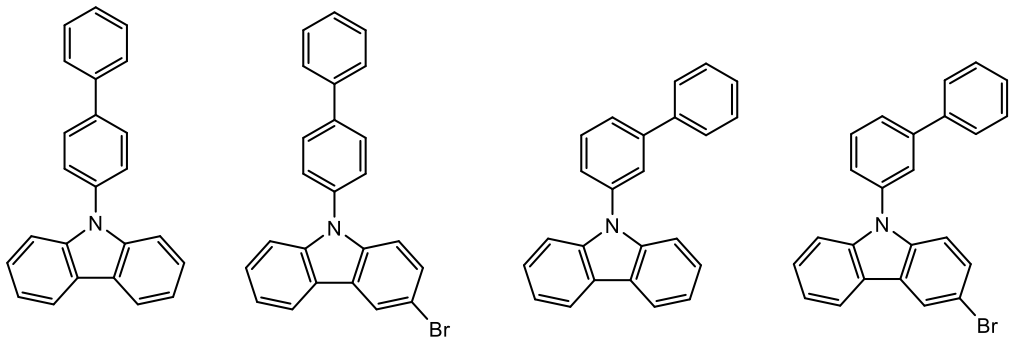

Figure 1.1 Structural formulas of the carbazole derivatives initially proposed for study: (a) 9-([1,1'-biphenyl]-4-yl)-9H-carbazole, (b) 9-([1,1'-biphenyl]-4-yl)-3-bromo-9H-carbazole, (c) 9-([1,1'-biphenyl]-3-yl)-9H-carbazole, and (d) 9-([1,1'-biphenyl]-3-yl)-3-bromo-9H-carbazole.

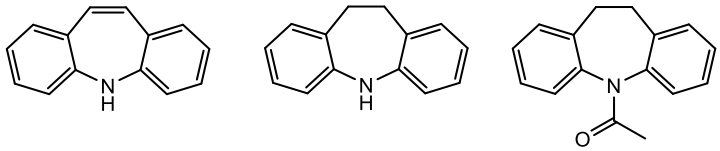

(a) (b) (c)

Figure 1.2 Structural formulas of the azepine derivatives investigated in this dissertation: (a) iminostilbene (b) iminodibenzyl, and (c) 5-acetyliminodibenzyl.

The dissertation was developed through a collaborative effort between the Department of Chemistry and Biochemistry, Faculty of Sciences, University of Porto (FCUP), and Sapienza University of Rome. At FCUP, the purification and structural characterization of the selected azepine derivatives were carried out, along with differential scanning calorimetry (DSC) and Knudsen effusion mass-loss experiments. Complementary theoretical studies were also performed at FCUP, aiming to determine the hydrogenation enthalpies of the azepines and to provide insight into their thermodynamic behaviour. At Sapienza, advanced thermophysical investigations were conducted, including Knudsen effusion mass spectrometry (KEMS), Knudsen effusion mass-loss (KEML), and thermogravimetric analysis (TG). This integrated experimental–theoretical approach ensured a comprehensive assessment of the thermodynamic and thermophysical properties of the selected nitrogen heterocycles.

1.3.1 Carbazoles

Carbazole is an aromatic heterocyclic compound with a planar tricyclic structure, consisting of two benzene rings fused to a five-membered nitrogen-containing ring. Carbazole derivatives have recently been explored as hydrogen storage materials, since their structural features and chemical versatility make them promising candidates for advanced organic hydrogen carriers (OHCs). For many years, organic compounds were not considered viable for hydrogen storage due to the difficulty of promoting reversible hydrogen release at low temperatures. However, recent advances have expanded the understanding of these compounds, opening new possibilities for their application [17].

Beyond hydrogen storage, carbazoles are well known for their optoelectronic properties, being widely used in OLEDs and organic photovoltaics (OPVs) [60]. Moreover, carbazole derivatives play an important role in medicinal chemistry, as they occur in natural products with reported antitumour [61], antibiotics [62] and antioxidative activity [63].

1.3.2 Azepines

Azepines are a class of heteroaromatic compounds characterized by a seven-membered central ring containing a nitrogen atom. Their derivatives, particularly dibenzoazepines, are stable and chemically versatile, attracting significant attention in both medicinal and materials chemistry due to their structural flexibility and electron-donor profile [64].

They have been investigated as building blocks in pharmacology (e.g., antidepressant and anticonvulsant agents) and in materials science as organic semiconductors. In contrast, no systematic studies have been reported on azepines as hydrogen carriers. Nevertheless, their π-conjugated frameworks and strong electron-donor character—features that parallel those of carbazoles—suggest that they could be explored as potential candidates for reversible hydrogen storage. This hypothesis provides the rationale for their inclusion in the present dissertation, where iminostilbene (IMB), iminodibenzyl (IDB), and 5-acetyliminodibenzyl (AcIDB) were selected for detailed thermodynamic investigation (Figure 1.2)

1.3.3 Applications

- **Carbazoles and Azepines as LOHCs**

Among heteroaromatic systems, *N*-ethylcarbazole (Figure 1.3) has been widely investigated as a prototypical liquid organic hydrogen carrier (LOHC), owing to its favourable thermodynamic and kinetic properties. Pez et al. [51] demonstrated that this compound can achieve a hydrogen storage capacity of ca. 5.8 wt% upon full hydrogenation, and about 5.2 wt% under lean hydrogen conditions. Despite these advantages, its relatively high melting point limits practical application. To address this challenge, several strategies have been proposed, including the introduction of allylic and aromatic substituents (e.g., benzylcarbazole, with structural formula in figure 1.3) [38], the incorporation of heteroatoms, or the use of eutectic mixtures. For instance, Stark et al. [22]. showed that substituting the ethyl group with a propyl group decreases the melting point by ~20 K, thereby enhancing the processability of eutectic systems.

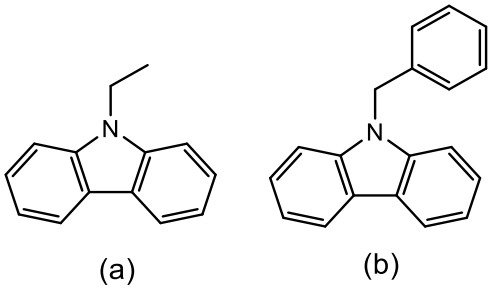

Figure 1.3 Structural formulas of 9-ethylcarbazole (a) and 9-benzylcarbazole (b).

In contrast, azepines have been primarily studied in photonics and medicinal chemistry, with no systematic reports on their use as hydrogen carriers. However, given their π-conjugated frameworks and electron-donor character, features that parallel those of carbazoles, they can be hypothesized as potential candidates for reversible hydrogen storage, a possibility that this dissertation seeks to explore.

- **Carbazole and Azepines in Photonics**

Beyond their role in hydrogen storage, carbazole derivatives are widely recognized for their importance in optoelectronics, owing to their excellent charge-transport properties, photoconductivity, and light-emitting behaviour. Their strong electron-donating character makes them attractive materials for organic semiconductors, including organic light-emitting diodes (OLEDs), organic field-effect transistors (OFETs), and organic photovoltaics (OPVs).

Compared with purely fluorescent materials, phosphorescent emitters are more efficient because they can utilize nearly 100% of the generated excitons in OLED devices. Thermally activated delayed fluorescence (TADF) has emerged as a promising strategy to improve OLED performance, exploiting a small energy gap between singlet (S1) and triplet (T1) states to facilitate reverse intersystem crossing (RISC) without the need for heavy metals [60].

Functionalization of organic semiconductors with heteroatoms has proven effective in designing TADF materials, as it enhances spin–orbit coupling — a relativistic effect arising from the interaction between the electron spin and its orbital angular momentum. While transition-metal complexes can achieve this efficiently, they often suffer from poor solubility in low-polarity environments, which limits their applicability. To address this, organic strategies such as the heavy atom effect (HAE) have been explored. Halogenation, for instance, has been shown to induce phosphorescence in organic systems like naphthalimide and fluorene derivatives [65]. HAE enhances spin–orbit

coupling, increasing RISC rates and enabling higher triplet-state utilization in phosphorescent OLEDs (PhOLEDs) and TADF devices [66].

Malinge et. al [21] systematically investigated the impact of halogenation on the photophysical properties of semiconducting materials, demonstrating that bromination enhances phosphorescence efficiency while reducing fluorescence intensity. They also showed that the number and position of halogen atoms affect the vibronic features of the phosphorescence spectra, although the fluorescence profile remains largely unaffected. In carbazole derivatives, bromine substitution induces a redshift in emission and an increase in vibronic peak intensity, particularly when introduced at substituent positions, whereas central-ring substitution leads to negligible changes. These findings suggest that bromination modifies the vibrational wave function of the triplet state, influencing Franck–Condon factors and the intensity of vibronic transitions.

Azepine derivatives have also attracted attention in optoelectronics due to their non-planar geometry, high electron-donating ability, and excellent thermal stability [59]. These properties enhance charge injection and transport, while ensuring morphological durability in multilayer devices. Consequently, azepines are promising candidates as both hole-transporting and light-emitting materials in OLEDs [67]. Danel et al [68], reported blue-emissive anthracene derivatives functionalized with dibenzoazepine and dihydrodibenzoazepine, designed to enhance hole-transport properties. Among the studied hole-transporting materials (HTMs), the iminodibenzyl (IDB)-substituted compound exhibited higher brightness and external quantum efficiency (EQE) compared with the iminostilbene (IMB) derivative, although both devices demonstrated a similar turn-on voltage of 3.5 V.

Further evidence of the potential of azepines in OLEDs was provided by Lei et al. [15], who synthesized and characterized two azepine–pyridine–carbonitrile compounds incorporating IDB and IMB substituents. The IDB-based derivative displayed a photoluminescence quantum yield of 95%, a small singlet–triplet energy gap (ΔE_{ST}), and an efficient RISC process, achieving an EQE of 39.6%. In contrast, the IMB derivative reached only 14.6%. Structural differences explain this performance gap: the absence of the central-ring double bond in IDB allows better alignment with the emission axis, thereby promoting outcoupling efficiency.

2. Methodologies

2.1. Methodologies for the Study of Crystal-Crystal and Crystal-Liquid Transitions

The investigation of crystal-crystal and crystal-liquid transitions provides key insights into the energetic and structural stability of condensed phases. These transitions involve either rearrangements between different crystalline forms (polymorphic transformations) or the disruption of long-range order during melting. From a thermodynamic perspective, they are characterised by well-defined enthalpy and entropy changes, which can be directly quantified using calorimetric methods. In this work, particular emphasis is placed on the combination of differential scanning calorimetry (DSC) and thermogravimetric analysis (TGA). These techniques allow the accurate determination of transition temperatures, enthalpies of fusion, and related thermodynamic parameters, thus providing the experimental foundation for the study of condensed-phase energetics.

- **Thermodynamic framework**

Thermodynamics provides the basis for understanding the energetic changes associated with physical and chemical processes. According to the first law of thermodynamics, the internal energy of an isolated system remains constant and its variation can be expressed as:

$$\Delta U = q + w \tag{2.1}$$

where q is the heat exchanged with the surroundings and w is the work performed on the system.

At constant volume, expansion work is negligible ($dw_{\mathrm{exp}} = 0$), and therefore:

$$\Delta U = q_V \tag{2.2}$$

This relation is central to calorimetry, which quantifies heat exchange during physical or chemical transformations. In calorimetric experiments, the measured temperature change ΔT is directly related to the heat absorbed or released. The proportionality constant is the heat capacity, defined as:

$$dq = C\ dT \tag{2.3}$$

For a system at constant volume:

$$C_V = \left(\frac{\partial q}{\partial T}\right)_V = \left(\frac{\partial U}{\partial T}\right)_V \tag{2.4}$$

At constant pressure, the relevant thermodynamic potential is enthalpy:

$$H = U + pV \tag{2.5}$$

and the corresponding heat capacity is:

$$C_p = \left(\frac{\partial q}{\partial T}\right)_p = \left(\frac{\partial H}{\partial T}\right)_p \tag{2.6}$$

During a phase transition, the system absorbs or releases a characteristic amount of energy. For melting, this is the molar enthalpy of fusion, $\Delta^{\mathrm{l}}_{\mathrm{cr}}H_{\mathrm{m}}$, observed at the melting T_{fus}. The Clapeyron equation provides the slope of the phase boundary:

$$\frac{dp}{dT} = \frac{\Delta^{\mathrm{l}}_{\mathrm{cr}}H_{\mathrm{m}}}{T_{\mathrm{fus}}\Delta^{\mathrm{l}}_{\mathrm{cr}}V_{\mathrm{m}}} \tag{2.7}$$

where $\Delta^{\mathrm{l}}_{\mathrm{cr}}V_{\mathrm{m}}$ is the molar volume change for the process of fusion.

In the absence of chemical or physical transformations, the heat capacity may be treated as temperature-independent, allowing the enthalpy variation between two states to be determined from eq. (2.8) where T_1 and $T_2$are the initial and final temperature respectively.

$$\Delta H = \int_{T_1}^{T_2} C_p dT \tag{2.8}$$

- **Thermal Analysis**

Thermal analysis comprises techniques in which a physical property of a material is measured as a function of temperature or time under controlled heating or cooling. In this work, two techniques were applied to study crystal–crystal and crystal–liquid transitions: Differential Scanning Calorimetry (DSC) and Thermogravimetric Analysis (TGA). These methods provide complementary information, since DSC quantifies heat effects while TGA monitors changes in sample mass.

2.1.1. Differential Scanning Calorimetry (DSC)

DSC is based on the continuous comparison between a sample and a reference subjected to the same temperature program. The recorded signal is proportional to the heat flow difference:

$$\Delta\phi = \phi_S - \phi_R \tag{2.9}$$

where ϕ_S and ϕ_R are the heat flows of the sample and reference, respectively.

Two instrument designs are widely used:

- *Heat flux DSC*, where both crucibles are placed in the same furnace and the heat flow is inferred from the measured temperature difference.
- *Power compensation DSC*, where sample and reference are maintained in separate furnaces and power is continuously adjusted to minimize temperature differences.

Experiments can be conducted in dynamic mode (temperature programmed) or in isothermal mode (constant temperature). In this work, most measurements were performed in dynamic mode, using hermetically sealed aluminium crucibles and controlled heating rates.

Accurate results require temperature and enthalpy calibration, carried out with reference materials of known transition temperatures and enthalpies. This ensures reliable determination of onset melting temperatures and enthalpies of fusion, which are critical to assess purity, crystallinity, and polymorphism.

2.1.2 Thermogravimetric Analysis (TGA)

TGA records the mass of a sample as a function of temperature or time. Typical outputs include the thermogravimetric curve (mass vs. temperature) and its derivative (DTG), which highlights the rates of mass loss. This technique allows the study of decomposition, desolvation, oxidation, and volatilisation processes.

When performed under vacuum or controlled gas flow, TG data can be also used to estimate vapour pressures through a Langmuir-type relation. In its standard form (ideal case, effective area S, instantaneous rate dm/dtdm/dtdm/dt):

$$p = \frac{1}{\alpha' S} \cdot \frac{dm}{dt} \cdot \sqrt{\frac{2\pi RT}{M}} \tag{2.10}$$

where M is the molecular weight, S the effective surface area of the sample, α' the vaporisation coefficient, R the gas constant, and T the absolute temperature.

2.1.3 Experimental setups

- **Differential Scanning Calorimetry (DSC)**

DSC measurements were performed on a *NETZSCH DSC 204 F1 Phoenix* heat-flux calorimeter equipped with an intracooler unit, allowing operation down to 188 K. Heating rates of 2 and 10 K·min⁻¹ were used. Temperature and heat flow calibrations were carried out at the same heating rates using recommended reference standards: indium (T_{fus} = 429.75 K, $\Delta^{\mathrm{l}}_{\mathrm{cr}}H$ = 28.6 J·g⁻¹), tin (T_{fus} = 505.05 K, $\Delta^{\mathrm{l}}_{\mathrm{cr}}H$ = 60.54 J·g⁻¹), bismuth (T_{fus} = 544.55 K, $\Delta^{\mathrm{l}}_{\mathrm{cr}}H$ = 53.14 J·g⁻¹), adamantane (T_{trans} = 208.65 K, $\Delta^{\mathrm{cr,I}}_{\mathrm{cr,II}}H$ = 22.0 J·g⁻¹), diphenyl ether (T_{fus} = 300.01 K, $\Delta^{\mathrm{l}}_{\mathrm{cr}}H$ = 101.15 J·g⁻¹), biphenyl (T_{fus} = 342.08 K, $\Delta^{\mathrm{l}}_{\mathrm{cr}}H$ = 120.6 J·g⁻¹), naphthalene (T_{fus} = 353.38 K, $\Delta^{\mathrm{l}}_{\mathrm{cr}}H$ = 147.6 J·g⁻¹), and benzoic acid (T_{fus} = 395.50 K, $\Delta^{\mathrm{l}}_{\mathrm{cr}}H$ = 147.2 J·g⁻¹). Each calibrant was analysed in triplicate.

Approximately 6–9 mg of sample was loaded into Concavus® aluminium crucibles (30 µL), weighed with a precision of ±0.1 µg using a Mettler Toledo UMT2 balance. Crucibles were hermetically sealed and placed in the calorimeter cell, with an identical empty pan used as reference. A constant nitrogen purge (Air Liquide, 99.999%) was applied at a flow rate of 40 cm³·min⁻¹. Instrument control and data treatment were performed using the *Proteus Thermal Analysis* software (version 8.0.3, NETZSCH).

The DSC experiments were performed under ambient laboratory pressure conditions, typically 101.3 kPa (± 2 kPa). Although the pressure was not actively controlled, this range reflects standard laboratory atmosphere during the experiments, with pressure variations (Δp) considered negligible.

Concavus® crucibles were selected as they provide improved reproducibility compared with standard aluminium crucibles, particularly in terms of enthalpy and onset temperature measurements.

- **Simultaneous Thermal Analysis (STA)**

TG/DSC measurements were performed using a *Stanton Redcroft 625 STA* system, coupled to a 386 IBM-compatible computer. Calibration was carried out with high-purity indium and tin standards, depending on the temperature range investigated.

Non-isothermal experiments were conducted under a stream of synthetic air to evaluate the oxidative behavior of the compounds. Sample masses ranged between 4

and 6 mg, placed in Concavus® aluminum crucibles. Heating rates were adapted to the experimental requirements and are reported with each dataset.

2.2 Methodologies for the Study of Crystal-Gas Transition

The study of crystal-gas transitions is fundamental for understanding sublimation processes, vapour pressure determination, and the thermodynamic stability of solid compounds. Unlike crystal-crystal or crystal-liquid transformations, which can be directly probed by calorimetric methods, crystal-gas transitions require indirect approaches combining theory and experiment. The kinetic theory of gases provides the microscopic basis for describing molecular fluxes, while effusion techniques, such as Knudsen effusion, allow the determination of equilibrium vapour pressures. More recently, quartz crystal microgravimetry has emerged as a sensitive tool to follow sublimation kinetics with small sample amounts. In this section, the theoretical framework and the experimental methodologies used for the investigation of crystal–gas transitions are presented.

2.2.1. Kinetic Theory of Gases

The kinetic theory of gases provides a connection between the microscopic motion of molecules and the macroscopic properties of gases. It is based on a set of simplifying assumptions that define the ideal gas model.

- **Assumptions of the Ideal Gas Model**

For an ideal gas, the following assumptions are made:

1. The gas contains a very large number, N, of identical molecules, each with the same mass, *m*;
2. Molecules obey Newton's laws of motion and are in continuous, random, and isotropic motion;
3. The molecular size is negligible compared with the average intermolecular distance; therefore, the volume of individual molecules can be disregarded relative to the molar volume of the gas
4. Collisions between molecules and the container walls are perfectly elastic;
5. The container is assumed to be a rectangular box;
6. The gas is monoatomic (e.g., noble gases), so molecules possess only translational kinetic energy, without rotational or vibrational contributions.

- **Derivation of the Ideal Gas Law**

Collisions between molecules do not explicitly appear in the derivation of the ideal gas law. Because molecules move with random velocities, intermolecular collisions merely redistribute momentum, ensuring that the overall motion remains isotropic. Although the number of collisions with a particular wall fluctuates over short time and spatial scales, the very large number of molecules guarantees that only the statistical average is relevant.

This statistical approach allows the calculation of the average force exerted by molecules on the container walls, which in turn demonstrates the connection between temperature and molecular kinetic energy.

Consider a molecule moving along the x-axis inside a cubic box of side l. Its momentum, p, changes from $-mv_x$ to $+mv_x$ after colliding elastically with the wall, so, $\Delta p = 2mv_x$.

The average force exerted by this molecule is:

$$F_i = \frac{\Delta p_i}{\Delta t} = \frac{2mv_x}{\Delta t} \tag{2.11}$$

The force between the wall and the molecule acts only during the instant of collision; at that moment, it is very large. However, since the average force is required, the appropriate time scale is the average time between successive collisions of the same molecule with the wall, $\Delta t = {}^{2l}/_{v_x}$

Substituting into Eq. (2.11):

$$F_i = \frac{\Delta 2mv_x}{\Delta 2l/v_x} = \frac{mv_x^2}{l} \tag{2.12}$$

For N molecules:

$$F = N\frac{m\langle v_x^2\rangle}{l} \tag{2.13}$$

Since molecular motion is isotropic:

$$\langle v^2\rangle = \langle v_x^2\rangle + \langle v_y^2\rangle + \langle v_z^2\rangle = 3\langle v^2\rangle \tag{2.14}$$

Therefore,

$$F = N\frac{m\langle v^2\rangle}{3l} \tag{2.15}$$

Using $p = {}^{F}/_{A}$ and $V = Al$,

$$pV = \frac{1}{3}Nm\langle v^2\rangle \tag{2.16}$$

Comparison with the ideal gas law,

$$pV = NK_BT \tag{2.17}$$

leads to:

$$\frac{1}{3}Nm\langle v^2\rangle = Nk_BT \tag{2.18}$$

- **Temperature and Molecular Kinetic Energy**

Eq. (2.18) leads directly to the expression for the average translational kinetic energy per molecule:

$$\langle K\rangle = \frac{1}{2}m\langle v^2\rangle = \frac{3}{2}k_BT \tag{2.19}$$

This expression shows that molecular kinetic energy depends solely on the temperature of the system.

In mixtures containing molecules of different masses, all species at the same temperature share the same average translational kinetic energy. When two systems at different temperatures come into contact, collisions transfer energy from the more energetic molecules of the hotter system to the molecules of the cooler one. On the macroscopic scale, this process corresponds to heat flow.

Thermal equilibrium is reached when no net heat transfer occurs, i.e., when both systems are at the same temperature.

2.2.2. Effusion and Knudsen Method

Effusion is the process by which gas molecules escape from a container through a very small orifice into vacuum conditions, without collisions between the escaping molecules and without disturbing the equilibrium inside the container. This phenomenon differs from diffusion, which results from concentration gradients in open systems.

- **Importance of Vapor Pressure**

The vapor pressure of a substance is a key thermodynamic property that describes its tendency to transition from the condensed to the gas phase. Accurate determination of vapor pressure plays a pivotal role across various scientific and technological domains, offering insights into volatility, thermal stability, and phase behaviour. This information is critical when assessing environmental dispersion, processing conditions, shelf-life, and storage stability, as well as in the design of materials for pharmaceutical, agrochemical, and energy-related applications.

From a thermodynamic perspective, vapor pressure measurements enable the determination of enthalpies and entropies of sublimation or vaporization and provide critical input for calculating gas-phase enthalpies of formation. Such values are required to construct thermochemical cycles, model reaction energetics, and validate quantum chemical predictions.

- **Principles of Knudsen Effusion**

Some experimental techniques are available for vapor pressure determination, and the choice of method depends on the volatility of the compound, thermal stability, physical state (solid or liquid), and the applicable temperature range, often limited by instrumental constraints. Among these approaches, effusion methods using Knudsen cells have proven particularly effective for determining the equilibrium vapor pressures of solid compounds under high-vacuum conditions.

A Knudsen cell is a temperature-controlled container, typically cylindrical, with a precisely defined orifice in its lid that connects the interior to a vacuum chamber. Inside the cell, the sample is in equilibrium with its vapor. Molecules effuse through the orifice, and provided that molecular flow conditions are established ($Kn > 1$), intermolecular collisions are negligible. Under these conditions, the equilibrium vapor pressure inside the cell can be directly related to the molecular flux through the orifice.

This approach relies on the assumptions of the kinetic theory of gases: molecules move randomly and isotropically, collisions with the orifice dominate over intermolecular collisions, and the equilibrium inside the cell remains undisturbed.

The versatility of Knudsen effusion methods lies in their ability to provide complementary types of information. Depending on the experimental setup, they can be used to determine mass loss - in the Knudsen Effusion Mass Loss (KEML) method - or the gas-phase composition of the effusing vapor - in Knudsen Effusion Mass Spectrometry

(KEMS). This duality enables the simultaneous acquisition of vapor pressure data and detailed insight into the molecular composition of the vapor phase (Figure 2.1).

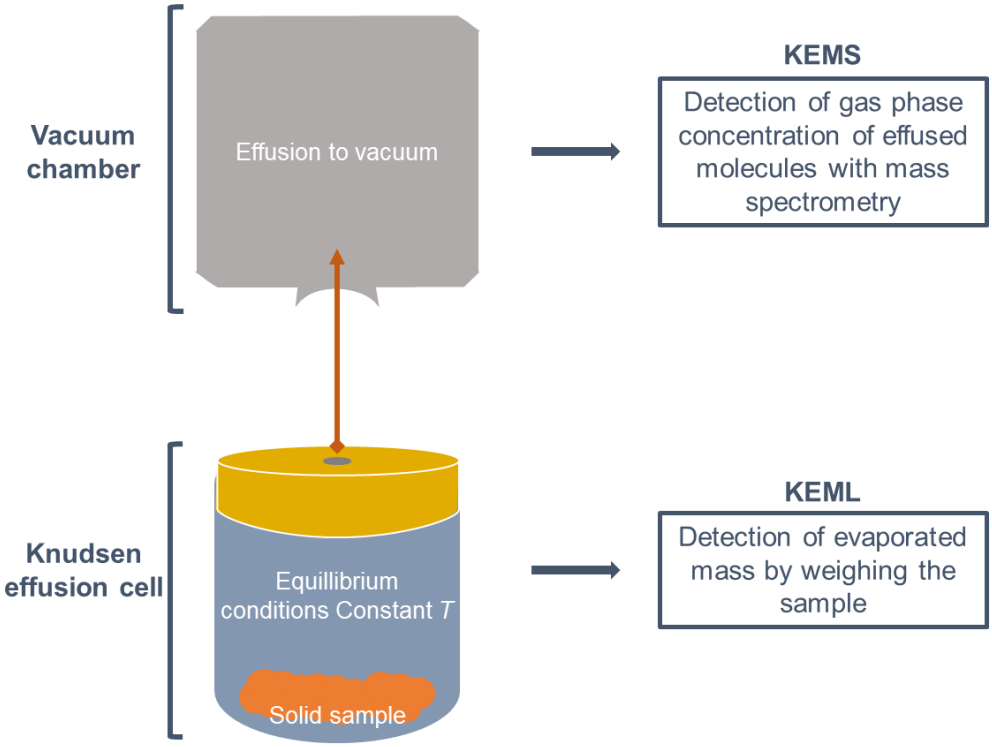

Figure 2.1 Schematic representation of the Knudsen effusion method, illustrating the two main experimental approaches: mass loss determination (KEML) and gas-phase composition analysis (KEMS).

- **Ideal Knudsen Effusion**

In its ideal formulation, the Knudsen effusion method is based on monitoring the mass loss of vapor molecules effusing through the orifice of the cell. The cell, containing the condensed phase in equilibrium with its vapor, is placed in a vacuum chamber at very low pressures and at controlled temperature.

For the ideal case, the following assumptions apply:

1. The vapor is uniformly distributed within the cell;
2. The orifice has negligible thickness;
3. The orifice diameter is much smaller than the mean free path of the molecules. Otherwise, intermolecular collisions near the orifice generate a collective flow, and the molecular flux no longer strictly follows the Maxwell–Boltzmann velocity distribution, invalidating the effusion assumption.

If these conditions are not satisfied, intermolecular collisions near the orifice generate a collective flow, and the molecular flux deviates from the Maxwell–Boltzmann distribution, invalidating the effusion assumption.

Under ideal assumptions, the vapor pressure is related to the measured mass loss by:

$$p = \frac{m}{A_0 t}\left(\frac{2\pi RT}{M}\right)^{1/2} \tag{2.20}$$

where m is the mass of effused vapor in time t, $A_0$the orifice area, M the molar mass, R the gas constant, and T the temperature.

This relation is consistent with Graham's law of effusion, which states that the rate of effusion is inversely proportional to the square root of the molar mass ($1/\sqrt{M}$).

- **Real Systems and the Clausing Factor**

In practical systems, the finite thickness of the orifice implies that some molecules collide with its walls: some return to the cell, while others escape. To correct for this effect, the Clausing factor, ω_0, is introduced, which quantifies the transmission probability of molecules through the orifice:

$$w_0 = \left[1 + \frac{3l}{8r}\right]^{-1} \tag{2.21}$$

where l is the thickness of the orifice and r its radius.

Considering this correction, the expression for vapor pressure becomes:

$$p = \frac{1}{w_0} \cdot \frac{m}{A_0 t}\left(\frac{2\pi RT}{M}\right)^{1/2} \tag{2.22}$$

The geometry of the orifice, particularly the l/r ratio, is therefore critical to ensure molecular flow and to avoid disturbing the solid–vapor equilibrium inside the cell.

- **Molecular Flow and the Knudsen Number**

Effusion takes place under Knudsen (molecular) flow, a regime in which intermolecular collisions are negligible and molecule–wall collisions dominate. This condition arises at sufficiently low pressures, when the molecular mean free path**,** λ, is much larger than the characteristic dimension of the system, such as the orifice radius, r_0. The mean free path is expressed as:

$$\lambda = \frac{k_B T}{\sqrt{2}\pi\sigma^2 p} \tag{2.23}$$

where σ is the effective molecular collision diameter, p the pressure, and k_B the Boltzmann constant.

The transition between flow regimes is described by the Knudsen number:

$$Kn = \frac{\lambda}{r_0} \tag{2.24}$$

where r_0 is the orifice radius (or another characteristic length scale). For $Kn > 1$, molecular flow conditions prevail, which are required for Knudsen effusion experiments. Typically, this regime is achieved at pressures below ~1 Pa, depending on molecular size.

- **Variants of the Knudsen Method**

In **Knudsen Effusion Mass Loss (KEML)**, the vapour pressure is determined from the rate of mass loss of the condensed sample in the Knudsen cell, applying eqs. (2.20)-(2.22). The method is reliable but limited by the requirement of measurable mass loss. For very low-volatility substances, it often requires extrapolation of high-temperature measurements down to room temperature.

Knudsen Effusion Mass Spectrometry (KEMS) combines the Knudsen cell with a mass spectrometer. After effusing through the orifice, the molecular beam is ionized by electron impact (typically at 70 eV), and ions are analysed according to their mass-to-charge ratio (m/z). A mechanical shutter alternates between beam-on and beam-off positions, separating background signals from those of the effusing species.

The partial pressure of a species x can be calculated from the ion intensity of isotope n:

$$p_x = \frac{K_{instr} I_{nx}^{+} T}{\sigma_x \gamma_{nx} \alpha_{nx}} \tag{2.25}$$

where I_{nx}^{+} is the ion intensity, K_{instr} the calibration constant of the ionization source, *T* is the temperature in K, σ_x the ionization cross section, γ_{nx} the detector gain, and $\alpha_{nx}$the isotopic abundance.

Advantages of KEMS include simultaneous thermodynamic and compositional analysis: it enables detection of secondary reactions, assessment of molecular integrity, study of vaporization pathways, and identification of gas-phase species.

Knudsen effusion techniques remain among the most robust and theoretically grounded methods for vapor pressure determination. Their ability to operate under high-vacuum and molecular flow conditions makes them especially valuable for volatile and thermally labile compounds. The two main variants, KEML and KEMS, provide complementary insights into vapor-phase thermodynamics and composition, making them indispensable tools in the characterization of condensed-phase materials.

2.2.3. Thermodynamic Relations

Depending on the chosen effusion method, different detectors may be employed, such as microbalances or mass spectrometers. Accordingly, the experimental signal may correspond either to the rate of mass loss (KEML) or to the ion current generated by ionization of the effusing vapor species (KEMS). In all cases, these measured quantities must ultimately be related to the equilibrium vapor pressure of the substance through fundamental thermodynamic relations, as derived below.

At equilibrium, the chemical potentials of the two coexisting phases are equal:

$$\mu^{\alpha} = \mu^{\beta} \tag{2.26}$$

$$G_m^{\alpha} = G_m^{\beta} \tag{2.27}$$

For a pure one-component phase, the differential form of the molar Gibbs free energy is:

$$dG_m = -S_m d\mathrm{T} + V_m dp \tag{2.28}$$

Considering two phases in equilibrium (α and β), the condition becomes:

$$-S_m^{\alpha} d\mathrm{T} + V_m^{\alpha} dp = -S_m^{\beta} d\mathrm{T} + V_m^{\beta} dp \tag{2.29}$$

which leads to the Clapeyron equation,

$$\frac{dP}{dT} = \frac{S_m^{\alpha} - S_m^{\beta}}{V_m^{\alpha} - V_m^{\beta}} = \frac{\Delta S_m}{\Delta V_m} = \frac{\Delta S}{\Delta V} \tag{2.30}$$

where ΔS and ΔV are the entropy and volume changes, respectively, associated with the phase transition $\beta \rightarrow \alpha$.

In equilibrium conditions $\Delta S = \Delta H/T$, giving:

$$\frac{dP}{dT} = \frac{\Delta H}{T\Delta V} \tag{2.31}$$

- **Saturation Vapor Pressure**

According to IUPAC, the saturation vapor pressure is the pressure exerted by a pure substance at a given temperature in a closed system containing only its vapor and condensed phase (liquid or solid). Under such conditions:

1. Chemical equilibrium ensures no net molecular flux between phases;
2. Thermal equilibrium ensures uniform temperature;
3. Mechanical equilibrium ensures no stress at the interface.

Thus, the vapor pressure depends exclusively on the molecular interactions of the pure compound in the condensed phase, and it is strongly temperature-dependent.

For a transition involving a condensed phase and vapor, eq. (2.31) can be reformulated as:

$$\frac{dp_i^0}{dT} = \frac{\Delta H_{\mathrm{trs,i}}}{T\Delta v_{\mathrm{trs,i}}} \tag{2.32}$$

where $\Delta H_{trs,\mathrm{i}}$ is the molar enthalpy and $\Delta v_{\mathrm{trs,i}}$ the molar volume change of the transition. For temperatures below the critical point, $\Delta v_{\mathrm{trs,i}}$ can be approximated by the molar volume of the vapor. Assuming ideal-gas behavior, this gives:

$$\frac{dp_i^0(T)}{dT} = \frac{\Delta H_{\mathrm{trs,i}}}{RT^2} p_i^0 \tag{2.33}$$

Integration yields the Clausius–Clapeyron equation:

$$\ln p_i^0(T) = -\frac{\Delta H_{\mathrm{trs,i}}}{RT} + C \tag{2.34}$$

where C is an integration constant related to the reference state and *R* is the molar gas constat.

Accordingly, plotting lnp as a function of $1/T$ allows the enthalpy of sublimation to be determined from the slope.

2.2.4. Quartz Crystal Microgravimetry

Microgravimetric techniques based on quartz crystal microbalances (QCM) have been extensively employed to measure extremely small mass changes [69-71]. This is possible because an increase in mass load on the quartz crystal induces a proportional decrease in its resonant frequency. The method was first introduced by Sauerbrey in 1959 [72, 73] and subsequent studies have demonstrated its high sensitivity to minute variations in solid samples. Unlike Knudsen effusion methods, which operate under equilibrium conditions with mass transport through an orifice, QCM functions under open-cell, non-equilibrium conditions. In this configuration, the sublimation flux is described by a combination of the Clausius–Clapeyron and Hertz–Knudsen relations (eqs. 2.41 and 2.40, respectively). The Sauerbrey equation can be adapted to these conditions, establishing that the rate of frequency change is directly proportional to the rate of mass loss:

$$\frac{df}{dt} \alpha \frac{dm}{dt} \tag{2.35}$$

This proportionality provides the basis for deriving the QCM working equation.

- **Piezoelectric Principle and Quartz Properties**

QCM relies on the ability of a quartz crystal to oscillate at a resonant frequency that varies proportionally with the mass adsorbed on its surface. This behaviour is fundamentally governed by the piezoelectric nature of quartz, which only manifests in crystal structures that lack a center of symmetry. When an alternating electric field is applied to the electrodes deposited on both faces of the quartz disk, the crystal undergoes mechanical oscillation, which is a direct manifestation of the piezoelectric effect. Conversely, mechanical deformation (e.g., pressure) generates a measurable electric charge separation.

The piezoelectric response of quartz is highly dependent on the crystallographic orientation of the cut, i.e., how the disk is sliced from the raw crystal. These quartz crystals are thin disks precisely obtained from macroscopic α-quartz (SiO_2), a naturally piezoelectric form of crystalline silica. Among various cut types (AT, BT, SC, etc.), the AT-cut is the most widely used in scientific and technological applications due to its excellent frequency stability and low temperature sensitivity within a moderate thermal range. In the AT-cut, the quartz disk is cut at an angle of approximately 35°15′ relative to the optical (*Z*) axis and vibrates primarily in the thickness shear mode, making it well-suited for operation in gaseous environments and under vacuum conditions. In this study, 6 MHz

AT-cut quartz crystals (Inficon 750-1000-G10) with 14 mm diameter and gold electrodes were used.

- **Frequency–Mass Relationship**

The Sauerbrey equation derived for thin, rigid, and uniformly deposited films, establishes a linear relationship between the change in resonant frequency and the mass per unit area adsorbed onto the crystal surface, where Δf is the frequency shift, f_0 is the crystal's fundamental frequency, *A* is the active electrode area, ρ_q is the density of quartz (2.648 g·cm^{-3}), and μ_q is its shear modulus.

$$\Delta f = -\frac{2f_0^2}{A \times \sqrt{\mu_\mathrm{q} \times \rho_\mathrm{q}}} \times \Delta m \tag{2.36}$$

This can be simplified to:

$$\Delta f = -S_\mathrm{q} \times \frac{\Delta m}{A} \tag{2.37}$$

where S_q is the theoretical mass sensitivity of the crystal:

$$S_q = \frac{2f_0^2}{\sqrt{\mu_q \times \rho_q}} \tag{2.38}$$

For a 6 MHz AT-cut quartz crystal, the theoretical sensitivity at 298 K is approximately 81.5 MHz·g^{-1}·cm². This implies that a deposition of 12.3 ng·cm^{-2} on the crystal surface leads to a frequency shift of approximately 1 Hz.

Under non-equilibrium conditions, such as open cell configurations, the resonance frequency of the quartz crystal changes dynamically over time. In this regime, the rate of change of frequency is directly proportional to the rate of change of mass on the crystal surface, according to,

$$\frac{df}{dt} = -S_q \frac{dm}{dt} \tag{2.39}$$

- **Thermodynamic Basis**

The determination of the enthalpy of sublimation from quartz crystal microgravimetry data can be derived by combining the Hertz–Knudsen equation with the Clausius–Clapeyron relationship, and by considering the proportionality between mass loss and frequency shift in a quartz crystal microbalance.

The Hertz–Knudsen equation describes the sublimation flux of a substance from a surface under vacuum or rarefied gas conditions, as a function of its vapor pressure and temperature:

$$\frac{dm}{dt} = \alpha\, A\, p \sqrt{\frac{M}{2\pi RT}} \tag{2.40}$$

where dm/dt is the sublimated mass per unit time, *α* is the sublimation coefficient ($0 < \alpha \leq 1$), *A* is the area of the sublimating surface, *p* is the vapor pressure, *M* is the molar mass, *R* is the gas constant, and *T* is the absolute temperature.

The temperature dependence of the vapor pressure is given by the Clausius–Clapeyron equation:

$$p = p_0\, e^{\left(-\frac{\Delta^{\mathrm{g}}_{\mathrm{cr}}H}{RT}\right)} \tag{2.41}$$

Substituting this into the Hertz–Knudsen equation yields:

$$\frac{dm}{dt} = K\, \frac{1}{\sqrt{T}} e^{\left(-\frac{\Delta^{\mathrm{g}}_{\mathrm{cr}}H}{RT}\right)} \tag{2.42}$$

where K groups all constant terms like

$$K = \alpha\, A\, p_0 \sqrt{\frac{M}{2\pi R}} \tag{2.43}$$

Taking the natural logarithm of both sides

$$ln\left(\frac{dm}{dt}\sqrt{T}\right) = -\frac{\Delta^{\mathrm{g}}_{\mathrm{cr}}H}{RT} + ln\, K \tag{2.44}$$

In a quartz crystal microgravimetry system, the change in frequency over time is proportional to the rate of mass loss, therefore it is obtained the working equation:

$$ln\left(\frac{df}{dt}\sqrt{T}\right) = -\frac{\Delta^{\mathrm{g}}_{\mathrm{cr}}H}{RT} + C \tag{2.45}$$

where C is a constant that includes instrumental and material-specific parameters.

This linear relationship enables the determination of the enthalpy of sublimation from the slope of a plot of $ln\left(\frac{df}{dt}\sqrt{T}\right)$ versus $1/T$, measured at different temperatures.

While Knudsen effusion remains the reference method for accurate vapor pressure determination, QCM offers sensitivity to small mass changes and can be advantageous when only small sample amounts are available. Together, these techniques provide complementary approaches to extract sublimation enthalpies across a wide volatility range.

2.2.5. Experimental Setups

2.2.5.1. Knudsen Effusion Mass Loss (KEML)

The Knudsen effusion mass-loss (KEML) method is a gravimetric technique that relates the rate of mass loss of a sample under effusion conditions to its equilibrium vapor pressure. In this work, two different setups were employed: one located at Sapienza University of Rome (SURome), based on continuous monitoring of mass loss with a thermobalance, and another at the Faculty of Sciences of the University of Porto (FCUP), designed for simultaneous measurements with multiple effusion cells.

- **KEML – Sapienza University of Rome (SURome)**

The classical KEML approach relies on monitoring the decrease in sample mass at constant temperature over time. At SURome, this was achieved using a Setaram Ugine-Eyraud Model B60 thermobalance, in which heating is provided by a graphite resistor surrounding a quartz tube that houses the effusion cell assembly. To minimize temperature fluctuations, the cell is enclosed in a copper cylinder, and the sample temperature is measured with a Pt100 platinum resistance thermometer. High-vacuum conditions are maintained by a rotary pump coupled with a diffusion pump.

A key advantage of this setup is the possibility of continuous, automated data acquisition, enabled by a data logger (HP 34970A) interfaced with LabVIEW software, which records both mass and temperature without the need for manual intervention. The vapor pressure is then obtained from the mass-loss rate using the Knudsen relation:

$$p = K\frac{dm}{dt}\sqrt{\frac{T}{M}} \tag{2.46}$$

where T is the absolute temperature, M the molar mass of the effusing vapor, dm/dt the rate of mass loss, and K a constant determined by the geometrical characteristics of the effusion orifice.

It is important to note that the working equation employed at SURome (2.46) is fully consistent with the general Knudsen effusion relation presented earlier, Eq. (2.22). The

expression used in the SURome setup is essentially a compact form of this general relation. Here, the constant K incorporates all geometrical and instrumental factors - namely the orifice area, the Clausing correction, the gas constant, and numerical terms - so that the equation depends only on directly measurable experimental quantities: the rate of mass loss dm/dt, the sample temperature, and the molar mass of the effusing vapor. In practice, however, the determination of K requires the use of reference compounds with well-established vapor pressures, which serve to calibrate the system under the specific experimental conditions.

Thus, both expressions describe the same physical principle, with the difference that the theoretical equation makes explicit the dependence on geometric parameters, while the experimental formulation condenses these factors into an empirically determined constant K.

A schematic representation of the Knudsen effusion mass-loss (KEML) apparatus used at Sapienza University of Rome is shown in Figure 2.2. The setup highlights the main components of the system: the thermobalance for continuous monitoring of sample mass, the graphite heating resistor surrounding the quartz tube, the copper cylinder for thermal stabilization, and the vacuum assembly composed of rotary and diffusion pumps. This configuration ensures precise temperature control and high-vacuum conditions, enabling accurate determination of mass-loss rates during effusion experiments. Together, these elements illustrate the classical design of a single-cell KEML system, optimized for automated data acquisition and reliable vapor-pressure measurements.

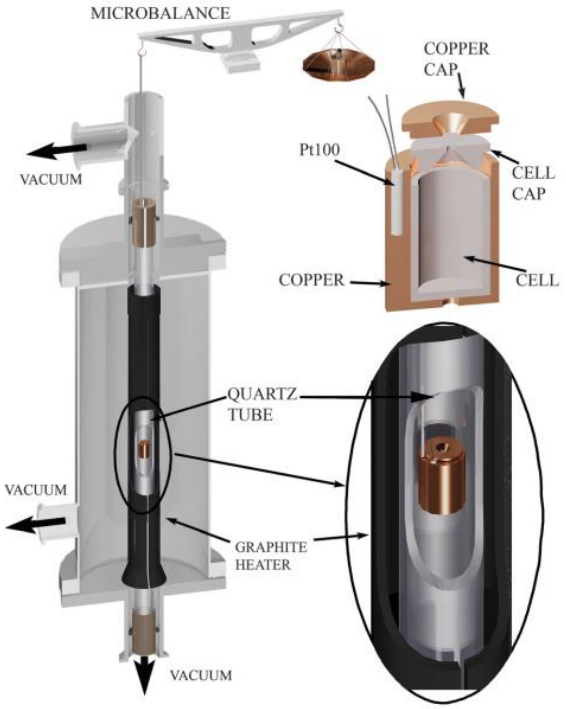

Figure 2.2 Schematic representation of the Knudsen effusion mass-loss (KEML) apparatus used at SURome, showing the microbalance, heating system, quartz tube, and copper cell assembly. Taken from [74].

- **KEML – Faculty of Sciences, University of Porto (FCUP)**

At FCUP, a multichannel effusion apparatus (figure 2.3) was employed, developed by Ribeiro da by Ribeiro da Silva *et al*. [75]. This instrument enables the simultaneous operation of nine effusion cells, arranged in three aluminum blocks inside a vacuum chamber (a glass bell jar with an aluminum lid). Each block contains three cells with different effusion orifice diameters—classified as small (S), medium (M), and large (L)—allowing measurements at three different temperatures and orifice sizes in a single experiment.

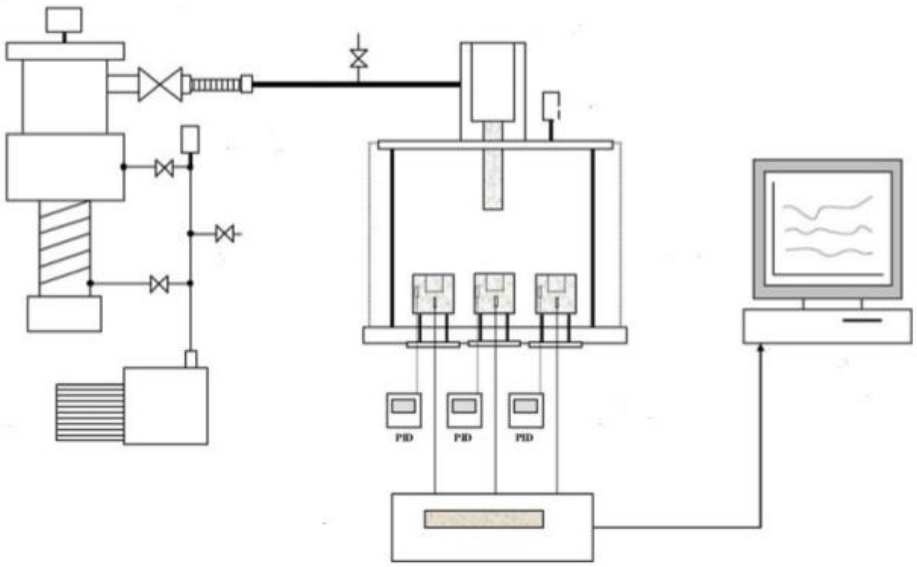

Figure 2.3 Schematic representation of the multichamber Knudsen effusion mass-loss (KEML) apparatus developed at FCUP, allowing simultaneous measurements with nine effusion cells at different temperatures and orifice sizes. Taken from [75].

The system is evacuated using a rotary pump (Edwards RV12) for pre-vacuum, followed by a cryogenically cooled diffusion pump (Edwards CR160). Cooling is provided by a water circuit at the pump base and liquid nitrogen at the top, while a liquid-nitrogen cold finger mounted on the chamber lid prevents contamination of the pumps by sublimed sample molecules.

Prior to each experiment, the samples are compressed inside the effusion cells with a piston to ensure a flat surface for optimal thermal contact, and a thin layer of Apiezon L grease is applied to improve thermal conductivity between the cells and the aluminum block. The cells are weighed before and after the experiment to determine the total mass loss during effusion. Based on extensive experience, a minimum detectable mass loss of 8 mg was established for the smallest orifice at the lowest operating temperature, ensuring reliable vapor pressure determination.

A distinctive advantage of the Porto multiblock KEML system is the simultaneous use of three effusion cells with different orifice sizes (small, medium, and large) operating at the same temperature (figure 2.4). This configuration allows verification that the measured vapor pressure is independent of the orifice diameter, thereby confirming that dynamic equilibrium is maintained inside the Knudsen cell. Such cross-validation minimizes systematic errors related to geometry effects and provides additional reliability to the vapor pressure determination.

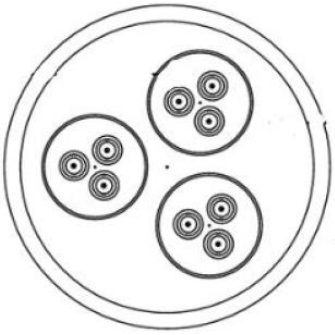

Figure 2.4 Top view of the multiblock Knudsen effusion mass-loss (KEML) oven at FCUP, illustrating the arrangement of nine effusion cells divided into three blocks, each operating at a different temperature and orifice size. Taken from [75].

- **Comparison of the two approaches**

The main distinction between the two KEML setups lies in the mode of mass determination. At SURome, mass loss is tracked continuously throughout the experiment with a thermobalance, offering high temporal resolution. In contrast, at FCUP, mass is determined by weighing the effusion cells before and after the experiment, with nine cells operating in parallel. This configuration not only provides high throughput but also enables direct comparison across different temperatures and orifice sizes in a single run.

A distinctive advantage of the Porto system is the simultaneous use of three cells with different orifice diameters at the same temperature, which allows verification that the measured vapor pressure is independent of the orifice size. This serves as a stringent test for equilibrium conditions inside the Knudsen cell, ensuring that deviations from the ideal effusion regime can be identified and corrected.

Despite their different designs, both systems operate under Knudsen effusion conditions and provide consistent access to equilibrium vapor pressures and sublimation enthalpies of low-volatility compounds.

2.2.5.2. Knudsen Effusion Mass Spectrometry (KEMS)

The Knudsen effusion mass spectrometry (KEMS) apparatus combines a Knudsen molecular effusion source with a high-resolution mass spectrometer, enabling simultaneous measurement of vapor pressures and identification of gas-phase species. The setup can be divided into four main parts: the sample system, the ionization source, the analyser, and the detector (Figure 2.5).

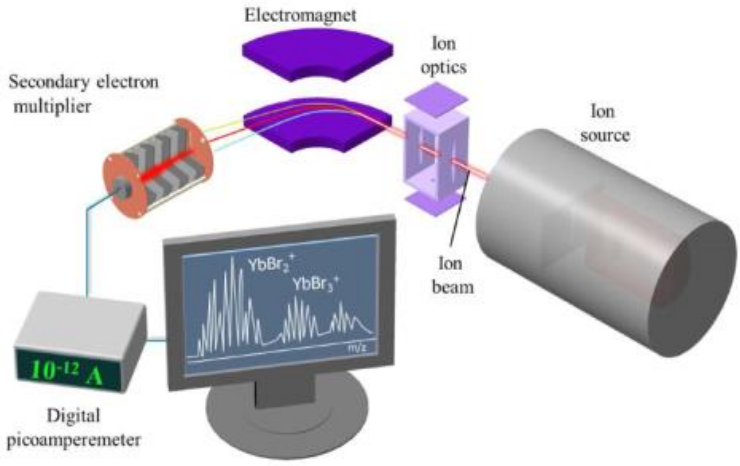

Figure 2.5 Schematic representation of magnetic sector of Knudsen Efusion mass spectrometer. Taken from ref. [76].

The effusion cell is made of platinum, fitted with a 1 mm diameter orifice, and placed inside an outer tantalum crucible. Heating is provided by a spiral-shaped tungsten element, surrounded by tantalum heat shields to ensure thermal uniformity. Temperature is continuously monitored by a Pt/Pt–13%Re thermocouple located at the base of the tantalum crucible. A schematic of a generic Knudsen molecular source is presented in Figure 2.5, while Figure 2.6 provides a detailed view of the effusion source assembly integrated into the spectrometer.

The cell is loaded with a sufficient amount of sample to cover its bottom surface, and the system is evacuated to high-vacuum conditions (~10^{-6} Pa). Heating is achieved by passing a high current (10–200 A) through the tungsten filaments until the desired temperature is reached. Once thermal stability is established, as monitored by the thermocouple, measurements can begin.

Ionization of the effusing vapor is performed by electron impact (typically 70 eV), with ions detected by a secondary electron multiplier. A mechanical shutter alternates between beam-on and beam-off positions to discriminate background signals. The measured ion intensities are converted to partial pressures using Eq. (2.25), and enthalpies of sublimation are obtained from Clausius–Clapeyron plots, calibrated with reference compounds of known vapor pressures.

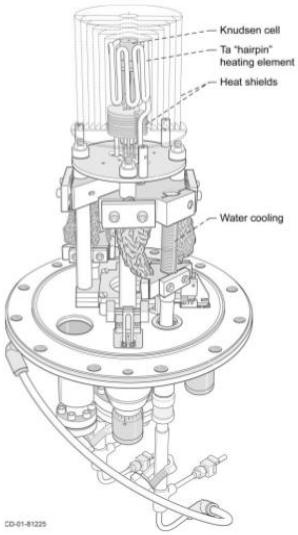

Figure 2.6 Knudsen molecular effusion source integrated into a single-focusing mass spectrometer, showing the effusion cell, tantalum heating element, thermal shields, and water-cooling system. Taken from [77].

2.2.5.3. Quartz Crystal Microbalance (QCM)

The QCM system employed in this work is located at the Department of Basic and Applied Sciences for Engineering (SBAI), Sapienza University of Rome. It is a prototype apparatus, originally developed for the study of ionic liquids at lower temperatures, inspired by the work of Verevkin et al. [78].

The setup consists of three main components: the quartz crystal microbalance, the sample holder with heating element, and the vacuum system (Figure 2.7). A rotary pump provides the pre-vacuum stage, after which a turbomolecular pump (Adixen ADH) is activated to achieve high vacuum conditions compatible with sublimation studies.

The crystal is a 6 MHz AT-cut quartz disk (Inficon 750-1000-G10), 14 mm in diameter and gold-coated, mounted in a BSH-150 sensor head to ensure stable electrical contact. Its resonant frequency is monitored by an STM-2 USB thin-film controller enclosed in a Faraday cage to reduce noise. The crystal is positioned 25 mm above the sample holder.

Heating is provided by a resistive element connected to a variable power supply, with temperature monitored by a Pt100 resistance sensor embedded in the block. A shutter mechanism installed in the chamber lid allows controlled exposure of the crystal to the sublimating sample.

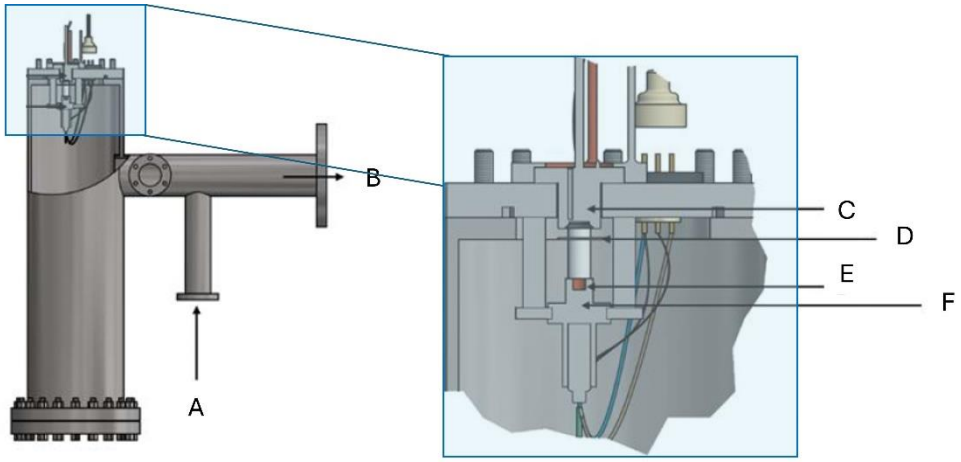

Figure 2.7 Schematic of the quartz crystal microgravimetry setup A. atmosphere inlet valve; B. vacuum system; C) quartz-crystal microbalance; D) shutter; E) sample holder and F) heating element.

2.2.6. Data Treatment

The experimental measurements obtained from Knudsen effusion experiments were processed to extract vapor pressures, sublimation enthalpies, and the corresponding thermodynamic functions. The procedure involves the following steps:

- **Determination of Vapor Pressures**

For each experimental technique, the equilibrium vapor pressure was obtained from directly measurable quantities:

- **KEML–FCUP**: the mass of each effusion cell was determined before and after the experiment. The total mass loss was used to calculate the average mass-loss rate and corresponding vapor pressure, again corrected with the appropriate Clausing factor (Eq. 2.22). For each compound, individual plots of lnp versus $1/T$ are constructed using data from the small, medium, and large orifices, as well as a combined plot including all experimental points. The comparison of these representations enables verification of equilibrium conditions inside the Knudsen cells, as vapor pressures should remain independent of the orifice diameter.

- **KEML–SURome**: the mass loss was continuously recorded with a thermobalance, and the vapor pressure calculated from the rate of mass loss using the Knudsen relation (Eq. 2.46), where the constant K incorporates the Clausing factor and other geometric terms specific to the effusion cell. The setup employed effusion cells with a fixed orifice diameter of 1 mm, so verification of

equilibrium conditions through comparison of multiple orifice sizes was not possible.

- **KEMS**: the ion intensities measured by the mass spectrometer were converted into partial vapor pressures using Eq. (2.25), with instrumental calibration performed against reference compounds of known vapor pressure.

- **Enthalpy of Sublimation**

The standard molar enthalpy of sublimation at the mean experimental temperature, $\langle T \rangle$, is derived from the slope of the linear regression of the Clausius–Clapeyron plot:

$$lnp = a - b/T \tag{2.47}$$

where a is a constant and b corresponds to $-\Delta_{cr}^{g} H_m(\langle T \rangle)/R$, with ($R$ = 8.3144621 J·K^{-1}·mol^{-1} [79])

$$\Delta_{cr}^{g} H_m(\langle T \rangle) = -R \cdot \text{slope} \tag{2.48}$$

From the slopes of these linear fits, the standard molar enthalpies of sublimation at the mean experimental temperature, $\Delta_{cr}^{g} H_m^{\circ}(\langle T \rangle)$, were derived. The corresponding molar entropies of sublimation, $\Delta_{\mathrm{cr}}^{\mathrm{g}} S_{\mathrm{m}}\big(\langle T \rangle, p(\langle T \rangle)\big)$, were calculated as:

$$\Delta_{\mathrm{cr}}^{\mathrm{g}} S_{\mathrm{m}}\big(\langle T \rangle, p(\langle T \rangle)\big) = \Delta_{\mathrm{cr}}^{\mathrm{g}} H_{\mathrm{m}}(\langle T \rangle)/\langle T \rangle \tag{2.49}$$

Sublimation enthalpies are reported in the standard state (10^5 Pa, T). The measured enthalpy at the vapor pressure of the substance, $\Delta_{cr}^{g} H_m(\langle T \rangle)$, differs slightly from the standard value, $\Delta_{cr}^{g} H_m^{\circ}(\langle T \rangle)$, by two correction terms. For most organic compounds, these corrections are negligible at 298.15 K, so that:

$$\Delta_{cr}^{g} H_m(\langle T \rangle) \approx \Delta_{cr}^{g} H_m^{\circ}(\langle T \rangle) \tag{2.50}$$

- **Correction to Standard Temperature (298.15 K)**

To allow direct comparison across compounds, the sublimation enthalpies obtained at the mean experimental temperature $\langle T \rangle$ were corrected to the reference temperature of 298.15 K using Kirchhoff's relation:

$$\Delta_{\mathrm{cr}}^{\mathrm{g}} H_{\mathrm{m}}^{\circ}(298.15\mathrm{K}) = \Delta_{\mathrm{cr}}^{\mathrm{g}} H_{\mathrm{m}}^{\circ}(\langle T \rangle) + \int_{\langle T \rangle}^{298.15} \left[C_{\mathrm{p,m}}^{\circ}(\mathrm{g}) - C_{\mathrm{p,m}}^{\circ}(\mathrm{cr})\right] \mathrm{d}T \tag{2.51}$$

The corresponding standard molar entropy and Gibbs energy of sublimation at 298.15 K were derived from:

$$\Delta_{\mathrm{cr}}^{\mathrm{g}} S_{\mathrm{m}}^{\circ}(298.15\mathrm{K}) = \Delta_{\mathrm{cr}}^{\mathrm{g}} S_{\mathrm{m}}^{\circ}(\langle T\rangle, p\langle T\rangle) + R\ln\left[\frac{p(\langle T\rangle)}{p^{\circ}}\right] + \int_{\langle T\rangle}^{298.15}\left[C_{\mathrm{p,m}}^{\circ}(\mathrm{g}) - C_{\mathrm{p,m}}^{\circ}(\mathrm{cr})\right]\frac{\mathrm{d}T}{T} \quad (2.52)$$

$$\Delta_{\mathrm{cr}}^{\mathrm{g}} G_{\mathrm{m}}^{\circ}(298.15\mathrm{K})/\ \mathrm{kJ{\cdot}mol^{-1}} = \Delta_{\mathrm{cr}}^{\mathrm{g}} H_{\mathrm{m}}^{\circ}(298.15\mathrm{K}) - 298.15 \cdot \Delta_{\mathrm{cr}}^{\mathrm{g}} S_{\mathrm{m}}^{\circ}(298.15\mathrm{K}) \quad (2.53)$$

These relations provide a consistent framework for deriving the standard thermodynamic functions of sublimation at the reference temperature. The thermochemical cycle depicted in Figure 2.8 illustrates the correction procedure, where sublimation enthalpies obtained at the mean experimental temperature $\langle T\rangle$ are adjusted to 298.15 K by considering the heat capacities of the crystalline and gaseous phases.

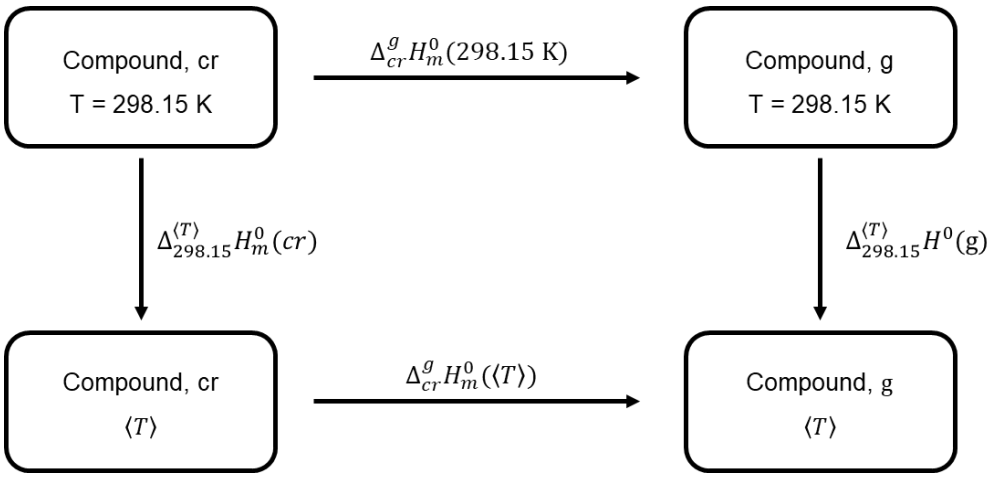

Figure 2.8. Thermochemical cycle used for correcting sublimation enthalpies from the mean experimental temperature $\langle T\rangle$ to the reference temperature of 298.15 K.

2.3. Theoretical Methodology for Gas-Phase Thermochemistry

Computational chemistry provides a valuable complement to experimental thermochemical measurements, particularly when compounds are highly toxic, unstable, expensive, or available only in very small amounts. In such cases, theoretical methods allow reliable estimations of standard molar enthalpies of formation and enthalpies of reaction, including hydrogenation processes, thereby extending the range of accessible data and enabling cross-validation of experimental results.

- **Composite Methods in Thermochemistry**

The direct solution of the Schrödinger equation for many-electron systems is computationally prohibitive, even for relatively small molecules. To overcome this, approximate quantum-chemical methods have been developed, with density functional theory (DFT) and wavefunction-based approaches as the most widely applied. Composite methods, such as the Gaussian-n (Gn) family proposed by Pople and co-workers, combine several levels of theory and basis sets in a systematic manner to improve accuracy while keeping computational costs manageable.

The first composite procedure, G1 [80], was introduced in 1989, followed by improved formulations G2 [81], G3 [82], and G4 [83]. Among these, the G3(MP2)//B3LYP [84] method has been extensively applied in molecular thermochemistry of organic compounds, including previous studies in the Thermochemistry Group at the University of Porto. This method achieves a balance between accuracy and computational efficiency, offering mean deviations typically within chemical accuracy (±4 $kJ \cdot mol^{-1}$) for standard enthalpies of formation.

Recently, Harb et al. [85] introduced the QM9-LOHC dataset, comprising over 10 373 (de)hydrogenation reactions with enthalpies computed at the G4MP2 composite level—a further example of how high-accuracy computational methods can expand experimentally inaccessible thermochemical data.

- **G3(MP2)//B3LYP Procedure**

In the G3(MP2)//B3LYP approach, molecular geometries are optimized at the B3LYP/6-31G(d) level, and harmonic vibrational frequencies are computed to confirm the nature of stationary points and to obtain zero-point vibrational energy (*ZPVE*) corrections, scaled by an empirical factor (0.9613) to compensate for anharmonicity. Subsequent single-point energy calculations are carried out at higher levels of theory, including QCISD(T)/6-31G(d) and MP2 with extended basis sets (G3MP2Large), with additional corrections for spin–orbit coupling and higher-level contributions. The final energy at 0 K is then obtained by combining these contributions, and thermal corrections to 298.15 K are introduced from partition functions of translational, rotational, and vibrational motions.

The sequential workflow of this composite method is summarized in Figure 2.8, which illustrates the combination of optimized geometries and scaled vibrational

frequencies with higher-level single-point electronic energies, ultimately leading to enthalpy values through statistical mechanics corrections.

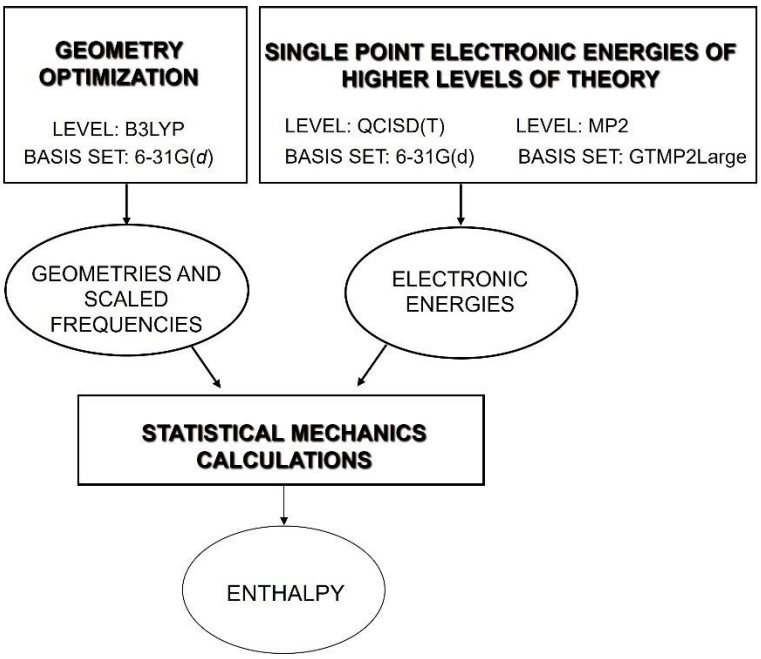

Figure 2.8 Scheme of sequential steps in G3(MP2)//B3LYP calculation.

- **Application to Hydrogenation Enthalpies**

The enthalpy of hydrogenation is defined as the enthalpy change for the addition of hydrogen to an unsaturated molecule. A general reaction can be expressed as:

$$-\mathrm{C}=\mathrm{C}-+\mathrm{H}_2 \rightarrow -\mathrm{C}-\mathrm{C}- \tag{2.54}$$

Computationally, it is obtained from the difference between the calculated enthalpies of formation of reactants and products:

$$\Delta H_{\mathrm{hyd}} = \sum H^{\circ}(\mathrm{products}) - \sum H^{\circ}(\mathrm{reactants}) \tag{2.55}$$

High-level composite methods such as G3(MP2)//B3LYP, as well as modern density functionals like M06-2X combined with complete basis set (CBS) extrapolations, have proven effective in reproducing experimental hydrogenation enthalpies with deviations within or close to chemical accuracy

For instance, Khairbek and Badawi [86] demonstrated that M06-2X/CBS-extrapolated calculations yielded mean absolute deviations as low as 2.7 $kJ \cdot mol^{-1}$ relative to experiment, validating the reliability of such methods for hydrocarbons.

- **Advantages and Limitations**

The major strength of theoretical calculations lies in their predictive capacity for compounds where experimental data are missing, hazardous, or otherwise inaccessible. Moreover, by systematically comparing computational results with experimental measurements, the accuracy of the chosen theoretical level can be validated for specific classes of molecules. Nonetheless, care must be taken when dealing with large systems or species with strong electron correlation, where the computational effort may become prohibitive or require further methodological refinement.

In this work, the G3(MP2)//B3LYP method was selected for the calculation of gas-phase enthalpies of formation of the investigated compounds, providing a reliable framework for the subsequent determination of hydrogenation enthalpies.

3. Results and Discussion

This chapter presents the experimental and computational results obtained for the compounds investigated in the scope of this dissertation. For clarity, the results are organized in two stages. First, the thermophysical properties of each dibenzoazepine derivative are presented individually - iminostilbene (IMB), iminodibenzyl (IDB), and 5-acetyliminodibenzyl (AcIDB) - covering purification, phase behaviour, calorimetric studies, and vapor pressure determinations. In the second stage, the thermochemical properties are discussed in a comparative manner, integrating experimental and computational data to derive standard molar enthalpies of formation and hydrogenation enthalpies.

As described in the Introduction, the initial project aimed to study brominated *N*-phenylcarbazoles; however, due to the impossibility of purifying these carbazole derivatives in sufficient amount and purity, it was not feasible to carry out the planned experimental program. To preserve the scientific objectives of evaluating thermochemical properties of nitrogen-containing heterocycles, the study was redirected to structurally related dibenzoazepines, which provide valuable insights into energetic stability, phase behaviour, and potential as organic hydrogen carriers.

3.1. Thermophysical Studies

3.1.1 Iminostilbene (IMB)

Iminostilbene (11*H*-benzo[b][1]benzazepine, CAS 256-96-2) was selected as one of the target compounds in this study. It is a tricyclic heteroaromatic system containing a nitrogen atom in the central seven-membered ring, structurally related to carbazole derivatives. The main properties and general characteristics of the compound are summarized in Table 3.1.

- **Purification and Purity Control**

The commercial material, received with a certified purity of 0.994 (mass fraction), was subjected to a single sublimation under reduced pressure, performed below the melting point with gentle heating, yielding bright-orange crystalline material suitable for thermophysical studies.

Purity verification was performed by gas–liquid chromatography (GLC) using dimethyl sulfoxide (DMSO) as solvent. A baseline subtraction method was employed: DMSO was injected first to record solvent contributions, followed by the IMB/DMSO solution. The chromatogram revealed a single dominant peak corresponding to IMB, and the calculated purity after sublimation was 0.9994 (mass fraction).

Table 3.1 Properties and characteristics of Iminostilbene.

Compound	**Iminostilbene**
IUPAC name	5H-Dibenzo[b,f]azepine
Structural formula	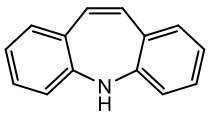
Molecular formula	$C_{14}H_{11}N$
Molar mass / g·mol^{-1}	193.24 [87]
CAS	256-96-2
Density / g·cm^{-3}	1.256 [88]
Appearance	Bright-orange powder
Source / Specification	Alfa Aesar, 99.4% (certificate of analysis, batch E3883A)

- **Thermal Analysis and Isothermal Thermogravimetry**

Differential scanning calorimetry (DSC) measurements were performed on IMB under both heating and cooling cycles for the same sample, using heating rates of 2 and 10 K·min^{-1}. These experiments confirmed the reversibility of the fusion process and the absence of additional crystal-crystal transitions within the studied temperature range. Representative DSC results are summarized in Table 3.2, while Figure 3.1 displays the DSC curves obtained at different heating rates.

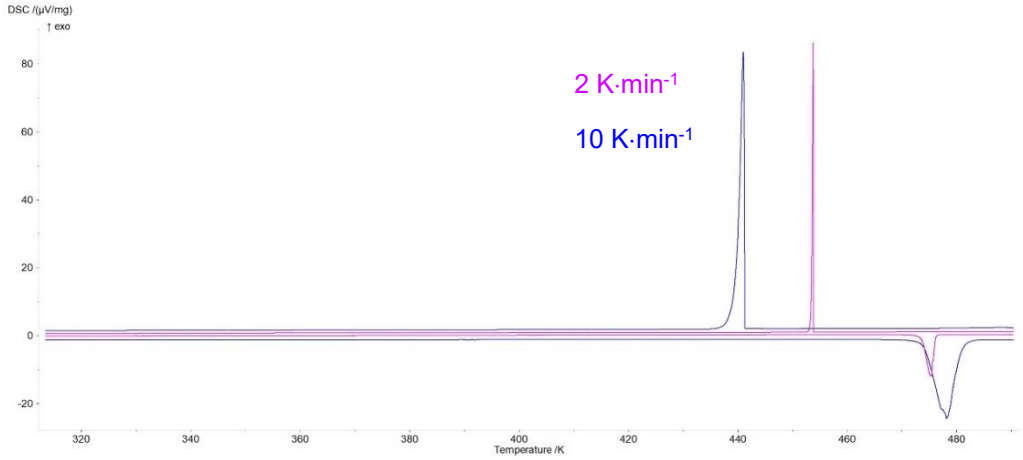

Figure 3.1 DSC heating and cooling curves of IMB recorded at 2 and 10 K·min^{-1}.

The fusion temperature of IMB was determined from five independent DSC measurements at 2 K·min^{-1}. The data show excellent reproducibility, with an average fusion temperature ⟨471.9 ± 0.9⟩ K. and an enthalpy of fusion of ⟨33.1 ± 0.4⟩ kJ·mol^{-1}. From these values, the entropy of fusion at the fusion temperature and constant pressure was calculated as $\Delta^{l}_{cr}S^{\circ}_{m}(T_{fus})$ = (70.2 ± 1.0) J·mol^{-1}·K^{-1}. The reported uncertainties correspond to the combined error, which includes the standard deviation of the mean, the calibration uncertainties of temperature and energy, respectively, and a coverage factor of 2 (95% confidence level). The narrow dispersion observed in the experimental values highlights the high stability and reliability of the fusion transition.

Table 3.2 Fusion temperature (T_{fus}) and standard molar enthalpy of fusion ($\Delta^{l}_{cr}H^{\circ}_{m}(T_{fus})$) of IMB obtained from DSC measurements at 2 K·min^{-1}.

T_{fus} / K	$\Delta^{l}_{cr}H^{\circ}_{m}(T_{fus})$ / kJ·mol^{-1}
471.87	33.30
471.95	33.12
471.96	33.45
471.94	33.05
471.91	32.61
<471.9 ± 0.9>[1]	<33.1 ± 0.4>[1]

[1]Reported uncertainties correspond to the combined error, including the standard deviation of the mean, calibration uncertainties (temperature and energy), and a coverage factor of 2 (95% confidence level).

In addition to conventional DSC measurements, IMB was further analysed by simultaneous thermogravimetric–differential scanning calorimetry (TG–DSC) under argon flow, using open aluminium crucibles with sample masses of 4-6 mg and a heating rate of 10 K·min^{-1}. The TG–DSC trace (Figure 3.2) shows that the sample remains stable in the crystalline state up to the melting event: the TG baseline is essentially flat and a sharp endotherm marks the T_{fus}. Immediately beyond this point, the DSC signal exhibits a narrow feature consistent with rapid melt–recrystallization, indicating that the liquid window is extremely small. Upon cooling, the material recrystallizes reversibly and retains its characteristics, with no evidence of degradation in this temperature range. Any subsequent mass loss occurs only at higher temperatures and is attributed to volatilization, outside the scope of the molten-phase measurements. Consequently, the overlap of melting and swift recrystallization precludes a reliable determination of thermophysical properties in the liquid state by conventional TG–DSC or non-isothermal TG protocols.

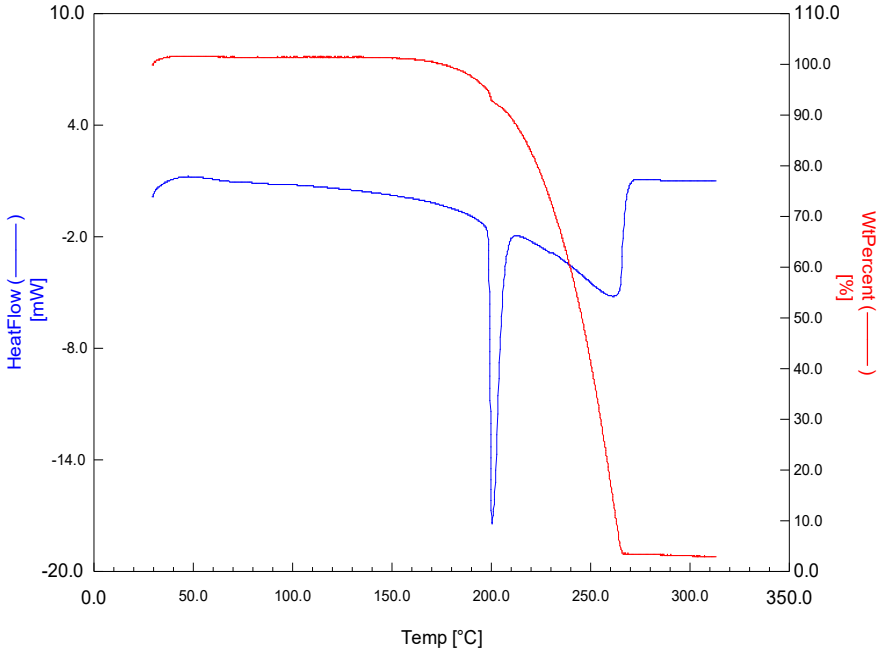

Figure 3.2 Simultaneous thermogravimetric–differential scanning calorimetry (TG–DSC) curves of IMB, obtained at a heating rate of 10 K·min^{-1}.

Exploratory TG–DSC experiments were also performed in an attempt to derive sublimation enthalpies of IMB by combining fusion and vaporization data. However, due to the immediate onset of decomposition after melting, the results proved inconsistent, yielding apparent enthalpies of vaporization in the range of 88–94 kJ·mol^{-1} at ⟨509 K⟩. These discrepancies confirm that under the applied conditions it was not possible to

separate fusion and vaporization events, precluding the reliable determination of sublimation enthalpies for IMB by this method.

- **Vapor Pressure Studies: KEML and KEMS Approaches**

Knudsen effusion experiments were performed at KEML-FCUP for IMB in the temperature range [355.17-375.15] K, yielding vapor pressures from approximately 0.11 to 0.89 Pa (Table 3.3). The results are illustrated in Figure 3.3, which shows the dependence of ln(p/Pa) on 1/T obtained with small (blue), medium (green), and large (red) orifices. The straight lines correspond to the linear fit of the Clausius–Clapeyron equation. Figure 3.4 presents the superposition of the data from the three orifice sizes, demonstrating excellent agreement and confirming that dynamic equilibrium conditions inside the effusion cell were maintained independently of the orifice size. For this reason, all the vapor pressure values were considered in the calculation of the thermodynamic sublimation parameters.

Table 3.3 Knudsen effusion mass-loss experimental results for iminostilbene (IMB), obtained at FCUP.[1]

T / K [2]	t / s	Orifices [3]	m / mg [4]			p / Pa [5]		
			m_S	m_M	m_L	p_S	p_M	p_L
355.17	29849	S3-M6-L9	5.58	8.91	12.48	0.1170	0.1183	0.1157
357.13	29849	S2-M5-L8	7.17	11.28	15.42	0.1489	0.1518	0.1441
359.10	29849	S1-M4-L7	8.49	13.29	18.79	0.1792	0.1816	0.1803
361.16	21609	S3-M6-L9	7.91	11.84	16.61	0.2311	0.2189	0.2146
363.15	21609	S2-M5-L8	9.54	14.87	20.40	0.2760	0.2787	0.2656
365.12	21609	S1-M4-L7	11.17	17.55	24.84	0.3283	0.3340	0.3320
367.16	13563	S3-M6-L9	8.76	13.31	18.60	0.4111	0.3954	0.3860
369.12	13563	S2-M5-L8	10.53	16.61	22.73	0.4894	0.5001	0.4754
371.10	13563	S1-M4-L7	—	19.46	27.57	—	0.5949	0.5920
371.15	7866	S3-M6-L9	7.59	—	16.09	0.6175	—	0.5789
373.17	7866	S2-M5-L8	9.04	14.47	19.90	0.7283	0.7554	0.7215
375.13	7866	S1-M4-L7	10.92	16.90	24.11	0.8937	0.8957	0.8974

[1]The subscripts S, M, L of the variables m (mass effused) and p (vapor pressure) correspond to the results obtained through the small (S1, S2, and S3), the medium (M4, M5, and M6) and the large (L7, L8, and L9) effusion orifices, respectively;

[2]The standard uncertainty of the measured temperature is $\pm (1 \cdot 10^{-2})$ K;

[3]The values areas, A_0, and transmission probability Clausing factors, ω_0, for each effusion orifice are given in Table A1 of appendix.

[4]The standard uncertainty is $\pm (1 \cdot 10^{-2})$ mg according to manufacturer's specifications (Analytical Balance Mettler Toledo EA 163);

[5]The standard uncertainty is $\pm (3 \cdot 10^{-2})$ Pa.

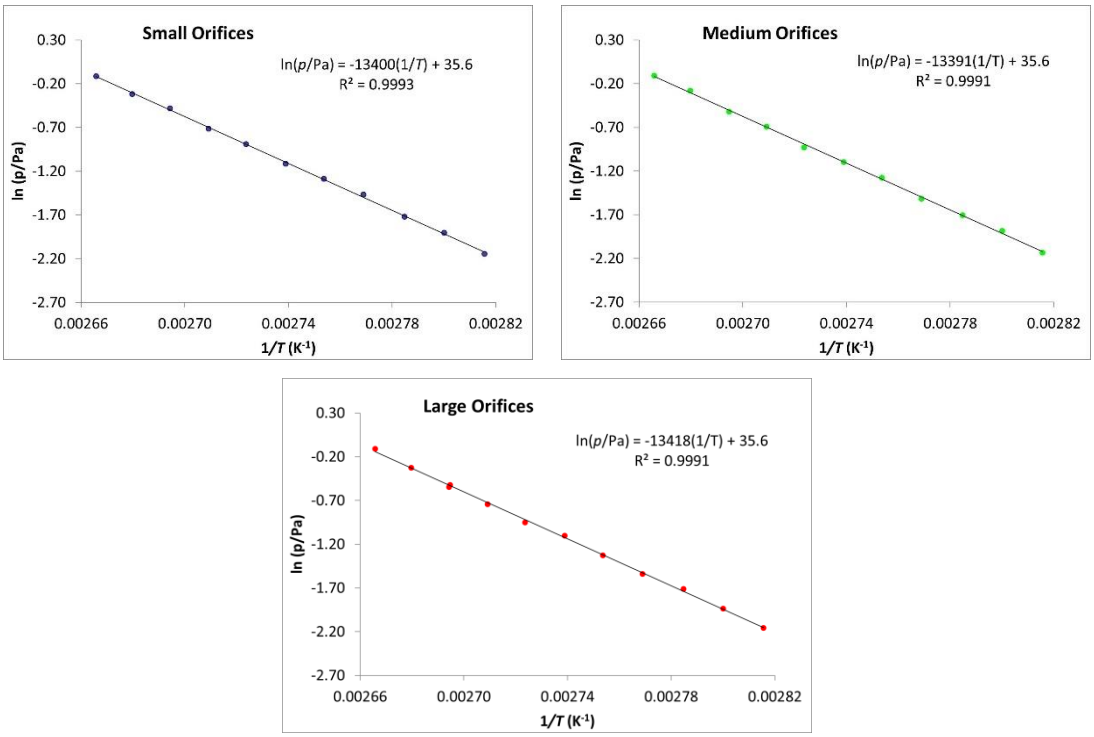

Figure 3.3 Dependence of ln(p/Pa) on 1/T for IMB, obtained by the Knudsen effusion method using the KEML-FCUP system with small (blue), medium (green), and large (red) orifices. The lines correspond to the linear fit of the Clausius–Clapeyron equation.

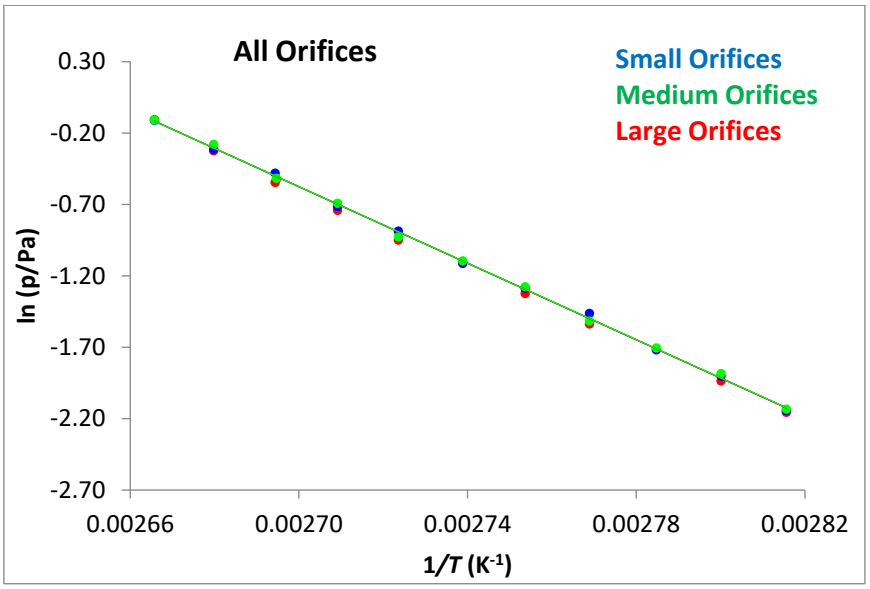

Figure 3.4 Dependence of ln(p/Pa) on 1/T for IMB obtained by the Knudsen effusion method using the KEML-FCUP system. The experimental data from small (blue), medium (green), and large (red) orifices are superimposed.

Table 3.4 summarizes the experimental data obtained for IMB by the Knudsen effusion method using the KEML-SURome system. Three independent experimental sets (Essays 1–3) were performed over different temperature intervals: Essay 1 (345.40–356.98 K), Essay 2 (339.44–358.98 K), and Essay 3 (350.84–364.57 K). For each measurement, the average temperature, effusion time, sample mass loss, and the corresponding vapor pressure were determined. These data are presented in Figure 3.5, which illustrates the dependence of ln(p/Pa) on 1/T for the three experimental sets.

Table 3.4 Knudsen effusion mass loss (SURome) experimental results for IMB.

T / K	Δt / s	Δm / mg	p_L
Essay 1			
345.40 ± 0.08	4550	0.254 ± 0.006	0.0486 ± 0.0028
347.34 ± 0.14	4337	0.307 ± 0.006	0.0617 ± 0.0033
349.21 ± 0.07	4659	0.443 ± 0.006	0.0831 ± 0.0041
351.26 ± 0.09	4241	0.523 ± 0.006	0.1080 ± 0.0052
353.15 ± 0.06	4953	0.799 ± 0.005	0.1417 ± 0.0065
355.12 ± 0.06	2606	0.558 ± 0.007	0.1886 ± 0.0093
356.98 ± 0.07	2979	0.856 ± 0.009	0.2538 ± 0.0120
Essay 2			
339.44 ± 0.04	21754	0.564 ± 0.003	0.0223 ± 0.0011
341.39 ± 0.05	16601	0.510 ± 0.003	0.0266 ± 0.0013
343.33 ± 0.12	10921	0.480 ± 0.004	0.0381 ± 0.0018
345.35 ± 0.15	7475	0.408 ± 0.005	0.0474 ± 0.0024
347.31 ± 0.09	7717	0.524 ± 0.005	0.0591 ± 0.0029
349.21± 0.17	4336	0.354 ± 0.007	0.0712 ± 0.0038
351.33 ± 0.36	4158	0.470 ± 0.008	0.0991 ± 0.0051
353.25 ± 0.20	4660	0.640 ± 0.009	0.1207 ± 0.0060
355.12 ± 0.11	4965	0.805 ± 0.005	0.1428 ± 0.0065
357.07 ± 0.10	4977	1.047 ± 0.004	0.1858 ± 0.0081
358.98 ± 0.18	4029	1.020 ± 1.590	0.2243 ± 0.1975
Essay 3			
350.84 ± 0.25	7737	0.781 ± 0.005	0.0884 ± 0.0041
352.86 ± 0.34	4565	0.605 ± 0.006	0.1165 ± 0.0056
354.84 ± 0.22	4840	0.797 ± 0.007	0.1450 ± 0.0068
356.87 ± 0.21	4889	0.992 ± 0.007	0.1792 ± 0.0082
358.77 ± 0.37	4646	1.162 ± 0.007	0.2215 ± 0.0100
360.72 ± 0.42	4695	1.376 ± 0.010	0.2603 ± 0.0118
360.67 ± 0.28	3673	1.094 ± 0.152	0.2646 ± 0.0307
362.62 ± 0.12	5033	1.783 ± 0.006	0.3154 ± 0.0135
364.57 ± 0.43	4484	1.980 ± 0.007	0.3942 ± 0.0170

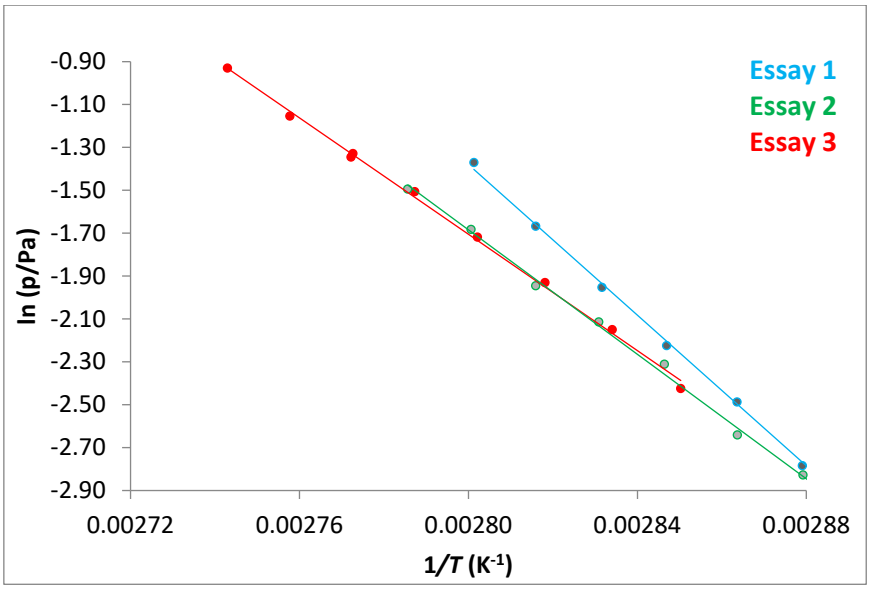

Figure 3.5 Dependence of ln(p/Pa) on 1/T for IMB obtained by the Knudsen effusion method using the KEML-SURome system.

The results display distinct slopes, with Essay 3 providing the most consistent trend, while Essays 1 and 2 exhibit significant deviations in both slope and scatter. These differences indicate that experimental conditions were not fully stabilized during the initial measurements.

A comparison between the KEML results obtained at SURome and at FCUP reveals that only the third experimental set performed in SURome showed good agreement with the FCUP data. This discrepancy may be attributed to differences in sample preparation and stabilization. In the FCUP multichannel apparatus, the solid samples are mechanically pressed into the effusion cells, producing a compact pellet with a flat surface that ensures both efficient thermal contact and reproducible effusion conditions. In contrast, at SURome the sample was introduced without pressing, which may lead to irregular surfaces, microvoids, or partial porosity, conditions that can distort the effusion regime and result in higher scatter in the early measurements. Furthermore, the first experimental runs in SURome likely involved surface stabilization phenomena, such as the removal of trace impurities or restructuring of the crystalline surface, which would affect the initial rates of mass loss. With successive heating cycles, the sample surface becomes cleaner and more homogeneous, reducing such artefacts and yielding results consistent with those obtained in FCUP. This suggests that the FCUP methodology, by enforcing initial compaction of the sample, accelerates the attainment of stable effusion conditions, while in the SURome setup such stabilization occurs gradually through repeated measurements.

For IMB, two experimental sets were obtained using KEMS, and the corresponding results are reported in Table 3.5. The dependence of ln(p/Pa) on 1/T for both sets is shown in Figure 3.6. The first experimental set exhibits a relatively high scatter in the data points, whereas the second set is more consistent, yielding a clearer linear dependence. This observation suggests that stabilization phenomena, such as surface restructuring or removal of trace impurities, may have influenced the early measurements.

It is worth noting that KEMS inherently presents certain limitations: the acquisition of a large number of experimental points is constrained by the long stabilization times required, and interruptions between measurements within a single experimental run are not possible. Nevertheless, when carefully performed, the technique provides valuable complementary information to Knudsen effusion experiments with gravimetric detection, as it also provides direct insight into the gas-phase species. In the case of IMB, the expected behaviour was the detection of the molecular ion, accompanied by characteristic fragmentation products consistent with its aromatic structure. This was indeed observed, with the spectra showing the presence of the molecular ion together with the expected fragment ions, in agreement with the known gas-phase chemistry of IMB.

Table 3.5 Knudsen effusion mass spectrometry (KEMS) experimental results for IMB

T / K	Ticks	Scale	I^+	p / Pa
		Essay 1		
311.9	6.5	0.1	0.7386	2.304×10^{-4}
317.8	8.0	0.3	2.7273	8.667×10^{-4}
322.3	13.0	0.3	4.4318	1.4284×10^{-3}
328.0	7.5	1.0	8.5227	2.795×10^{-3}
335.2	14.5	1.0	16.4773	5.523×10^{-3}
		Essay 2		
315.7	12.5	0.1	1.4205	4.484×10^{-4}
320.3	7.5	0.3	2.5568	8.189×10^{-4}
326.7	16	0.3	5.4545	1.782×10^{-3}
334.3	12.5	1.0	14.2045	4.749×10^{-4}

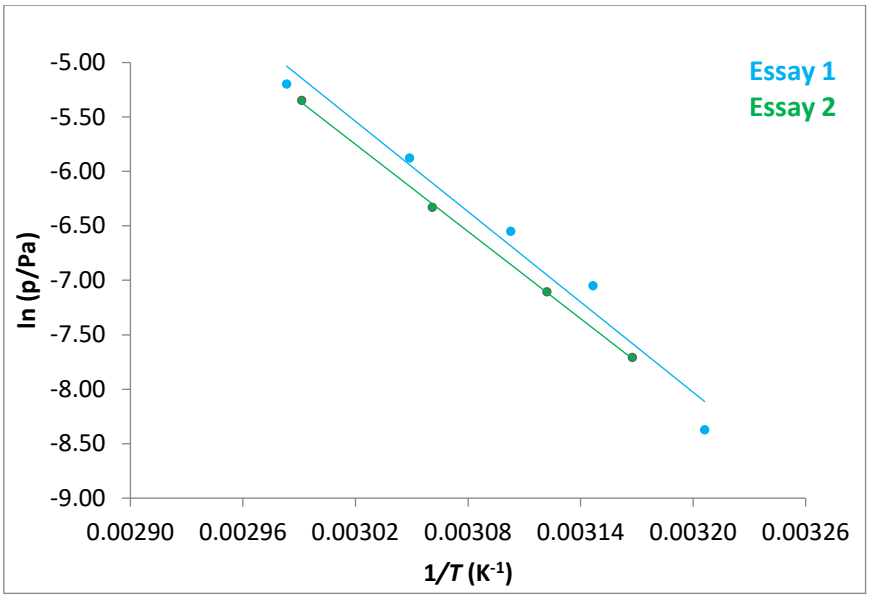

Figure 3.6 Dependence of ln(p/Pa) on 1/T for IMB obtained by KEMS. The results correspond to two experimental sets: Essay 1 (blue) and Essay 2 (green).

For IMB, no reliable QCM results could be obtained. The compound proved to be too volatile, and under the open-cell operating mode it was not possible to control the sublimation process. The QCM setup was specifically designed for the study of ionic liquids and other low-volatility substances; therefore, it is not suitable for volatile compounds such as IMB.

The sublimation parameters of IMB obtained by the three techniques are summarized in Table 3.6, with the corresponding vapor pressure data represented in Figures 3.7 and 3.8. The results from KEML-FCUP and KEML-SURome are in very good agreement, confirming the reproducibility of the gravimetric Knudsen effusion method across different laboratories. Small variations in the derived enthalpies can be attributed to differences in sample preparation and the specific effusion cell geometries employed. The KEMS experiments, although restricted to a narrower temperature range and exhibiting larger scatter, yielded consistent results of the same order of magnitude and provided complementary information by confirming the gas-phase identity of IMB, with spectra showing only the molecular ion and characteristic fragments, thereby excluding the presence of dimers.

Table 3.6 Thermodynamic parameters of sublimation of IMB derived from vapor pressure measurements obtained by Knudsen effusion at KEML–FCUP and KEML–SURome, and by Knudsen effusion mass spectrometry (KEMS). Parameters *a* and *b* correspond to the intercept and slope of the Clausius–Clapeyron equation.

Set/ Essay	***a***	***b***	$p(\langle T \rangle)$ **/ Pa**	$\Delta_{cr}^{g} H_m(\langle T \rangle)$ **/ kJ·mol^{-1}**	$\Delta_{cr}^{g} S_m(\langle T \rangle, p\langle T \rangle)$**/ J·K^{-1}·mol^{-1}**
KEML - FCUP					
Small Orifices	35.6 ± 0.7 [1]	13400 ± 258 [1]	0.334 <365.15K>	111.4 ± 2.1 [7]	305.1 ± 5.8 [7]
Medium Orifices	35.6 ± 0.8 [1]	13391 ± 302 [1]	0.342 <365.15K>	111.3 ± 2.5 [7]	304.8 ± 6.8 [7]
Large orifices	35.6 ± 0.8 [2]	13418 ± 289 [2]	0.318 <365.15K>	111.6 ± 2.4 [7]	305.6 ± 6.6 [7]
All Orifices	35.6 ± 0.5 [3]	13393 ± 170 [3]	0.340 <365.15K>	111.4 ± 1.4 [7]	305.1 ± 3.8 [7]
KEML-SURome					
Essay 1	47.8 ± 2.1 [4]	17556 ± 754 [4]	0.112 <351.19>	146.0 ± 6.3 [7]	416 ± 18 [7]
Essay 2	39.0 ± 1.4 [1]	14515 ± 504 [1]	0.077 <349.21>	120.7 ± 4.2 [7]	346 ± 12 [7]
Essay 3	36.3 ± 1.5 [5]	13564 ± 547 [5]	0.198 <357.71>	112.8 ± 4.5 [7]	315 ± 13 [7]
KEMS					
Essay 1	36 ± 14 [6]	13820 ± 4459 [6]	0.00148 <323.55>	115 ± 37 [7]	355 ± 114 [7]
Essay 2	34.6 ± 1.4 [6]	13367 ± 447 [6]	0.00146 <325.00>	111.1 ± 3.7 [7]	342 ± 11 [7]

The standard uncertainties were obtained by multiplying the standard error of the fitting parameters by a coverage factor k corresponding to the t-distribution value for a 0.95 confidence level and the respective degrees of freedom:
[1] k=2.26 (9 degrees of freedom); [2] k=2.23 (10 degrees of freedom); [3] k=2.04 (32 degrees of freedom); [4] k=2.57 (5 degrees of freedom); [5] k=2.36 (7 degrees of freedom); [6] k=3.18 (3 degrees of freedom);
[7] The uncertainties quoted are the combined standard uncertainties (0.95 level of confidence).

The standard thermodynamic parameters of sublimation calculated at 298.15 K are presented in Table 3.7, showing excellent consistency within the combined experimental uncertainties. The standard molar enthalpies of sublimation range from 112 to 115 kJ·mol^{-1}, while the entropies and Gibbs free energies derived from the three techniques are also in close correspondence, further supporting the robustness of the dataset and the validity of the extrapolation procedure. The slightly lower entropy obtained from KEMS can be attributed to the narrower temperature interval and the larger scatter of

the mass spectrometric data. Overall, the consistency of the thermodynamic functions derived from independent techniques and laboratories provides strong confidence in the reported sublimation parameters of IMB and highlights the complementary advantages of gravimetric and mass spectrometric Knudsen effusion approaches.

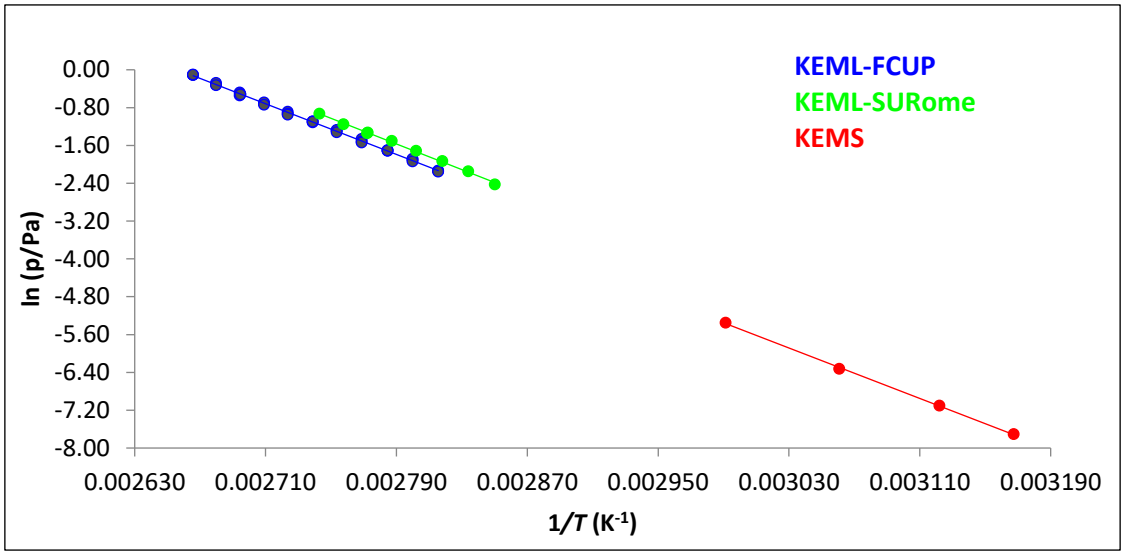

Figure 3.7 Comparison of the vapor pressure results for IMB obtained by KEML–FCUP (blue), KEML–SURome (green), and KEMS (red).

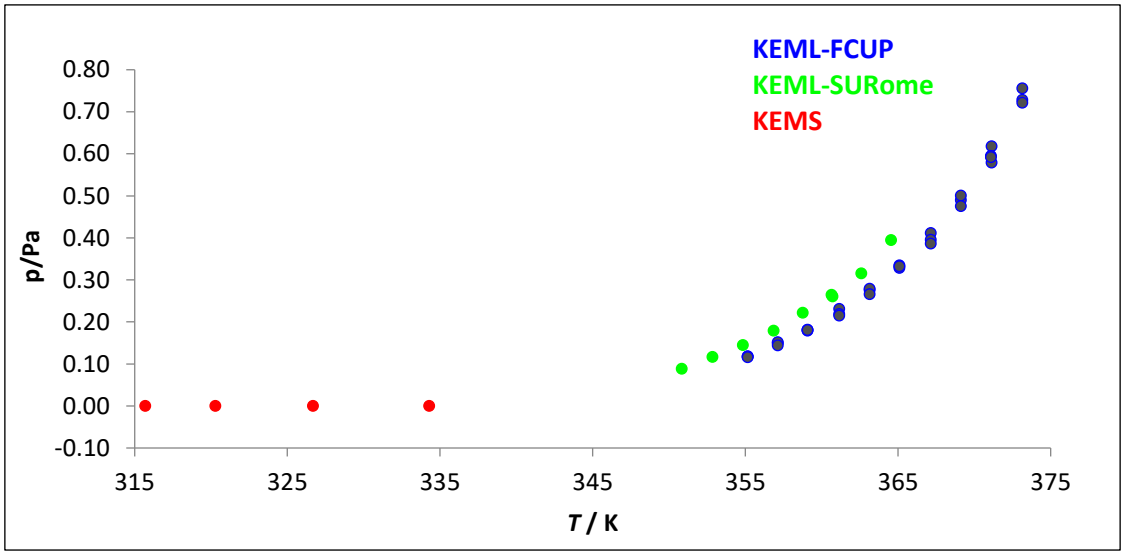

Figure 3.8 Vapor pressure of IMB as a function of temperature, obtained by KEML–FCUP (blue), KEML–SURome (green), and KEMS (red).

Table 3.7 Standard (p° = 0.1 MPa) molar enthalpies, $\Delta_{cr}^{g}H_m^\circ$, entropies, $\Delta_{cr}^{g}S_m^\circ$, and Gibbs energies, $\Delta_{cr}^{g}G_m^\circ$, of sublimation, and vapor pressure, p, at T = 298.15 K, for iminostilbene, obtained by different experimental techniques: Knudsen effusion at KEML-FCUP and KEML-SURome, and Knudsen effusion mass spectrometry (KEMS).[1]

Equipment	$\Delta_{cr}^{g}H_m^\circ$ / kJ·mol^{-1}	$\Delta_{cr}^{g}S_m^\circ$ / J·K^{-1}·mol^{-1}	$\Delta_{cr}^{g}G_m^\circ$/ kJ·mol^{-1}	p / Pa
KEML-Porto	113.9 ± 1.4	207.9 ± 3.8	51.9 ± 1.8	8.03×10^{-5}
KEML-SURome	115.0 ± 4.5	212 ± 13	51.5 ± 5.9	9.41×10^{-5}
KEMS	112.1 ± 3.7	195 ± 11	54.0 ± 5.0	3.52×10^{-5}

[1]The uncertainties quoted are the combined standard uncertainties (0.95 level of confidence).

3.1.2 Iminodibenzyl (IDB)

Iminodibenzyl (6,11-dihydro-5*H*-benzo[b][1]benzazepine, CAS 491-19-9) was selected as one of the compounds in this study. Structurally, it is closely related to iminostilbene, differing in the central seven-membered ring, where the absence of a double bond renders IDB a fully saturated analogue. The main physicochemical properties and general characteristics of IDB are summarized in Table 3.8.

Table 3.8 Properties and characteristics of iminodibenzyl.

Compound	Iminodibenzyl
IUPAC name	10,11-dihydro-5H-dibenz[b,f]azepine
Structural formula	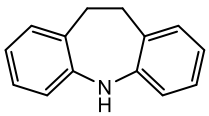
Molecular formula	$C_{14}H_{13}N$
Molar mass / g·mol^{-1}	195.2650
CAS	494-19-9
Density / g·cm^{-3}	1.1 ± 0.1[89]
Appearance	Fine, beige powder
Source / Specification	Alfa Aesar, 99.4% (certificate of analysis, batch E7426A)

- **Purification and Purity Control**

The commercial sample, supplied with a certified purity of 0.994 (mass fraction), was initially subjected to sublimation. However, the process led to a decrease in purity, as the impurity present was more volatile than the compound itself and condensed on the cold finger; after two sublimations, the purity decreased to 0.991. Consequently, recrystallization from methanol was performed, affording a material with an improved purity of 0.996. The recrystallized sample was then carefully dried to ensure complete removal of residual solvent.

Purity verification was carried out by gas–liquid chromatography (GLC), using dimethyl sulfoxide (DMSO) as solvent. A baseline subtraction procedure was applied: a blank DMSO injection was recorded first to account for solvent contributions, followed by analysis of the IDB/DMSO solution.

- **Thermal Analysis and Isothermal Thermogravimetry**

Differential scanning calorimetry (DSC) experiments were carried out for IDB, applying both heating and cooling cycles to the same specimen at rates of 2 and 10 $K \cdot min^{-1}$. The results demonstrated that the melting process is fully reversible and that no additional solid–solid phase transitions occur within the investigated temperature interval. This absence of crystal–crystal transitions prior to melting ensures that thermophysical studies by Knudsen effusion techniques can be reliably conducted over this temperature range. A summary of the DSC data is provided in Table 3.9, and the thermograms recorded at the two heating rates are presented in Figure 3.9.

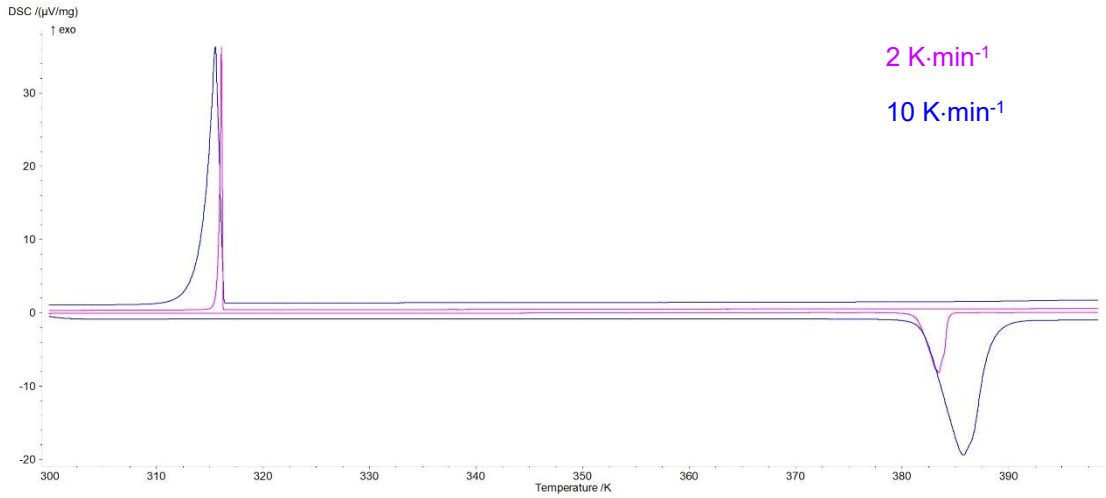

Figure 3.9 DSC heating and cooling curves of IDB recorded at 2 and 10 $K \cdot min^{-1}$.

The melting properties of IDB were investigated through five DSC runs performed at a heating rate of 2 K·min^{-1}. The measurements yielded highly consistent results, giving an average fusion temperature of ⟨380.1 ± 0.9⟩ K. and a corresponding molar enthalpy of fusion of ⟨24.1 ± 0.3⟩ kJ·mol^{-1}. From these values, the standard molar entropy of fusion at the fusion temperature and constant pressure was derived as $\Delta^{l}_{cr}S^{\circ}_{m}(T_{fus})$ = (63.7 ± 1.0) J·mol^{-1}·K^{-1}. The reported uncertainties represent combined values, accounting for the standard deviation of the mean, calibration errors in both temperature and enthalpy, and the use of a coverage factor of 2 (95% confidence level).

Table 3.9 Fusion temperature (T_{fus}) and standard molar enthalpy of fusion ($\Delta^{l}_{cr}H^{\circ}_{m}(T_{fus})$) of IDB obtained from DSC measurements at 2 K·min^{-1}.

T_{fus} / K	$\Delta^{l}_{cr}H^{\circ}_{m}(T_{fus})$ / kJ·mol^{-1}
380.17	24.26
380.12	24.11
380.25	24.13
380.10	24.24
379.91	24.16
< 380.1 ± 0.9>[1]	<24.2 ± 0.3>[1]

[1]Reported uncertainties correspond to the combined error, including the standard deviation of the mean, calibration uncertainties (temperature and energy), and a coverage factor of 2 (95% confidence level).

In addition to conventional DSC measurements, IDB was further analysed by simultaneous thermogravimetric–differential scanning calorimetry (TG–DSC) under argon flow, using open aluminium crucibles with sample masses of 4-6 mg and a heating rate of 10 K·min^{-1}. The TG–DSC curves (Figure 3.10) exhibit a sharp endothermic peak associated with melting, with no evidence of additional solid-solid transitions, as previously confirmed by the independent DSC experiments. Following fusion, a single mass-loss event is observed, attributable to vaporization rather than decomposition, as supported by the reproducibility of the DSC melting cycles. These results indicate that IDB remains chemically stable up to its volatilization range, thereby enabling reliable thermophysical investigations within this temperature interval.

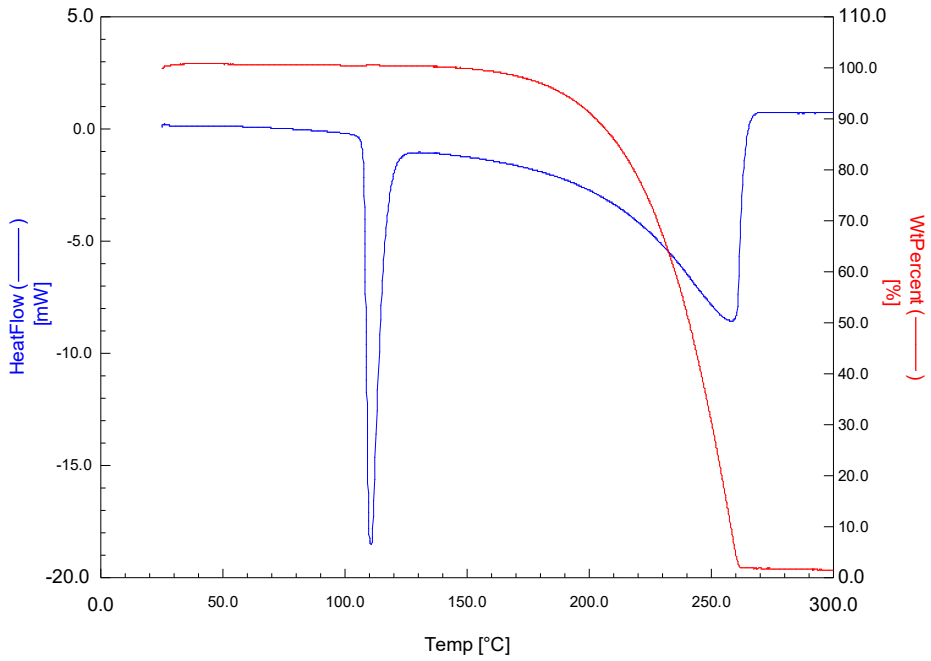

Figure 3.10 Simultaneous thermogravimetric–differential scanning calorimetry (TG–DSC) curves of IDB, obtained at a heating rate of 10 K·min^{-1}.

Isothermal thermogravimetric measurements were performed on IDB at a heating rate of 10 K·min^{-1} in order to derive the sublimation enthalpy from combined calorimetric and mass-loss data. In this approach, the fusion and vaporization processes are monitored simultaneously by TG-DSC. The enthalpy of fusion was obtained by integrating the melting peak, while the enthalpy of vaporization was determined from the mass-loss step recorded under isothermal conditions. Both contributions were corrected to the reference temperature of 298.15, thereby allowing the calculation of the standard molar enthalpy of sublimation.

The experimental results, summarized in Table 3.10, reveal an average standard sublimation enthalpy of ⟨112.5 ± 0.2⟩ kJ·mol^{-1} for IDB at 298.15 K, obtained from the combination of an enthalpy of fusion of ⟨18.2 ± 0.4⟩ kJ·mol^{-1} and an enthalpy of vaporization of ⟨94.1 ± 0.1⟩ kJ·mol^{-1}. The reproducibility of the independent determinations highlights the reliability of the method for this compound, further confirming that IDB undergoes a clean volatilization process without detectable decomposition within the studied range.

Table 3.10 Thermodynamic results for IDB obtained from isothermal thermogravimetry (TG-DSC): fusion enthalpy, vaporization enthalpy, and sublimation enthalpy corrected to 298.15 K.

$\langle T \rangle$ / K	$\Delta_{cr}^{l} H_m^{\circ}(298.15\mathrm{K})$ / kJ·mol^{-1}	$\Delta_{l}^{g} H_m^{\circ}(298.15\mathrm{K})$ / kJ·mol^{-1}	$\Delta_{cr}^{g} H_m^{\circ}(298.15K)$ / kJ·mol^{-1}
453.47	18.63	94.12	112.75
453.47	18.94	94.82	113.76
453.51	19.10	94.69	113.79
453.05	15.65	92.25	107.89
452.20	19.28	94.77	114.05
< 453.14 ± 0.03>[1]	<18.2 ± 0.4>[1]	<94.1 ± 0.1>[1]	<112.5 ± 0.2>[1]

[1]Reported uncertainties correspond to the the standard deviation of the mean.

- **Vapor Pressure Studies: KEML and KEMS Approaches**

Knudsen effusion experiments on IDB were performed at KEML–FCUP over the range [329.18-351.12] K, yielding vapor pressures of 0.07 to 0.84 Pa (Table 3.11). Figure 3.11 shows the ln(*p*/Pa) vs. 1/*T* plots for small, medium, and large orifices, together with the corresponding Clausius–Clapeyron fits. The combined data in Figure 3.12 display excellent agreement among the three orifice sizes, confirming the attainment of dynamic equilibrium within the effusion cell. All vapor pressure values were therefore used in the derivation of sublimation parameters.

Table 3. 11 Knudsen effusion mass-loss experimental results for iminodibenzyl (IDB), obtained at FCUP.[1]

T / K [2]	*t* / s	Orificies [3]	*m* / mg [4]			*p* / Pa [5]		
			m_S	m_M	m_L	p_S	p_M	p_L
329.18	46009	S3-M6-L9	7.28	9.08	11.31	0.0748	0.0755	0.0749
331.17	46009	S2-M5-L8	9.15	11.27	14.19	0.0943	0.0940	0.0942
333.11	46009	S1-M4-L7	11.47	14.14	17.80	0.1186	0.1183	0.1185
335.17	24596	S3-M6-L9	7.61	9.42	11.86	0.1477	0.1479	0.1482
337.18	24596	S2-M5-L8	9.75	11.84	14.87	0.1898	0.1864	0.1864
339.12	24596	S1-M4-L7	11.91	14.87	18.30	0.2325	0.2348	0.2300
341.17	16516	S3-M6-L9	9.97	12.37	15.38	0.2907	0.2917	0.2888
343.18	16516	S2-M5-L8	12.49	15.22	18.89	0.3652	0.3600	0.3557
345.11	16516	S1-M4-L7	15.19	18.61	23.48	0.4454	0.4414	0.4434
347.16	10183	S3-M6-L9	11.62	14.26	18.02	0.5543	0.5502	0.5535
349.18	10183	S2-M5-L8	14.39	17.61	22.07	0.6884	0.6814	0.6799
351.12	10183	S1-M4-L7	17.58	21.69	27.27	0.8433	0.8416	0.8424

[1]The subscripts S, M, L of the variables *m* (mass effused) and *p* (vapor pressure) correspond to the results obtained through the small (S1, S2, and S3), the medium (M4, M5, and M6) and the large (L7, L8, and L9) effusion orifices, respectively; [2]The standard uncertainty of the measured temperature is ± (1·10^{-2}) K;

[3]The values areas, A_0, and transmission probability Clausing factors, ω_0, for each effusion orifice are given in Table A2 of appendix. [4]The standard uncertainty is $\pm (1 \cdot 10^{-2})$ mg according to manufacturer's specifications (Analytical Balance Mettler Toledo EA 163); [5]The standard uncertainty is $\pm (3 \cdot 10^{-2})$ Pa.

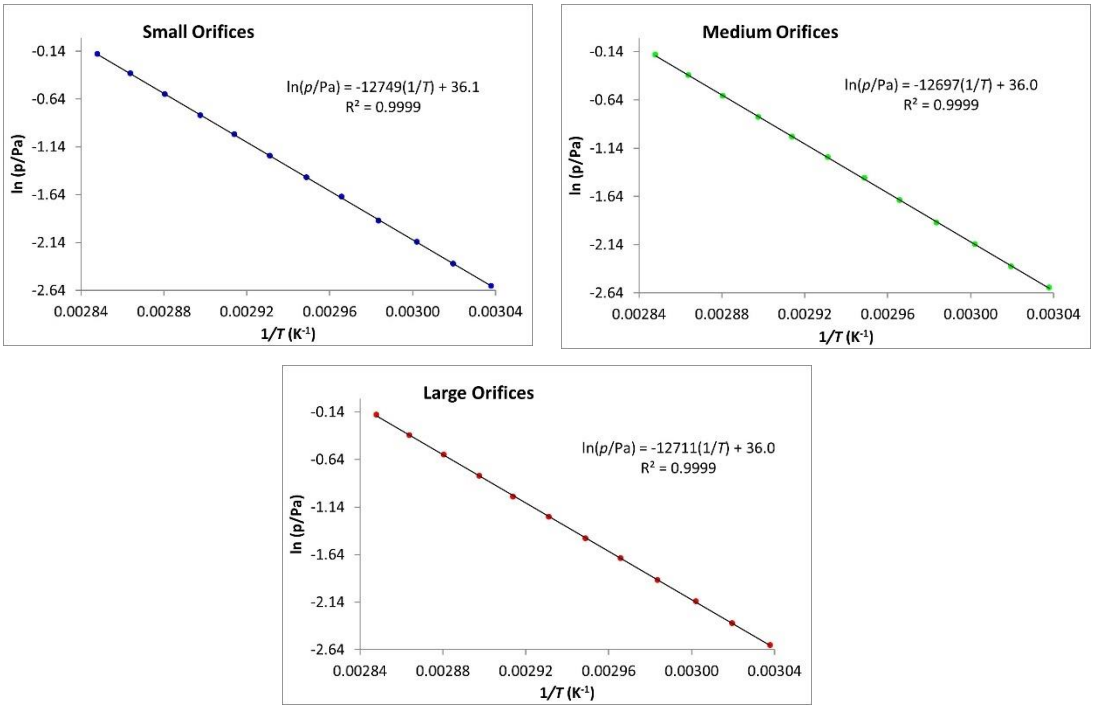

Figure 3. 11 Dependence of ln(p/Pa) on 1/T for IDB, obtained by the Knudsen effusion method using the KEML-FCUP system with small (blue), medium (green), and large (red) orifices. The lines correspond to the linear fit of the Clausius–Clapeyron equation.

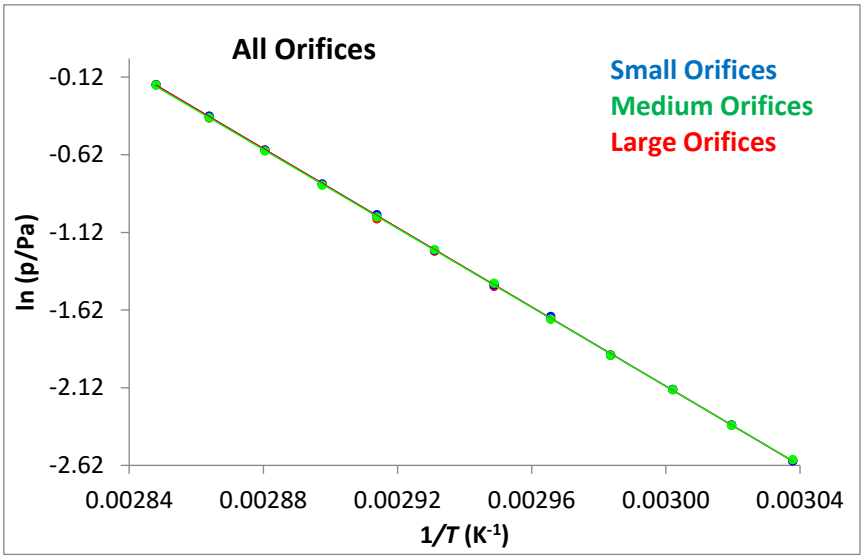

Figure 3.12 Dependence of ln(p/Pa) on 1/T for IDB obtained by the Knudsen effusion method using the KEML-FCUP system. The experimental data from small (blue), medium (green), and large (red) orifices are superimposed.

Knudsen effusion measurements with the KEML-SURome apparatus are summarized in Table 3.12, which reports the vapor pressure results for IDB. Three experimental series were conducted within partially overlapping temperature intervals: Essay 1 [332.19-352.16 K], Essay 2 [328.58-349.45 K], and Essay 3 [334-12-347.69 K]. For each run, the mean temperature, effusion time, sample mass loss, and corresponding vapor pressure were determined. Figure 3.13 shows the ln(p/Pa) versus 1/T dependence for IDB obtained in three independent Knudsen effusion experiments performed with the KEML–SURome apparatus. The results reveal marked differences among the datasets: Essay 1 exhibits a significantly different slope and higher scatter, suggesting insufficient stabilization during the early stages of the measurements. In contrast, Essays 2 and 3 show closely matching linear trends, confirming consistent vapour pressure behaviour. For the final determination of sublimation enthalpy, Essay 3 was selected, as it is considered to have benefitted from a longer stabilization period, ensuring more reliable equilibrium conditions.

Table 3.12 Knudsen effusion mass loss (SURome) experimental results for IDB.

T / K	Δt / s	Δm / mg	p_L
Essay 1			
332.19 ±0.26	13627	1.651 ± 0.004	0.1027 ± 0.0048
334.60 ± 0.32	8792	1.411 ± 0.005	0.1366 ± 0.0064
336.14 ± 0.29	8519	1.648 ± 0.006	0.1650 ± 0.0077
337.64 ± 0.73	5400	1.284 ± 0.007	0.2032 ± 0.0098
338.96 ± 0.40	6209	1.691 ± 0.007	0.2333 ± 0.0110
341.46 ± 0.24	6619	2.495 ± 0.084	0.3241 ± 0.0205
343.42 ± 0.35	4095	2.037 ± 0.007	0.4289 ± 0.0197
345.44 ± 0.27	4695	3.137 ± 0.008	0.5776 ± 0.0260
347.38 ± 0.24	4517	4.030 ± 0.008	0.7734 ± 0.0345
352.16 ± 0.23	3092	5.259 ± 0.010	1.4845 ± 0.0651
Essay 2			
328.58 ± 0.20	21938	1.663 ± 0.010	0.0639 ± 0.0032
331.33 ± 0.20	16053	1.655 ± 0.010	0.0873 ± 0.0043
332.83 ± 0.21	10135	1.224 ± 0.010	0.1025 ± 0.0051
334.54 ± 0.20	10153	1.571 ± 0.010	0.1317 ± 0.0064
336.61 ± 0.20	10023	1.952 ± 0.010	0.1662 ± 0.0079
338.73 ± 0.20	7209	1.913 ± 0.010	0.2271 ± 0.0108
341.01 ± 0.20	7161	2.476 ± 0.010	0.2971 ± 0.0138
342.87 ± 0.20	3928	1.752 ± 0.010	0.3841 ± 0.0181
344.94 ± 0.20	3702	1.960 ± 0.010	0.4575 ± 0.0213
347.18 ± 0.20	4187	2.969 ± 0.010	0.6145 ± 0.0279
349.45 ± 0.20	5513	4.588 ± 0.010	0.7237 ± 0.0321
Essay 3			
334.12 ± 0.020	7725	1.166 ± 0.010	0.1283 ± 0.0064
336.35 ± 0.020	5916	1.182 ± 0.010	0.1704 ± 0.0085
338.25 ± 0.020	7321	1.760 ± 0.010	0.2056 ± 0.0098
340.15 ± 0.020	7646	2.271 ± 0.010	0.2548 ± 0.0119
342.06 ± 0.020	4590	1.738 ± 0.010	0.3257 ± 0.0154
344.08 ± 0.020	4510	2.154 ± 0.010	0.4121 ± 0.0191
345.77 ± 0.020	5997	3.277 ± 0.010	0.4727 ± 0.0214
347.69 ± 0.020	4897	3.330 ± 0.010	0.5898 ± 0.0266

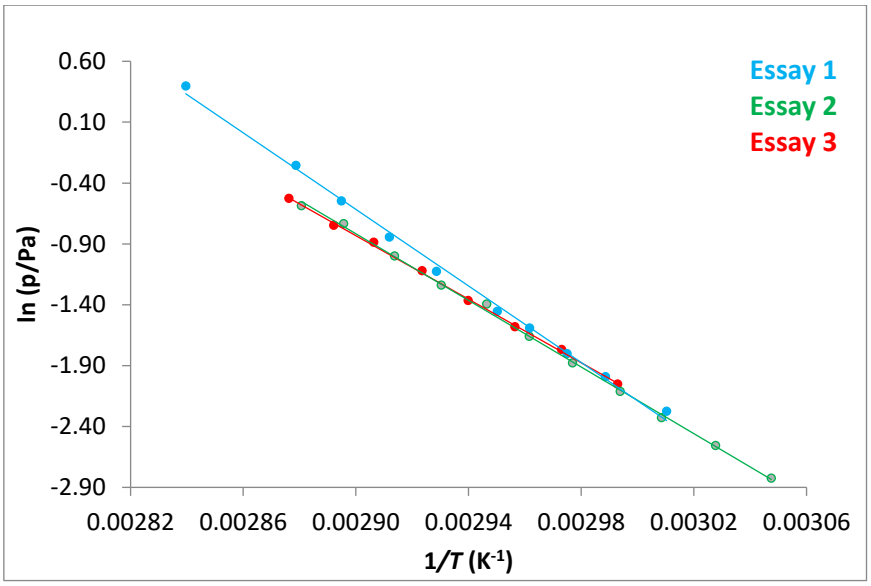

Figure 3.13 Dependence of ln(p/Pa) on 1/T for IDB obtained by the Knudsen effusion method using the KEML-SURome system.

Knudsen effusion mass spectrometry (KEMS) experiments were carried out for IDB, and the corresponding results are summarized in Table 3.13. Two independent experimental sets were performed, covering the temperature ranges 307.3-329.0 K (Essay 1) and 312.1-328.5 K (Essay 2). For each measurement, the ion beam intensity was recorded and converted into vapor pressure values using the instrumental calibration constant.

Table 3.13 Knudsen effusion mass spectrometry (KEMS) experimental results for IDB.

T / K	Ticks	Scale	I^+	p / Pa
		Essay 1		
307.30	5.5	1.0	6.2502	0.0142
315.80	17.0	1.0	19.3188	0.0451
321.70	15.5	3.0	52.8426	0.1258
329.00	11.5	10.0	130.6860	0.3181
		Essay 2		
312.1	4.00	3.0	13.6368	0.0315
317.3	8.5	3.0	28.9782	0.0680
322.4	17.0	3.0	57.9564	0.1382
328.5	10.0	10.0	113.6400	0.2762

The plots of ln(p/Pa) versus 1/T for the two datasets are presented in Figure 3.14. Both experimental series exhibit a clear linear dependence consistent with the Clausius–Clapeyron relation, although Essay 2 displays slightly reduced scatter compared to

Essay 1. This indicates a more stable effusion regime in the second run, likely due to improved surface equilibration of the sample after initial heating cycles. Despite the limited number of experimental points inherent to the technique, the results provide complementary evidence for the sublimation behavior of IDB in the studied temperature interval.

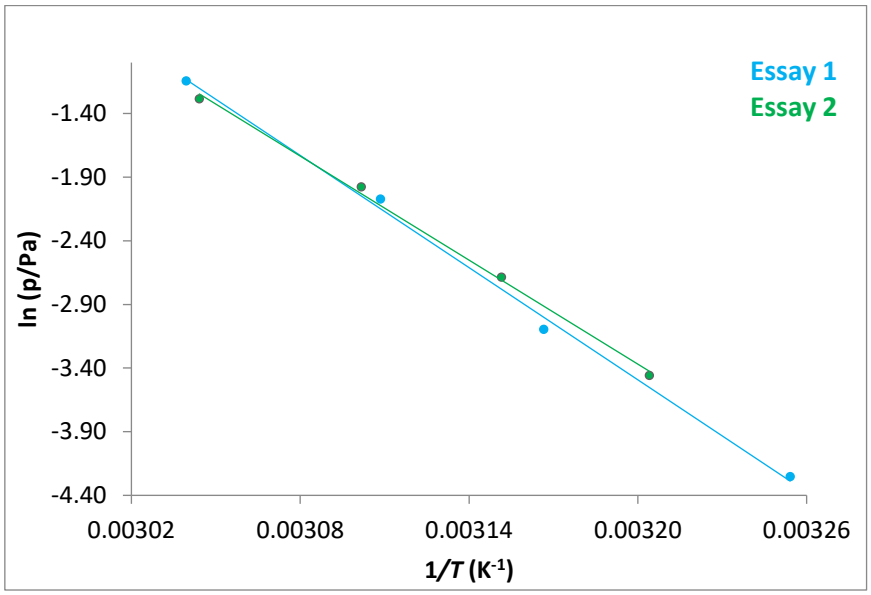

Figure 3.14 Dependence of ln(p/Pa) on 1/T for IDB obtained by KEMS. The results correspond to two experimental sets: Essay 1 (blue) and Essay 2 (green).

The sublimation parameters of IDB derived from the different Knudsen effusion experiments reveal noticeable variations in the Clausius–Clapeyron slopes, particularly between the KEML–FCUP and KEML–SURome datasets. The Porto results yield a consistent sublimation enthalpy at mean temperature of experiments of about 106 kJ·mol^{-1}, whereas the Rome measurements, especially Essay 1, initially suggest significantly higher values. However, the later series (Essay 3) converge toward the FCUP data, indicating that stabilization effects and experimental conditions strongly influenced the earlier results. The KEMS measurements, although characterized by larger scatter and higher uncertainties, provide intermediate values that fall within the experimental error limits of the gravimetric determinations. When corrected to 298.15 K (Table 3.15), the three techniques give sublimation enthalpies in the range of 107–114 kJ·mol^{-1}, demonstrating overall consistency and reinforcing the reliability of the reported thermodynamic parameters.

Table 3.14 Thermodynamic parameters of sublimation of IDB derived from vapor pressure measurements obtained by Knudsen effusion at KEML–FCUP and KEML–SURome, and by Knudsen effusion mass spectrometry (KEMS). Parameters *a* and *b* correspond to the intercept and slope of the Clausius–Clapeyron equation.

Set/ Essay	*a*	*b*	$p(\langle T \rangle)$ / Pa	$\Delta^{g}_{cr}H_m(\langle T \rangle)$ / kJ·mol^{-1}	$\Delta^{g}_{cr}S_m(\langle T \rangle, p\langle T \rangle)$/ J·K^{-1}·mol^{-1}
KEML - FCUP					
Small Orifices	36.1 ± 0.2 [1]	12749 ± 67 [1]	0.251 <340.15K>	106.0 ± 0.6 [7]	311.6 ± 1.8 [7]
Medium Orifices	36.0 ± 0.2 [1]	12697 ± 78 [1]	0.265 <340.15K>	105.6 ± 0.6 [7]	310.5 ± 1.8 [7]
Large orifices	36.0 ± 0.2 [1]	12711 ± 72 [1]	0.254 <340.15K>	105.7 ± 0.6 [7]	310.7 ± 1.8 [7]
All Orifices	35.6 ± 0.5 [2]	12719 ± 40 [2]	0.248 <340.15K>	105.8 ± 0.3 [7]	311.0 ± 0.9 [7]
KEML-SURome					
Essay 1	45.0 ± 2.0 [3]	15721 ± 698 [3]	0.389 <342.18>	130.7 ± 5.8 [7]	382 ± 17 [7]
Essay 2	38.9 ± 1.0 [4]	13682 ± 350 [4]	0.233 <339.02>	113.8 ± 2.9 [7]	335.7 ± 8.5 [7]
Essay 3	37.0 ± 1.3 [5]	13044 ± 445 [5]	0.283 <340.91>	108.5 ± 3.7 [7]	318 ± 11 [7]
KEMS					
Essay 1	43.5 ± 7.7 [6]	14689 ± 2462 [6]	0.0692 <318.15>	122 ± 21 [7]	383.5 ± 66 [7]
Essay 2	40.2 ± 6.2 [6]	13619 ± 1975 [6]	0.0983 <320.30>	113 ± 16 [7]	353 ± 50 [7]

The standard uncertainties were obtained by multiplying the standard error of the fitting parameters by a coverage factor k corresponding to the t-distribution value for a 0.95 confidence level and the respective degrees of freedom:
[1] k=2.23 (10 degrees of freedom); [2] k=2.03 (34 degrees of freedom); [3] k=2.31 (8 degrees of freedom); [4] k=2.26 (9 degrees of freedom); [5] k=2.45 (6 degrees of freedom); [6] k=4.30 (2 degrees of freedom);
[7] The uncertainties quoted are the combined standard uncertainties (0.95 level of confidence).

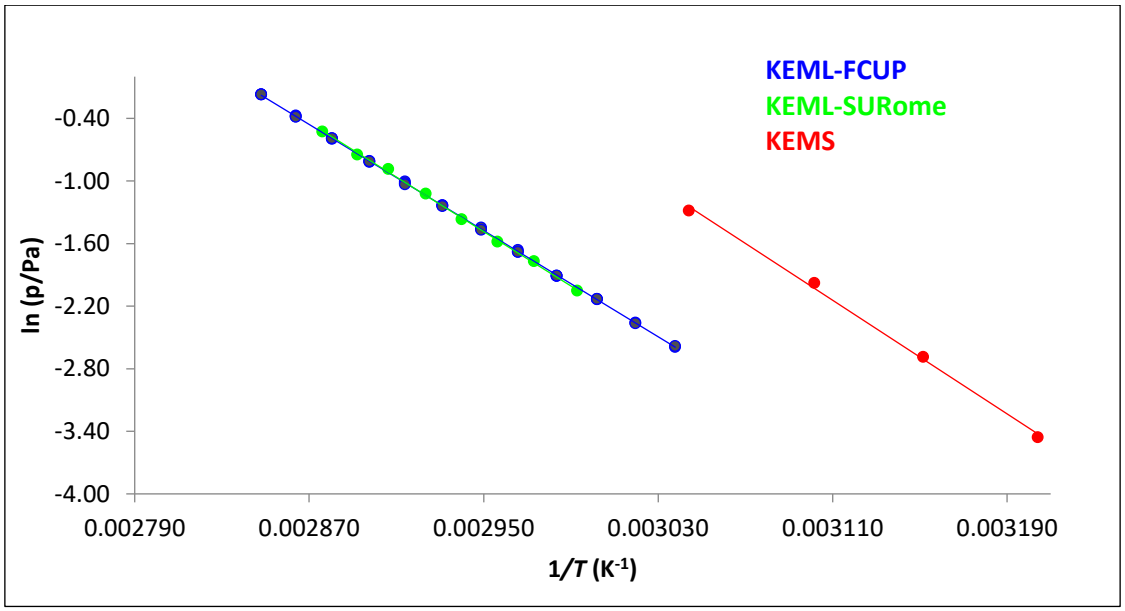

Figure 3.15 Comparison of the vapor pressure results for IDB obtained by KEML–FCUP (blue), KEML–SURome (green), and KEMS (red).

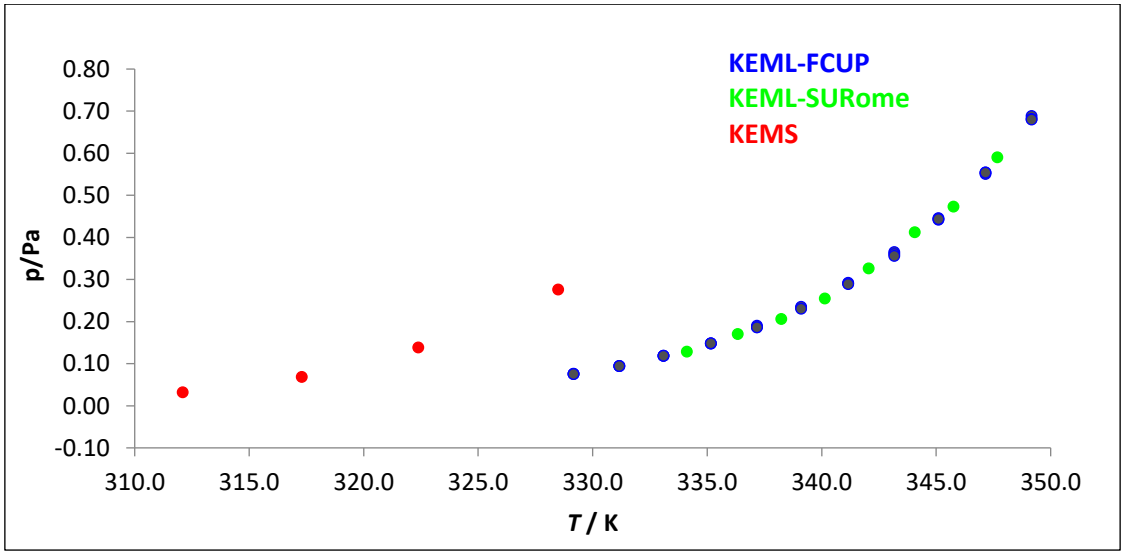

Figure 3.16 Vapor pressure of IDB as a function of temperature, obtained by KEML–FCUP (blue), KEML–SURome (green), and KEMS (red).

Table 3.15 Standard (p° = 0.1 MPa) molar enthalpies, $\Delta_{cr}^{g}H_m^\circ$, entropies, $\Delta_{cr}^{g}S_m^\circ$, and Gibbs energies, $\Delta_{cr}^{g}G_m^\circ$, of sublimation, and vapor pressure, p, at T = 298.15 K, for iminodibenzyl, obtained by different experimental techniques: Knudsen effusion at KEML-FCUP and KEML-SURome, and Knudsen effusion mass spectrometry (KEMS).[1]

Equipment	$\Delta_{cr}^{g}H_m^\circ$ / kJ·mol^{-1}	$\Delta_{cr}^{g}S_m^\circ$ / J·K^{-1}·mol^{-1}	$\Delta_{cr}^{g}G_m^\circ$/ kJ·mol^{-1}	p / Pa
KEML-Porto	107.4 ± 0.3	208.8 ± 0.9	45.1 ± 0.4	1.23×10^{-3}
KEML-SURome	110.2 ± 3.7	217 ± 11	45.5 ± 4.9	1.07×10^{-3}
KEMS	114 ± 16	241 ± 50	42 ± 22	4.13×10^{-3}

[1]The uncertainties quoted are the combined standard uncertainties (0.95 level of confidence).

3.1.3. 5-Acetyliminodibenzyl (AcIDB)

The third compound selected for this study was 5-acetyliminodibenzyl (1-(5,6-dihydrobenzo[b][1]benzazepin-11-yl)ethenone, CAS 13080-75-6), which belongs to the benzodiazepine family. The compound was obtained as an off-white crystalline powder, as summarized in Table 3.16. The presence of the acetyl group attached to the dibenzodiazepine core provides distinctive structural and physicochemical characteristics, making this molecule relevant for thermodynamic analysis and for comparison with structurally related compounds previously investigated.

Table 3.16 Properties and characteristics of 5-Acetyliminodibenzyl.

Compound	5-Acetyliminodibenzyl
IUPAC name	1-(5,6-dihydrobenzo[b][1]benzazepin-11-yl)ethanone
Structural formula	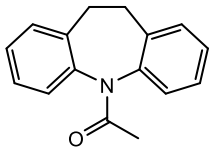
Molecular formula	$C_{16}H_{15}NO$
Molar mass / g·mol^{-1}	237.2964
CAS	13080-75-6
Density / g·cm^{-3}	1.264 [90]
Appearance	Off-white crystalline powder
Source / Specification	Aldrich, 99.9% (certificate of analysis, batch 13504CZ)

- **Purification and Purity Control**

The compound was initially purified by sublimation, despite its declared purity of 0.999 according to the certificate of analysis. This additional step aimed to remove any trace impurities, particularly inorganic residues that cannot be detected by GC-FID. After sublimation, the purity reached 0.9997.

Purity assessment was performed by gas–liquid chromatography (GLC), with methanol as the solvent. A baseline correction approach was applied: a blank methanol injection was first recorded to account for solvent contributions, followed by the analysis of the 5-acetyliminodibenzyl/methanol solution.

- **Thermal Analysis and Isothermal Thermogravimetry**

The DSC heating and cooling cycles were performed at rates of 2 and 10 $K \cdot min^{-1}$. In the heating runs, a sharp endothermic peak corresponding to the melting transition was observed. However, during cooling, no exothermic event associated with crystallization was detected at either cooling rate. This indicates that 5-acetyliminodibenzyl does not crystallize under the experimental conditions and instead forms a supercooled liquid. The absence of crystallization suggests a high kinetic barrier for nucleation, preventing the reorganization of the melt into a crystalline lattice. Furthermore, the similarity of the cooling curves at 2 and 10 $K \cdot min^{-1}$ demonstrates that the lack of crystallization is not strongly dependent on the cooling rate within this range, confirming the inherent tendency of the compound to remain in a metastable liquid state upon cooling.

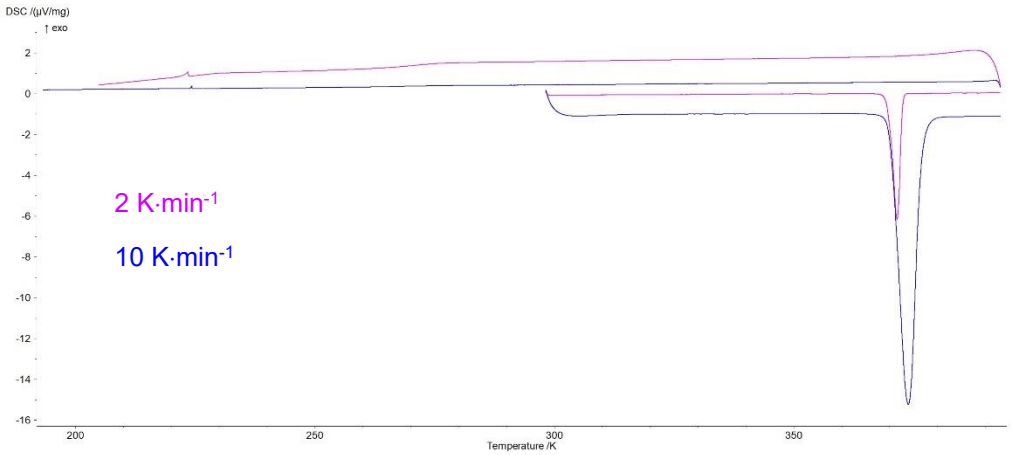

Figure 3.17 DSC heating and cooling curves of AcIDB recorded at 2 and 10 K·min^{-1}.

Fourier-transform infrared (FTIR) spectroscopy was employed in order to complement the thermal analysis and to gain further insight into the molecular features of 5-acetyliminodibenzyl. This technique was selected as it provides a rapid and reliable method for confirming the structural integrity of the compound and for detecting potential changes in the intermolecular interactions between the solid crystalline and liquid states. FTIR spectroscopy is particularly sensitive to functional groups such as the carbonyl and aromatic moieties, whose vibrational modes may exhibit shifts or variations depending on the degree of molecular order. Thus, the application of FTIR allowed us to verify the preservation of the chemical structure after thermal treatment and to highlight differences in band resolution and intensity associated with the transition from a crystalline solid to a supercooled liquid.

The ATR-FTIR spectra of 5-acetyliminodibenzyl were recorded for both the crystalline solid and the supercooled liquid in order to identify possible structural differences between the two states (Figure 3.18). The main functional groups, including the carbonyl stretching vibration around 1700 cm^{-1}, aromatic C=C stretching, and C–H stretching modes in the 3100-2850 cm^{-1} region, are present in both phases, confirming the chemical integrity of the compound after thermal treatment. However, clear spectral differences are observed between the solid and liquid states. In particular, the C–H stretching region near 3000 cm^{-1} shows pronounced broadening and intensity reduction in the liquid state, while in the crystalline solid the bands are sharper and more defined, reflecting the ordered environment of the lattice. Additional differences appear in the carbonyl and aromatic domains, as well as in the fingerprint region (1500-500 cm^{-1}), where the solid phase exhibits better-resolved bands in contrast to the broader and less defined features of the liquid. These findings, especially the marked changes near 3000

cm^{-1}, are consistent with the DSC results and confirm that upon cooling the compound does not recrystallize but remains in a supercooled liquid state with reduced intermolecular ordering.

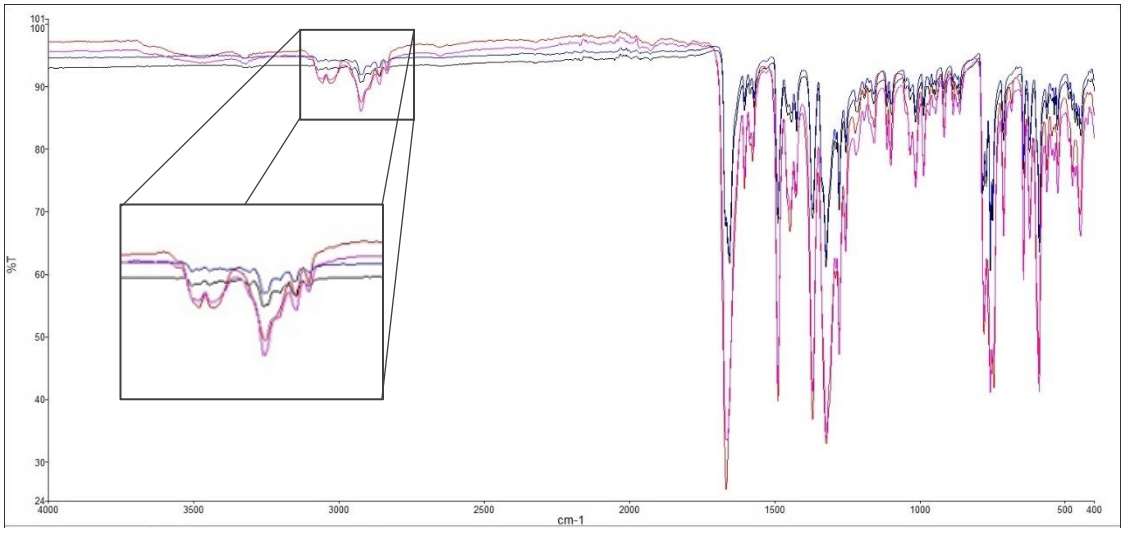

Figure 3.18 ATR-FTIR spectra of 5-acetyliminodibenzyl (AcIDB) recorded in the crystalline solid state (black line) and in the metastable liquid state (colored lines).

DSC experiments were carried out to determine the fusion temperature and the standard molar enthalpy of fusion of 5-acetyliminodibenzyl (AcIDB). The measurements were performed at a heating rate of 2 $K \cdot min^{-1}$, and five independent runs were conducted to ensure reproducibility. The results are summarized in Table 3.17. The compound exhibited a sharp and well-defined endothermic peak associated with the fusion process, with no evidence of crystal–crystal transitions detected at either 2 or 10 $K \cdot min^{-1}$ prior to melting (Figure 3.17). The average fusion temperature was determined as of ⟨368.6 ± 0.9⟩ K, while the corresponding standard molar enthalpy of fusion was obtained as ⟨22.3 ± 0.3⟩ $kJ \cdot mol^{-1}$, where the reported uncertainties represent the combined error, including the standard deviation of the mean, calibration uncertainties (temperature and energy), and a coverage factor of 2 (95% confidence level).

Table 3.17 Fusion temperature (T_{fus}) and standard molar enthalpy of fusion ($\Delta_{\mathrm{cr}}^{\mathrm{l}}H_{\mathrm{m}}^{\circ}\,(T_{\mathrm{fus}})$) of AcIDB obtained from DSC measurements at 2 K·min^{-1}.

T_{fus} / K	$\Delta_{\mathrm{cr}}^{\mathrm{l}}H_{\mathrm{m}}^{\circ}\,(T_{\mathrm{fus}})$ / kJ·mol^{-1}
368.44	22.34
368.87	22.31
368.71	22.49
368.54	22.25
368.48	22.28
< 368.6 ± 0.9>[1]	<22.3 ± 0.3>[1]

[1]Reported uncertainties correspond to the combined error, including the standard deviation of the mean, calibration uncertainties (temperature and energy), and a coverage factor of 2 (95% confidence level).

Simultaneous thermogravimetric–differential scanning calorimetry (TG-DSC) measurements were performed for AcIDB at a heating rate of 10 K·min⁻¹ in order to investigate its thermal stability and derive complementary thermodynamic data (Figure 3.19). The DSC trace exhibits a sharp endothermic event corresponding to the melting process, in agreement with the previous DSC measurements. Upon further heating, a second endothermic process is observed, accompanied by a significant mass loss in the TG curve, which is attributed to the vaporization of the compound. No evidence of solid-solid transitions was detected before melting, confirming the stability of the crystalline phase up to the fusion temperature.

From the isothermal thermogravimetry analysis, reliable values for the standard molar enthalpies of fusion, vaporization, and sublimation (corrected to 298.15 K) were derived, and are summarized in Table 3.18.

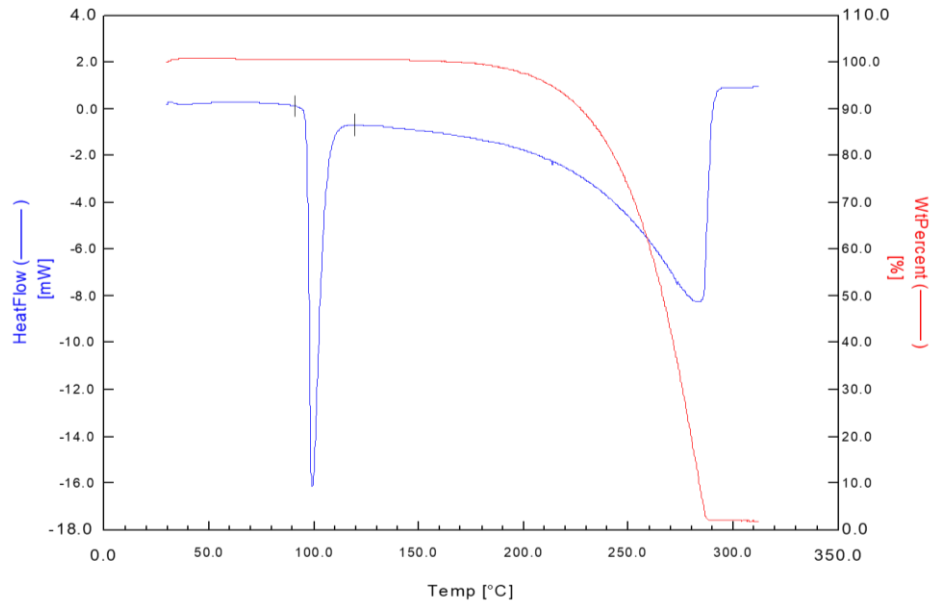

Figure 3.19 Simultaneous thermogravimetric–differential scanning calorimetry (TG–DSC) curves of AcIDB, obtained at a heating rate of 10 K·min^{-1}.

Table 3.18 Thermodynamic results for AcIDB obtained from isothermal thermogravimetry (TG-DSC): fusion enthalpy, vaporization enthalpy, and sublimation enthalpy corrected to 298.15 K.

$\langle T \rangle$ / K	$\Delta_{cr}^{l} H_m^{\circ}(298.15\mathrm{K})$ / kJ·mol^{-1}	$\Delta_{l}^{g} H_m^{\circ}(298.15\mathrm{K})$ / kJ·mol^{-1}	$\Delta_{cr}^{g} H_m^{\circ}(298.15K)$ / kJ·mol^{-1}
493.68	14.72	107.86	122.58
493.42	15.12	109.06	124.18
493.50	15.93	105.86	121.78
493.50	15.94	108.38	124.32
< 493.53 ± 0.05>[1]	<15.4 ± 0.3>[1]	<107.8 ± 0.7>[1]	<123.2 ± 0.6>[1]

[1]Reported uncertainties correspond to the the standard deviation of the mean.

- **Vapor Pressure Studies: KEML and KEMS Approaches**

Knudsen effusion measurements of AcIDB were conducted at KEML-FCUP within the temperature interval [344.16–366.13] K, providing vapor pressure values between 0.06 and 0.89 Pa (Table 3.19). The corresponding ln(*p*/Pa) versus 1/*T* representations obtained for the small, medium, and large orifices are depicted in Figure 3.20, together with the fitted Clausius–Clapeyron lines. As illustrated in Figure 3.21, the results from the three orifice sizes are fully consistent, demonstrating that dynamic equilibrium was achieved inside the effusion cell. Consequently, the complete dataset was employed for the determination of the sublimation thermodynamic parameters.

Table 3.19 Knudsen effusion mass-loss experimental results for 5-acetyliminodibenzyl (acIDB), obtained at FCUP.[1]

T / K [2]	t / s	Orifices [3]	m / mg [4]			p / Pa [5]		
			m_S	m_M	m_L	p_S	p_M	p_L
344.16	45635	S3-M6-L9	5.22	8.10	12.02	0.0636	0.0625	0.0648
346.20	45635	S2-M5-L8	7.02	10.71	15.51	0.0847	0.0838	0.0843
348.13	45635	S1-M4-L7	8.67	13.37	19.04	0.1063	0.1062	0.1062
350.17	29371	S3-M6-L9	7.10	11.44	15.73	0.1356	0.1383	0.1328
352.18	29371	S2-M5-L8	9.62	14.89	20.31	0.1820	0.1825	0.1729
354.11	29371	S1-M4-L7	11.88	18.19	25.62	0.2283	0.2264	0.2240
356.17	19489	S3-M6-L9	9.68	15.45	21.68	0.2810	0.2839	0.2783
358.18	19489	S2-M5-L8	12.58	20.05	27.55	0.3617	0.3735	0.3564
359.16	8745	S3-M6-L9	6.17	9.85	13.83	0.4008	0.4050	0.3973
360.12	19489	S1-M4-L7	—	24.23	34.86	—	0.4583	0.4630
361.14	8745	S2-M5-L8	7.91	12.10	17.26	0.5089	0.5044	0.4997
362.16	11967	S3-M6-L9	11.66	18.54	26.18	0.5558	0.5594	0.5519
363.10	8745	S1-M4-L7	9.66	14.96	21.50	0.6314	0.6332	0.6391
364.17	11967	S2-M5-L8	14.97	22.92	32.73	0.7067	0.7011	0.6954
366.13	11967	S1-M4-L7	18.55	28.44	41.06	0.8896	0.8833	0.8956

[1]The subscripts S, M, L of the variables m (mass effused) and p (vapor pressure) correspond to the results obtained through the small (S1, S2, and S3), the medium (M4, M5, and M6) and the large (L7, L8, and L9) effusion orifices, respectively; [2]The standard uncertainty of the measured temperature is $\pm (1 \cdot 10^{-2})$ K;
[3]The values areas, A_0, and transmission probability Clausing factors, ω_0, for each effusion orifice are given in Table A1 of appendix. [4]The standard uncertainty is $\pm (1 \cdot 10^{-2})$ mg according to manufacturer's specifications (Analytical Balance Mettler Toledo EA 163); [5]The standard uncertainty is $\pm (3 \cdot 10^{-2})$ Pa.

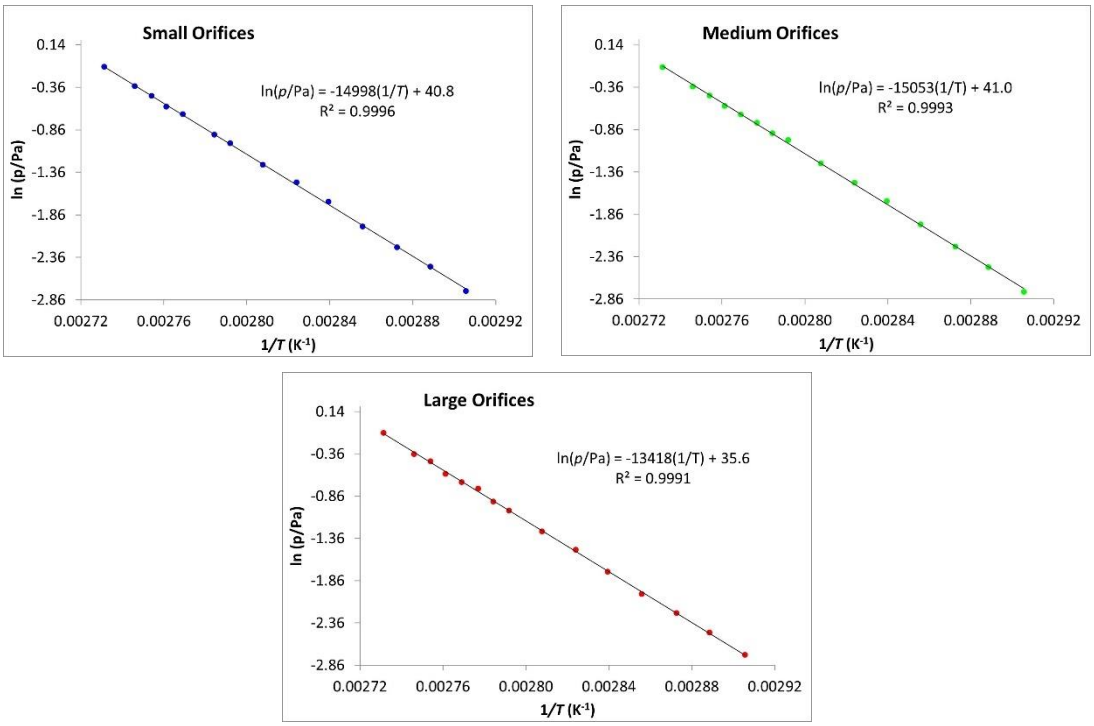

Figure 3. 20 Dependence of ln(p/Pa) on 1/T for AcIDB, obtained by the Knudsen effusion method using the KEML-FCUP system with small (blue), medium (green), and large (red) orifices. The lines correspond to the linear fit of the Clausius–Clapeyron equation.

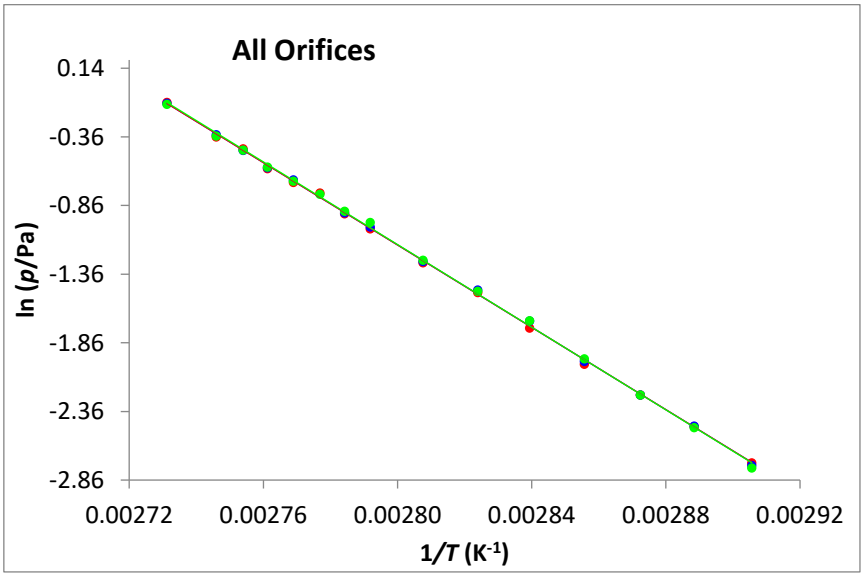

Figure 3.21 Dependence of ln(p/Pa) on 1/T for AcIDB obtained by the Knudsen effusion method using the KEML-FCUP system. The experimental data from small (blue), medium (green), and large (red) orifices are superimposed.

Knudsen effusion mass-loss experiments on AcIDB were also performed at SURome in order to determine its vapor pressures over the temperature range 341–361 K. Two independent experimental runs were carried out, and the results are summarized in Table 3.20. The results from the two experimental sets do not fully agree (Figure 3.22), the slopes of the ln(p) vs 1/T plots differ significantly, leading to discrepancies in the derived sublimation enthalpies (Table 3.22). This lack of internal consistency indicates the presence of systematic deviations between the two runs, and therefore the SURome dataset must be interpreted with caution. For the final determination of sublimation enthalpy, Essay 2 was selected, as it is considered to have benefitted from a longer stabilization period, ensuring more reliable equilibrium conditions.

Table 3.20 Knudsen effusion mass loss (SURome) experimental results for AcIDB.

T / K	Δt / s	Δm / mg	p / Pa
Essay 1			
341.20 ± 0.20	10526	0.429 ± 0.010	0.0318 ± 0.0022
345.04 ± 0.20	12660	0.939 ± 0.010	0.0581± 0.0035
347.03 ± 0.20	8993	0.894± 0.010	0.0782 ± 0.0047
349.06 ± 0.20	9244	1.275± 0.010	0.1087 ± 0.0063
350.99 ± 0.20	5437	1.017± 0.010	0.1478 ± 0.0087
352.94 ± 0.20	4564	1.115 ± 0.010	0.1936 ± 0.0112
356.72 ± 0.20	3465	1.551 ± 0.010	0.3568 ± 0.0199
358.62 ± 0.20	3400	2.080 ± 0.010	0.4888 ± 0.0265
360.42 ± 0.20	3433	2.896 ± 0.010	0.6758 ± 0.0359
Essay 2			
341.25 ± 0.20	14532	0.705 ± 0.010	0.0378 ± 0.0024
344.97 ± 0.20	10501	0.863 ± 0.010	0.0644 ± 0.0039
346.89± 0.20	7350	0.855 ± 0.010	0.0914 ± 0.0056
348.91 ± 0.20	7542	1.153 ± 0.010	0.1204 ± 0.0070
350.92 ± 0.20	4759	0.939 ± 0.010	0.1560 ± 0.0093
352.83 ± 0.20	4678	1.263 ± 0.010	0.2140 ± 0.0123
354.74 ± 0.20	3286	1.197± 0.010	0.2894 ± 0.0166
356.80 ± 0.20	3189	1.487 ± 0.010	0.3715 ± 0.0207
358.66 ± 0.20	3480	2.146 ± 0.010	0.4928 ± 0.0267
360.63 ± 0.20	3011	2.450 ± 0.010	0.6520 ± 0.0349

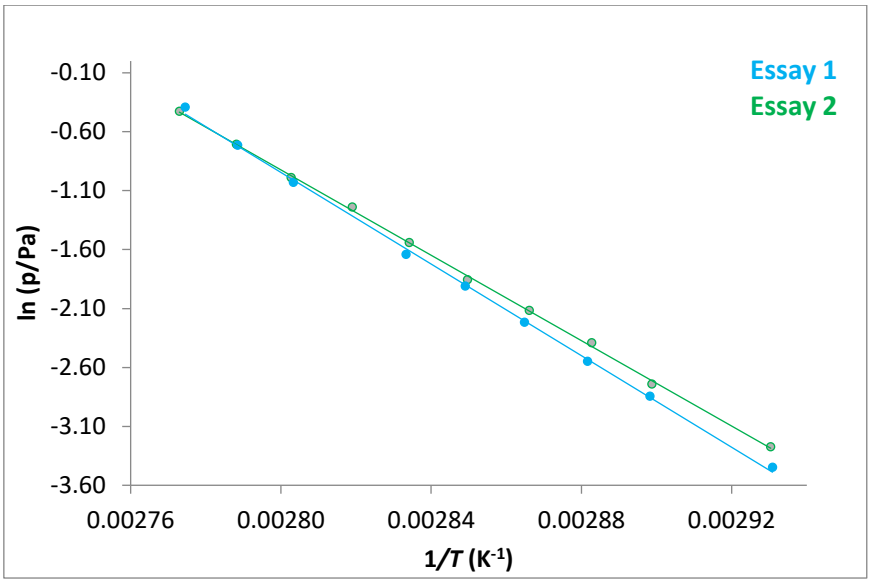

Figure 3. 22 Dependence of ln(p/Pa) on 1/T for AcIDB obtained by the Knudsen effusion method using the KEML-SURome system.

Knudsen effusion mass spectrometry (KEMS) experiments were also carried out for AcIDB, and the corresponding results are summarized in Table 3.21. Two independent experimental sets were performed, covering the temperature ranges 321.1–334.0 K (Essay 1) and 315.9–333.3 K (Essay 2). For each measurement, the ion beam intensity was recorded and converted into vapor pressure values using the instrumental calibration constant. The plots of ln(*p*/Pa) versus 1/*T* are shown in Figure 3.23. Although both essays follow the expected linear behaviour predicted by the Clausius–Clapeyron equation, the data display a noticeable degree of scatter, particularly at the lower temperature end where the ion signals are weaker. As expected for this compound, only the molecular ion and characteristic fragment ions of AcIDB were observed in the gas phase. No additional species or unexpected peaks were detected, confirming the absence of decomposition or molecular association during sublimation.

Table 3.21 Knudsen effusion mass spectrometry (KEMS) experimental results for AcIDB.

T / K	Ticks	Scale	I^+	p / Pa
		Essay 1		
321.1	23.0	0.1	2.6137	0.00601
327.1	17.0	0.3	5.7956	0.01359
334.0	11.5	1.0	13.0686	0.03128
		Essay 2		
315.9	9.5	0.1	1.0796	0.00244
320.2	17.0	0.1	1.9319	0.00443
325.9	11.0	0.3	3.7501	0.00876
333.3	9.0	1.0	10.2276	0.02443

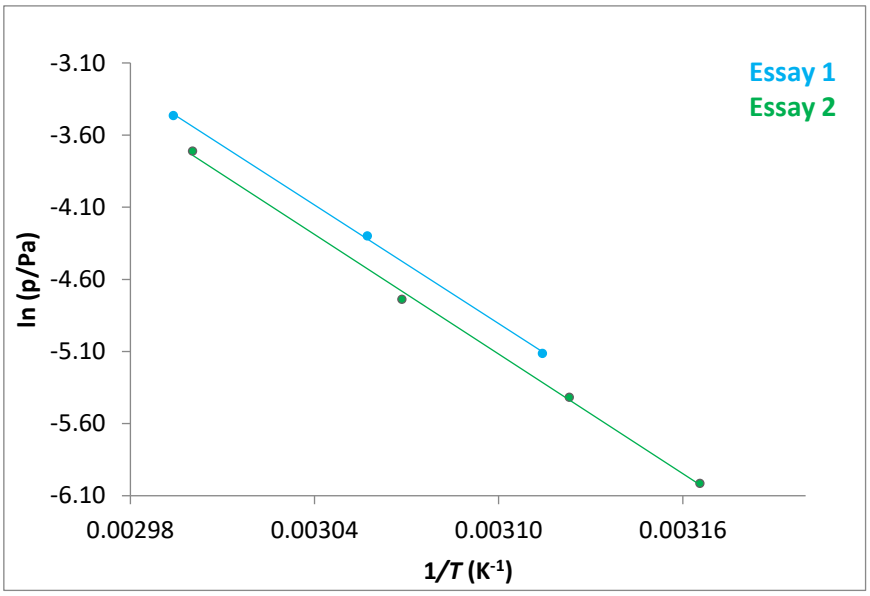

Figure 3.23 Dependence of ln(p/Pa) on 1/T for AcIDB obtained by KEMS. The results correspond to two experimental sets: Essay 1 (blue) and Essay 2 (green).

Table 3.22 Thermodynamic parameters of sublimation of AcIDB derived from vapor pressure measurements obtained by Knudsen effusion at KEML–FCUP and KEML–SURome, and by Knudsen effusion mass spectrometry (KEMS). Parameters a and b correspond to the intercept and slope of the Clausius–Clapeyron equation.

Set/ Essay	*a*	*b*	$p(\langle T \rangle)$ / Pa	$\Delta_{cr}^{g} H_m(\langle T \rangle)$ / kJ·mol^{-1}	$\Delta_{cr}^{g} S_m(\langle T \rangle, p\langle T \rangle)$/ J·K^{-1}·mol^{-1}
KEML - FCUP					
Small Orifices	40.8 ± 0.5[1]	14998 ± 190 [1]	0.239 <355.15K>	124.7 ± 1.6 [8]	351.1 ± 4.5 [8]
Medium Orifices	41.0 ± 0.7 [2]	15053 ± 232 [2]	0.250 <355.15K>	125.2 ± 1.9 [8]	352.5 ± 5.3 [8]
Large orifices	40.9 ± 0.5 [2]	15030 ± 187 [2]	0.242 <355.15K>	125.0 ± 1.6 [8]	352.0 ± 4.5 [8]
All Orifices	40.9 ± 0.3 [3]	15027 ± 108 [3]	0.244 <355.15K>	124.9 ± 0.9 [8]	351.7 ± 2.5 [8]
KEML-SURome					
Essay 1	53.5 ± 1.6 [4]	19438 ± 562 [4]	0.148 <350.81>	161.6 ± 4.7 [8]	461 ± 13 [8]
Essay 2	49.8 ± 1.0 [5]	18118 ± 351 [5]	0.161 <350.94>	150.6 ± 2.9 [8]	429.1 ± 8.0 [8]
KEMS					
Essay 1	38 ± 12 [6]	13699 ± 3872 [6]	0.0219 <327.55>	114 ± 32 [8]	348 ± 99 [8]
Essay 2	37.3 ± 5.0 [6]	13819 ± 1623 [6]	0.00514 <324.62>	115 ± 13 [8]	354 ± 40 [8]

The standard uncertainties were obtained by multiplying the standard error of the fitting parameters by a coverage factor k corresponding to the t-distribution value for a 0.95 confidence level and the respective degrees of freedom:
[1] k=2.18 (12 degrees of freedom); [2] k=2.16 (13 degrees of freedom); [3] k=2.02 (42 degrees of freedom); [4] k=2.36 (7 degrees of freedom); [5] k=2.31 (8 degrees of freedom); [6] k=12.7 (1 degrees of freedom); [7] k=4.30 (2 degrees of freedom);
[8] The uncertainties quoted are the combined standard uncertainties (0.95 level of confidence).

The vapor pressure results obtained by the different effusion techniques are compared in Figures 3.24 and 3.25, while the corresponding thermodynamic parameters derived at 298.15 K are summarized in Table 3.23. The Knudsen effusion measurements performed at KEML–FCUP and at KEML–SURome show reasonably consistent trends, although the enthalpies of sublimation differ by almost 25 kJ·mol⁻¹. This discrepancy likely reflects the differences already noted between the two essays performed at SURome, which may be attributed to insufficient stabilization time or to subtle variations in sample preparation, resulting in systematic deviations in that dataset.

The KEMS results, although affected by larger scatter and calibration uncertainties, provide a lower enthalpy of sublimation of (116 ± 13 kJ·mol^{-1}) and a significantly smaller entropy value compared with the Knudsen effusion experiments. These differences are consistent with the reduced sensitivity of the method to absolute vapor pressure values, as the instrumental calibration constant introduces additional uncertainty in the intercept of the Clausius–Clapeyron plots.

Taken together, the three independent experimental approaches confirm the overall consistency of the sublimation process of AcIDB, but they also highlight the sensitivity of the derived thermodynamic parameters to the specific technique and experimental conditions. In particular, the FCUP Knudsen effusion data appears the most reliable due to their internal consistency across different orifice sizes and the lower associated uncertainties, and they were therefore selected as the reference dataset for subsequent thermodynamic analysis.

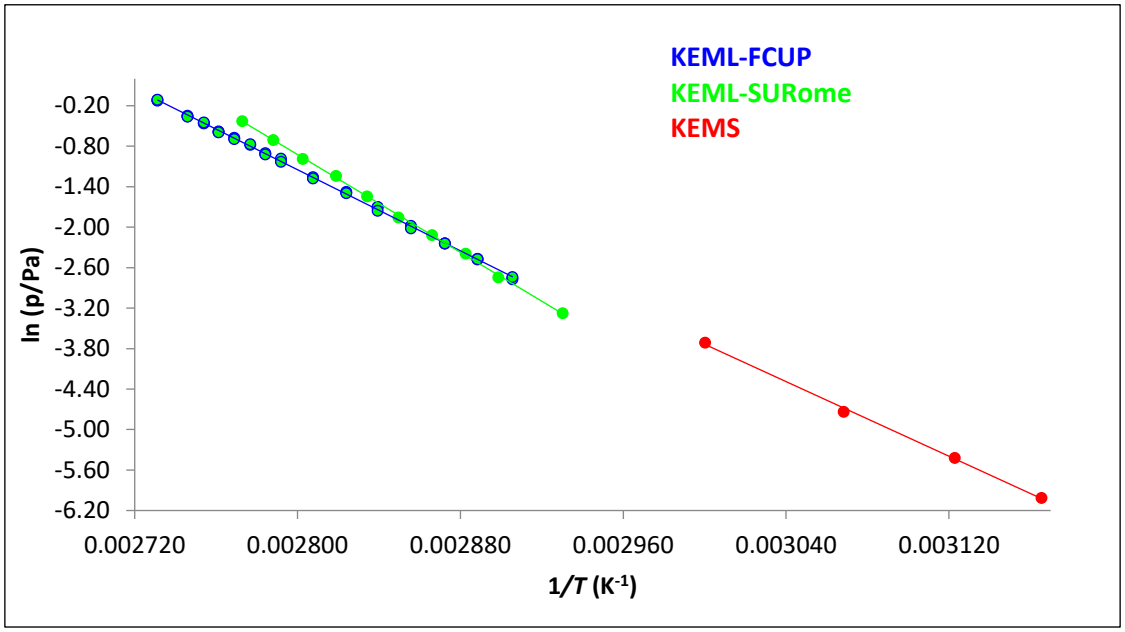

Figure 3.24 Comparison of the vapor pressure results for AcIDB obtained by KEML–FCUP (blue), KEML–SURome (green), and KEMS (red).

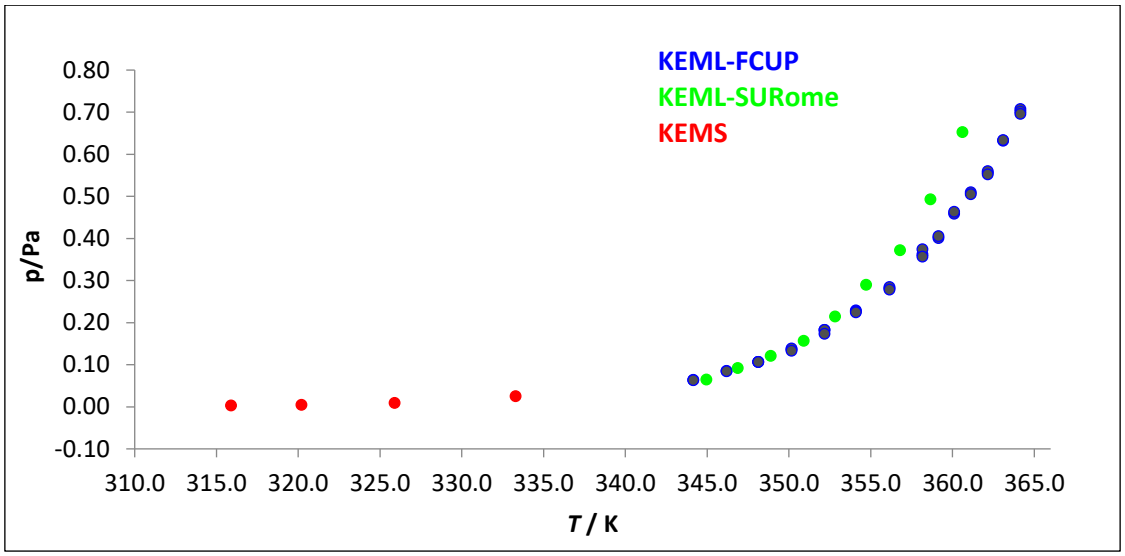

Figure 3. 25 Comparison of the vapor pressure results for AcIDB obtained by KEML–FCUP (blue), KEML–SURome (green), and KEMS (red).

Table 3.23 Standard (p° = 0.1 MPa) molar enthalpies, $\Delta^g_{cr}H^\circ_m$, entropies, $\Delta^g_{cr}S^\circ_m$, and Gibbs energies, $\Delta^g_{cr}G^\circ_m$, of sublimation, and vapor pressure, *p*, at *T* = 298.15 K, for 5-acetyliminodibenzyl, obtained by different experimental techniques: Knudsen effusion at KEML-FCUP and KEML-SURome, and Knudsen effusion mass spectrometry (KEMS).[1]

Equipment	$\Delta^g_{cr}H^\circ_m$ / kJ·mol^{-1}	$\Delta^g_{cr}S^\circ_m$ / J·K^{-1}·mol^{-1}	$\Delta^g_{cr}G^\circ_m$/ kJ·mol^{-1}	p / Pa
KEML-Porto	127.6 ± 0.9	252.5 ± 2.5	52.3 ± 1.2	6.83 × 10^{-5}
KEML-SURome	153.1 ± 2.9	325.9 ± 8.3	55.9 ± 3.8	1.59 × 10^{-5}
KEMS	116 ± 13	218 ± 40	51 ± 18	1.16 × 10^{-4}

[1]The uncertainties quoted are the combined standard uncertainties (0.95 level of confidence).

3.2. Thermochemical Studies

Hydrogenation enthalpies provide valuable insights into molecular stability and are particularly relevant in the design of hydrogen storage materials. According to DOE guidelines, the optimal enthalpy range for reversible hydrogen storage lies between –40 and –60 kJ·mol^{-1} (gas phase, 298–350 K) per H_2, thus enabling a direct comparison between calculated values and the energetic requirements for practical applications.

The predictive strength of theoretical calculations is especially valuable when experimental data are unavailable, hazardous to obtain, or technically challenging. In this work, the G3(MP2)//B3LYP composite method was selected as a reliable framework for the computation of gas-phase enthalpies of formation of the studied azepan derivatives,

enabling the subsequent determination of position-dependent hydrogenation enthalpies. It was considered one 1,2-addition of H_2 per aromatic bond (i.e., a single dihydrogenation step), restricting the reaction to the benzene ring of each scaffold. For every case, the lowest-energy conformer (global minimum; no imaginary frequencies) was used.

General reaction for the position-selective 1,2-hydrogenation (single H_2 addition),

$$\mathrm{X\,(g)} + \mathrm{H_2\,(g)} \rightarrow \mathrm{X[H_i, H_j]\,(g)} \quad (3.1)$$

where X is IMB, IDB or AcIDB and i, j denotes the specific aromatic bond (C_1–C_2, C_3–C_4, C_5–C_6, …). The product $\mathrm{X[H_i, H_j]}$ is the i,j-dihydro derivative with H atoms added at carbons i and j.

The enthalpy change for addition at a given bond is calculated by eq. 3.2.

$$\Delta H_{\mathrm{hyd}}(C_i - C_j, g) = H^{\circ}_{298.15K}\left(X[H_i, H_j], g\right) - H^{\circ}_{298.15K}(X, g) - H^{\circ}_{298.15K}(H_2, g) \quad (3.2)$$

In table 3.24 are the position-resolved values of $-\Delta H^{\circ}{}_{\mathrm{hyd}}\,(\mathrm{g})\ \mathrm{per}\ \mathrm{H_2}$ at 298.15 K, which show a clear site and scaffold dependence.

For IMB, the most exothermic ring site is C_5–C_6 (42.2 kJ·mol^{-1}), which lies within the DOE window (≈40–60 kJ·mol^{-1} in magnitude), whereas C_1–C_2 (29.9 kJ·mol^{-1}) and C_3–C_4 (26.1 kJ·mol^{-1}) are less exothermic. Notably, hydrogenation at the ethylenic C_7–C_8 bond (the linker between the two benzene rings) is much stronger as expected, with ΔH_{hyd}=88.4 kJ·mol^{-1} per H2. This enhanced driving force is consistent with saturating the isolated C=C while preserving both aromatic sextets; by contrast, 1,2-addition on the ring dearomatizes the benzene ring and is therefore less exothermic. From a storage standpoint, the C_7–C_8 value exceeds the DOE range and would require higher temperatures for H_2 release than ring sites near 40–60 kJ·mol^{-1}.

For IDB, hydrogenation is moderately exothermic at all positions. The C_5–C_6 site (37.7 kJ·mol^{-1}) lies just below the DOE lower bound but can be considered a near-threshold candidate—likely viable under modestly elevated H_2 pressures or slightly reduced temperatures. By contrast, C_1–C_2 and C_3–C_4 (both 30.8 kJ·mol^{-1}) are appreciably weaker and are unlikely to support efficient room-temperature loading at modest pressures.

Table 3.24 Position-resolved gas-phase hydrogenation enthalpies, for the IMB, IDB and AcIDB scaffolds. Values at 298.15 K

	$-\Delta H^{\circ}_{hyd}$ (g) per H_2 / kJ·mol^{-1}			
Hydrogen Addition	**C_1-C_2**	**C_3-C_4**	**C_5-C_6**	**C_7-C_8**
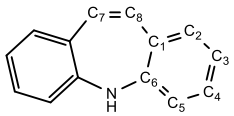 **IMB**	29.9	26.1	42.2	88.4
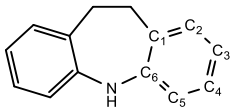 **IDB**	30.8	30.8	37.7	—
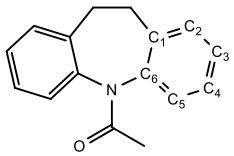 **AcIDB**	36.2	33.2	21.9	—

For AcIDB, positional effects are more pronounced: hydrogenation at C_5–C_6 is the least exothermic of all sites (21.9 kJ·mol^{-1}), whereas C_1–C_2 and C_3–C_4 yield 36.2 and 33.2 kJ· mol^{-1}, respectively. The attenuation at C5–C6 is consistent with deactivation by the acyl group—via electron-withdrawing effects and local polarization, which diminishes the enthalpic benefit of adding H_2 adjacent to the carbonyl.

4. Final Remarks

This work provides a consistent thermophysical and thermodynamic picture for azepan derivatives. Condensed-phase transitions (crystal-crystal and crystal-liquid) were characterized by DSC, and, when required, by simultaneous TG–DSC to distinguish enthalpic events from mass loss. The crystal-gas pathway was quantified by Knudsen effusion (mass-loss) using two independent setups (at FCUP and at SURome) and complemented by Knudsen effusion mass spectrometry (KEMS) to verify vapor composition. Quartz crystal microbalance (QCM) measurements were also explored for sublimation studies; however, for the azepan derivatives the open-cell configuration proved unsuitable. The sublimation flux and deposition onto the quartz resonator could not be adequately controlled or quantified, preventing a reliable determination of the enthalpy of sublimation.

Thermal screening highlighted two contrasting cases:

- IMB melts cleanly but exhibits rapid mass loss after melting, consistent with appreciable volatilization in the temperature range-therefore it is disfavoured as a neat LOHC.
- By contrast, AcIDB melts at a lower temperature and can be kept in the liquid state, showing pronounced supercooling on cooling; this facilitates liquid-phase storage and transport. To confirm practical viability, its recrystallisation kinetics should be mapped to delineate operating windows free of solid formation.

Table 4.1 compiles the thermophysical data: melting temperatures and fusion enthalpies measured by DSC, and sublimation enthalpies at reference temperature determined by Knudsen effusion (KEML) at two laboratories (FCUP and Sapienza), Knudsen effusion mass spectrometry (KEMS), and isothermal thermogravimetry (ITG) for the azepan derivatives:

- **IMB.** The three applied techniques (KEML–FCUP, KEML–Sapienza, KEMS) are mutually consistent within their stated uncertainties, indicating good inter-technique reproducibility for this compound.
- **IDB.** KEML–FCUP and KEML–Sapienza are in agreement within uncertainty. KEMS shows a very large uncertainty band and sits somewhat offset from the KEML values, while ITG is more precise but systematically higher, suggesting a small positive bias, yet still useful as an external reference.

- **AcIDB.** There is good proximity between KEML–FCUP and ITG, whereas KEML–Sapienza and KEMS diverge. For this compound the stabilization times were short, so the discrepancies are unlikely to stem from slow equilibration; they more likely reflect setup-specific factors (effusion regime, sample handling).

The KEML-FCUP results are internally very robust for the three compounds, IMB (113.9 ± 1.4) kJ·mol^{-1}, IDB (107.4 ± 0.3) kJ·mol^{-1}, AcIDB (127.6 ± 0.9) kJ·mol^{-1}, with tight uncertainties and good agreement between different orifice diameters, indicating operation in the molecular regime and stable effusion conditions. These values therefore provide a reliable reference set. Moreover, KEMS proved especially valuable by directly probing the gas phase and confirming a predominantly monomeric vapor, thereby ruling out dimeric (or clustered) species under the measurement conditions.

Table 4.1 Thermophysical Properties of Azepan Derivatives Determined Using a Multi-Technique Approach.

T_{fus} / K	$\Delta^{l}_{cr}H^{\circ}_{m}(T_{fus})$ / kJ·mol^{-1}	$\Delta^{g}_{cr}H^{\circ}_{m}$(298.15K) / kJ·mol^{-1}			
		KEML-FCUP	KEML-SURome	KEMS	ITG
IMB					
471.9 ± 0.9	<33.1 ± 0.4>	113.9 ± 1.4	115.0 ± 4.5	112.1 ± 3.7	—
IDB					
380.1 ± 0.9	24.2 ± 0.3	107.4 ± 0.3	110.2 ± 3.7	114 ± 16	112.5 ± 0.2
AcIDB					
368.6 ± 0.9	22.3 ± 0.3	127.6 ± 0.9	153.1 ± 2.9	116 ± 13	123.2 ± 0.6

In the thermochemical assessment of azepan derivatives as candidates for hydrogen carriers, **gas-phase calculations at 298.15 K (G3(MP2)//B3LYP)** rank the hydrogenation sites as follows:

- **IMB** shows C_5–C_6 42.2 kJ·mol^{-1} per H_2 (within the DOE window), while C_1–C_2 and C_3–C_4 are weaker; the ethylenic C7–C8 (88.4 kJ·mol^{-1}) is much stronger and thus unfavorable for reversible release.
- **IDB** is moderate overall, with C_5–C_6 (37.7 kJ·mol^{-1}) near-threshold.
- **AcIDB** shows ring-site hydrogenations uniformly weaker. None fall within the DOE 40–60 kJ·mol^{-1} window.

Although AcIDB's lower magnitudes favour H_2 release and could allow equilibrium loading under moderately elevated pressures or slightly reduced temperatures, its appeal rests chiefly on **handling advantages** (low melting temperature and supercooling) rather than energetics. A key open point is **framework robustness** under cycling - i.e., resistance to hydrogenolysis or carbonyl reduction. Overall, these trends single out IMB C_5–C_6 as the most viable site among those surveyed and flag the others as non-ideal starting points for OHC design.

5. References

1. Union, E., *Establishing the Framework for Achieving Climate Neutrality and Amending Regulations (EC) No 401/2009 and (EU) 2018/1999 ('European Climate Law')*. 2021, European Commission Brussels, Belgium.
2. Yang, Z., et al., *Electrochemical energy storage for green grid.* Chemical reviews, 2011. **111**(5): p. 3577-3613.
3. Züttel, A., *Materials for hydrogen storage.* Materials today, 2003. **6**(9): p. 24-33.
4. Ma, T., et al., *Technical feasibility study on a standalone hybrid solar-wind system with pumped hydro storage for a remote island in Hong Kong.* Renewable energy, 2014. **69**: p. 7-15.
5. Faraji, F., A. Majazi, and K. Al-Haddad, *A comprehensive review of flywheel energy storage system technology.* Renewable and Sustainable Energy Reviews, 2017. **67**: p. 477-490.
6. Louie, H. and K. Strunz, *Superconducting magnetic energy storage (SMES) for energy cache control in modular distributed hydrogen-electric energy systems.* IEEE Transactions on Applied Superconductivity, 2007. **17**(2): p. 2361-2364.
7. Abedin, A.H. and M.A. Rosen, *A critical review of thermochemical energy storage systems.* The open renewable energy journal, 2011. **4**(1): p. 42-46.
8. Mori, D. and K. Hirose, *Recent challenges of hydrogen storage technologies for fuel cell vehicles.* International journal of hydrogen energy, 2009. **34**(10): p. 4569-4574.
9. https://www.chiyodacorp.com/en/service/lowcarbon/hydrogen/demonstration/.
10. Ximenes, M.C., et al., *Organic Electronics: Basic Fundamentals and Recent Applications Involving Carbazole-Based Compounds.* Processes, 2024. **12**(12): p. 2945.
11. Weinhold, T.D., et al., *Assessing carbazole derivatives as single-electron photoreductants.* The Journal of Organic Chemistry, 2022. **87**(24): p. 16928-16936.
12. Bekkar, F., et al., *Polycarbazole and its derivatives: Synthesis and applications. A review of the last 10 years.* Polymers, 2020. **12**(10): p. 2227.
13. Stark, K., et al., *Liquid organic hydrogen carriers: thermophysical and thermochemical studies of carbazole partly and fully hydrogenated derivatives.* Industrial & Engineering Chemistry Research, 2015. **54**(32): p. 7953-7966.
14. Arai, A., et al., *π-Extended carbazole derivatives as host materials for highly efficient and long-life green phosphorescent organic light-emitting diodes.* Chemistry–A European Journal, 2021. **27**(15): p. 4971-4976.

15. Lei, J., et al., *Azepine Modulation in Thermally Activated Delayed Fluorescence Emitters for OLEDs Achieving Nearly 40% EQE.* ACS Materials Letters, 2025. **7**(5): p. 1896-1904.
16. Bui, T.-T., et al., *Thermally activated delayed fluorescence emitters for deep blue organic light emitting diodes: A review of recent advances.* Applied Sciences, 2018. **8**(4): p. 494.
17. Tan, K.C., et al., *Strategies of thermodynamic alternation on organic hydrogen carriers for hydrogen storage application: A review.* Green Energy and Resources, 2023. **1**(2): p. 100020.
18. Jung, J., et al., *Catalytic hydrogenation and dehydrogenation reactions of n-alkyl-bis (Carbazole)-based hydrogen storage materials.* Catalysts, 2021. **11**(1): p. 123.
19. Emel'yanenko, V.N., et al., *Hydrogen storage: thermochemical studies of N-alkylcarbazoles and their derivatives as a potential liquid organic hydrogen carriers.* The Journal of Physical Chemistry C, 2015. **119**(47): p. 26381-26389.
20. Cavallo, G., et al., *The halogen bond.* Chemical reviews, 2016. **116**(4): p. 2478-2601.
21. Malinge, A., et al., *Heavy Atom Effect in Halogenated mCP and Its Influence on the Efficiency of the Thermally Activated Delayed Fluorescence of Dopant Molecules.* The Journal of Physical Chemistry C, 2024. **128**(3): p. 1122-1130.
22. Stark, K., et al., *Melting points of potential liquid organic hydrogen carrier systems consisting of N-alkylcarbazoles.* Journal of Chemical & Engineering Data, 2016. **61**(4): p. 1441-1448.
23. Møller, K.T., et al., *Hydrogen-A sustainable energy carrier.* Progress in natural science: Materials International, 2017. **27**(1): p. 34-40.
24. Energy, U.S.D.o. *Hydrogen and Fuel Cells*. February 2025]; Available from: https://www.energy.gov/eere/fuelcells/hydrogen-.
25. Palmer, C., *Hydrogen power focus shifts from cars to heavy vehicles.* 2020.
26. Dincer, I., N. Javani, and G.K. Karayel, *Sustainable city concept based on green hydrogen energy.* Sustainable Cities and Society, 2022. **87**: p. 104154.
27. McPherson, M., N. Johnson, and M. Strubegger, *The role of electricity storage and hydrogen technologies in enabling global low-carbon energy transitions.* Applied Energy, 2018. **216**: p. 649-661.
28. Xu, Y., et al., *Research Progress and Application Prospects of Solid-State Hydrogen Storage Technology.* Molecules, 2024. **29**(8): p. 1767.

29. Liu, J., et al., *Numerical study on the fast filling of on-bus gaseous hydrogen storage cylinder.* International Journal of Hydrogen Energy, 2020. **45**(15): p. 9241-9251.
30. Yanxing, Z., et al., *Thermodynamics analysis of hydrogen storage based on compressed gaseous hydrogen, liquid hydrogen and cryo-compressed hydrogen.* International Journal of Hydrogen Energy, 2019. **44**(31): p. 16833-16840.
31. Song, Z., J. Xu, and X. Chen, *Design and optimization of a high-density cryogenic supercritical hydrogen storage system based on helium expansion cycle.* International Journal of Hydrogen Energy, 2024. **49**: p. 1401-1418.
32. Hosseini, S., *Chapter 5-Hydrogen storage and delivery challenges.* Fundamentals of Hydrogen Production and Utilization in Fuel Cell Systems, 2023: p. 237-254.
33. Sharifian, M., W. Kern, and G. Riess, *A Bird's-Eye View on Polymer-Based Hydrogen Carriers for Mobile Applications.* Polymers, 2022. **14**(21): p. 4512.
34. Tamura, A. and N. Yui, *Rational design of stimuli-cleavable polyrotaxanes for therapeutic applications.* Polymer journal, 2017. **49**(7): p. 527-534.
35. Sarker, M.N., et al., *Innovative Materials and Techniques for Enhancing Hydrogen Storage: A Comprehensive Review of Damage Detection and Preventive Strategies.* ASME Open Journal of Engineering, 2024. **3**.
36. Meille, V. and I. Pitault, *Liquid organic hydrogen carriers or organic liquid hydrides: 40 years of history.* Reactions, 2021. **2**(2): p. 94-101.
37. Lucentini, I., et al., *Review of the decomposition of ammonia to generate hydrogen.* Industrial & Engineering Chemistry Research, 2021. **60**(51): p. 18560-18611.
38. Shin, B.S., et al., *Thermodynamic assessment of carbazole-based organic polycyclic compounds for hydrogen storage applications via a computational approach.* International Journal of Hydrogen Energy, 2018. **43**(27): p. 12158-12167.
39. Müller, K., J. Völkl, and W. Arlt, *Thermodynamic evaluation of potential organic hydrogen carriers.* Energy Technology, 2013. **1**(1): p. 20-24.
40. Chu, C., et al., *Hydrogen storage by liquid organic hydrogen carriers: catalyst, renewable carrier, and technology–a review.* Carbon Resources Conversion, 2023. **6**(4): p. 334-351.
41. Dürr, S., et al., *Experimental determination of the hydrogenation/dehydrogenation-Equilibrium of the LOHC system H0/H18-*

dibenzyltoluene. International Journal of Hydrogen Energy, 2021. **46**(64): p. 32583-32594.

42. Tang, J., et al., *Recent progress and perspectives of liquid organic hydrogen carrier electrochemistry for energy applications.* Journal of Materials Chemistry A, 2024.
43. Zhang, J., et al., *Heterogeneous Catalysts in N-Heterocycles and Aromatics as Liquid Organic Hydrogen Carriers (LOHCs): History, Present Status and Future.* Materials, 2023. **16**(10): p. 3735.
44. Ni, Y., et al., *Catalytic hydrogen storage in liquid hydrogen carriers.* EES Catalysis, 2023. **1**(4): p. 459-494.
45. He, T., Q. Pei, and P. Chen, *Liquid organic hydrogen carriers.* Journal of energy chemistry, 2015. **24**(5): p. 587-594.
46. Cabrera, G., et al., *Liquid Organic Hydrogen Carrier Concepts and Catalysts for Hydrogenation and Dehydrogenation Reactions.* Molecules, 2024. **29**(20): p. 4938.
47. Abdin, Z., et al., *Large-scale stationary hydrogen storage via liquid organic hydrogen carriers.* Iscience, 2021. **24**(9).
48. Sultan, O. and H. Shaw, *Study of automotive storage of hydrogen using recyclable liquid chemical carriers.* NASA STI/recon technical report N, 1975. **76**: p. 33642.
49. Tan, K.C., et al., *Recent advances of catalysis in the hydrogenation and dehydrogenation of N-heterocycles for hydrogen storage.* The Journal of Physical Chemistry C, 2021. **125**(34): p. 18553-18566.
50. Shukla, A.A., et al., *Efficient hydrogen supply through catalytic dehydrogenation of methylcyclohexane over Pt/metal oxide catalysts.* International Journal of Hydrogen Energy, 2010. **35**(9): p. 4020-4026.
51. Pez, G.P., et al., *Hydrogen storage by reversible hydrogenation of pi-conjugated substrates*. 2008, Air Products and Chemicals, Inc., Allentown, PA (United States).
52. He, T., H. Cao, and P. Chen, *The roles of alkali/alkaline earth metals in the materials design and development for hydrogen storage.* Accounts of Materials Research, 2021. **2**(9): p. 726-738.
53. Coropceanu, V., et al., *Charge transport in organic semiconductors.* Chemical reviews, 2007. **107**(4): p. 926-952.
54. Kalyani, N.T. and S. Dhoble, *Organic light emitting diodes: Energy saving lighting technology—A review.* Renewable and Sustainable Energy Reviews, 2012. **16**(5): p. 2696-2723.

55. Wang, C., et al., *Semiconducting π-conjugated systems in field-effect transistors: a material odyssey of organic electronics.* Chemical reviews, 2012. **112**(4): p. 2208-2267.
56. Parida, B., S. Iniyan, and R. Goic, *A review of solar photovoltaic technologies.* Renewable and sustainable energy reviews, 2011. **15**(3): p. 1625-1636.
57. Costa, J.C., et al., *The impact of phenyl–phenyl linkage on the thermodynamic, optical and morphological behavior of carbazol derivatives.* RSC advances, 2020. **10**(20): p. 11766-11776.
58. Cui, L.-S., et al., *Bipolar host materials for high efficiency phosphorescent organic light emitting diodes: tuning the HOMO/LUMO levels without reducing the triplet energy in a linear system.* Journal of Materials Chemistry C, 2013. **1**(48): p. 8177-8185.
59. Zang, X.-F., et al., *Synthesis and photovoltaic performance of dihydrodibenzoazepine-based sensitizers with additional lateral anchor.* Dyes and Pigments, 2013. **99**(3): p. 1072-1081.
60. Ledwon, P., *Recent advances of donor-acceptor type carbazole-based molecules for light emitting applications.* Organic Electronics, 2019. **75**: p. 105422.
61. Waghmare, P.S., et al., *A Review on Carbazole and Its Derivatives as Anticancer Agents From 2013 to 2024.* Chirality, 2025. **37**(2): p. e70021.
62. Patil, S.A., et al., *Carbazole derivatives as potential antimicrobial agents.* Molecules, 2022. **27**(19): p. 6575.
63. Alothman, S., F. Kandil, and A. Deep, *Carbazole derivatives as antioxidant and anticorrosion materials.* Results in Chemistry, 2024. **9**: p. 101667.
64. Erdoğan, M. and A. Daştan, *Synthesis of N-substituted dibenzoazepine–pyridazine derivatives as potential neurologically active drugs.* Synthetic Communications, 2020. **50**(24): p. 3845-3853.
65. Wang, J., et al., *Bromine-Substituted Fluorene: Molecular Structure, Br–Br Interactions, Room-Temperature Phosphorescence, and Tricolor Triboluminescence.* Angewandte Chemie, 2018. **130**(51): p. 17063-17068.
66. Zhao, Z., S. Yan, and Z. Ren, *Regulating the nature of triplet excited states of thermally activated delayed fluorescence emitters.* Accounts of Chemical Research, 2023. **56**(14): p. 1942-1952.
67. Chen, Y., R.B. Sheu, and T.Y. Wu, *Novel light-emitting polymers containing donor and acceptor architectures.* Journal of Polymer Science Part A: Polymer Chemistry, 2003. **41**(6): p. 725-731.
68. Danel, K., et al., *Blue-emitting anthracenes with end-capping diarylamines.* Chemistry of materials, 2002. **14**(9): p. 3860-3865.

69. Arnau, A., *Piezoelectric transducers and applications*. Vol. 2004. 2004: Springer.
70. Lu, C. and A. Czanderna, *Methods and Phenomena, Their Applications in Science and Technology.* 1984.
71. Steinem, C. and A. Janshoff, *Piezoelectric sensors*. Vol. 5. 2007: Springer Science & Business Media.
72. Sauerbrey, G., *The use of quartz oscillators for weighing thin layers and for microweighing.* Z. Fur. Phys., 1959. **155**: p. 206-222.
73. Mecea, V., *Fundamentals of mass measurements.* Journal of thermal analysis and calorimetry, 2006. **86**(1): p. 9-16.
74. Brunetti, B., et al., *Vaporization of the prototypical ionic liquid BMImNTf 2 under equilibrium conditions: a multitechnique study.* Physical Chemistry Chemical Physics, 2014. **16**(29): p. 15653-15661.
75. da Silva, M.A.R., M.J. Monte, and L.M. Santos, *The design, construction, and testing of a new Knudsen effusion apparatus.* The Journal of Chemical Thermodynamics, 2006. **38**(6): p. 778-787.
76. Jacobson, N., D. Kobertz, and D. Sergeev, *Introduction to proceedings of the workshop on Knudsen effusion mass spectrometry.* Calphad, 2019. **65**: p. 111-126.
77. Copland, E.H. and N.S. Jacobson, *Measuring thermodynamic properties of metals and alloys with Knudsen effusion mass spectrometry.* 2010.
78. Verevkin, S.P., et al., *A new method for the determination of vaporization enthalpies of ionic liquids at low temperatures.* The Journal of Physical Chemistry B, 2011. **115**(44): p. 12889-12895.
79. Mohr, P.J., B.N. Taylor, and D.B. Newell, *CODATA recommended values of the fundamental physical constants: 2010.* Reviews of Modern Physics, 2012. **84**(4): p. 1527-1605.
80. Curtiss, L.A., et al., *Gaussian-1 theory of molecular energies for second-row compounds.* The Journal of Chemical Physics, 1990. **93**(4): p. 2537-2545.
81. Curtiss, L.A., et al., *Gaussian-2 (G2) theory: Reduced basis set requirements.* The Journal of chemical physics, 1996. **104**(13): p. 5148-5152.
82. Curtiss, L.A., et al., *Gaussian-3 (G3) theory for molecules containing first and second-row atoms.* The Journal of chemical physics, 1998. **109**(18): p. 7764-7776.
83. Curtiss, L.A., P.C. Redfern, and K. Raghavachari, *Gaussian-4 theory.* The Journal of chemical physics, 2007. **126**(8).

84. Baboul, A.G., et al., *Gaussian-3 theory using density functional geometries and zero-point energies.* The Journal of chemical physics, 1999. **110**(16): p. 7650-7657.
85. Harb, H., et al., *Accurate Dehydrogenation Enthalpies Dataset for Liquid Organic Hydrogen Carriers.* Scientific Data, 2025. **12**(1): p. 171.
86. Khairbek, A. and M.A.A.-H. Badawi, *Calculations of hydrogenation enthalpies of hydrocarbons by M06-2X/CBS extrapolated level in the gas phase.* Journal of Chemical Research, 2020. **44**(11-12): p. 762-768.
87. Prohaska, T., et al., *Standard atomic weights of the elements 2021 (IUPAC Technical Report).* Pure and Applied Chemistry, 2022. **94**(5): p. 573-600.
88. Sadashiva, M., et al., *Synthesis and crystal structure of 5-allyl-5 H dibenzo [b, f] azepine.* Journal of Chemical Crystallography, 2005. **35**(3): p. 171-175.
89. CSID:9886, h.w.c.c.C.-S.h., (accessed 16:55, Sept 30, 2025).
90. Nagaraj, B., H.S. Yathirajan, and D.E. Lynch, *1-(10, 11-Dihydrodibenz [b, f] azepin-5-yl) ethanone.* Structure Reports, 2005. **61**(6): p. o1609-o1610.

Appendix

Table A1 Areas and transmission probability factors of each effusion orifice made in platinum foil of the Knudsen effusion apparatus at FCUP.[1]

Series	Orifice number	Orifice diameter / mm	*l*/*r*	A_o / mm^2	w_o
Small	S1	0.7998	0.0313	0.502	0.9846
	S2	0.8050	0.0311	0.509	0.9847
	S3	0.7719	0.0324	0.503	0.9841
Medium	M4	0.9924	0.0252	0.774	0.9876
	M5	0.9986	0.0250	0.783	0.9876
	M6	1.0040	0.0249	0.792	0.9877
Large	L7	1.1830	0.0211	1.099	0.9895
	L8	1.1970	0.0209	1.125	0.9897
	L9	1.2000	0.0208	1.131	0.9897

[1]The symbols presented in this table have the following meaning: *l*, thickness of platinum foil (0.0125 mm); *r*, effusion orifice radius; A_o, effusion orifice areas; w_o, Clausing factors.

Table A2 Areas and transmission probability factors of each effusion orifice made in platinum foil of the Knudsen effusion apparatus at FCUP.[1]

Series	Orifice number	Orifice diameter / mm	*l*/*r*	A_o / mm^2	w_o
Small	S1, S2, S3	0.9000	0.0278	0.636	0.9863
Medium	M4, M5, M6	1.0000	0.0250	0.785	0.9877
Large	L7, L8, L9	1.1200	0.0223	0.985	0.9890

[1]The symbols presented in this table have the following meaning: *l*, thickness of platinum foil (0.0125 mm); *r*, effusion orifice radius; A_o, effusion orifice areas; w_o, Clausing factors.